On the Richtmyer-Meshkov Instability in Magnetohydrodynamics

Thesis by
Vincent Wheatley

In Partial Fulfillment of the Requirements
for the Degree of
Doctor of Philosophy

California Institute of Technology
Pasadena, California

2005

(Defended May 17, 2005)

Acknowledgements

First, I thank my adviser, Dale Pullin, for his insightful suggestions, advice, and encouragement over the years. Next, I would like to thank Ravi Samtaney of the Princeton Plasma Physics Laboratory. As well as writing the paper that inspired my work, he provided the codes that I used during my time at Caltech along with a great deal of valuable advice. My friends and colleagues at the Iris lab, Gerard O'Reilly, Philippe Chatelain, James Faddy, Nikoo Saber, Paul O'Gorman and Mike Rubel made the lab a great place to come to work every day. Mike and Philippe also worked hard to keep the machines running and provided all the software advice I needed, for which I am grateful. I also thank my colleagues in the ASC CTC group for all their hard work that kept the project on track, as well as the help and advice they gave me throughout my PhD.

I am most grateful to my wife Cindy, who gave me her unconditional and invaluable support throughout my years at Caltech. Many thanks also go to my parents who have never stopped encouraging me.

This effort was supported by the Academic Strategic Alliances Program of the Accelerated Strategic Computing Initiative (ASCI/ASAP) under subcontract no. B341492 of DOE contract W-7405-ENG-48.

Abstract

The Richtmyer-Meshkov instability is important in a wide variety of applications including inertial confinement fusion and astrophysical phenomena. In some of these applications, the fluids involved may be plasmas and hence be affected by magnetic fields. For one configuration, it has been numerically demonstrated that the growth of the instability in magnetohydrodynamics is suppressed in the presence of a magnetic field. Here, the nature of this suppression is theoretically and numerically investigated.

In the framework of ideal incompressible magnetohydrodynamics, we examine the stability of an impulsively accelerated, sinusoidally perturbed density interface in the presence of a magnetic field that is parallel to the acceleration. This is accomplished by analytically solving the linearized initial value problem, which is a model for the Richtmyer-Meshkov instability. We find that the initial growth rate of the interface is unaffected by the presence of a magnetic field, but for a finite magnetic field the interface amplitude asymptotes to a constant value. Thus the instability of the interface is suppressed. The interface behavior from the analytical solution is compared to the results of both linearized and non-linear compressible numerical simulations for a wide variety of conditions.

We then consider the problem of the regular refraction of a shock at an oblique, planar contact discontinuity separating conducting fluids of different densities in the presence of a magnetic field aligned with the incident shock velocity. Planar ideal MHD simulations indicate that the presence of a magnetic field inhibits the deposition of vorticity on the shocked contact, which leads to the suppression of the Richtmyer-Meshkov instability. We show that the shock refraction process produces a system of five to seven plane waves that may include fast, intermediate, and slow MHD shocks, slow compound waves, 180^o rotational discontinuities, and slow-mode expansion fans that intersect at a point. In all solutions, the shocked contact is vorticity free and hence stable. These solutions are not unique, but differ in the type of waves that participate. The set of equations governing the structure of these

multiple-wave solutions is obtained in which fluid property variation is allowed only in the azimuthal direction about the wave-intersection point. Corresponding solutions are referred to as either quintuple-points, sextuple-points, or septuple-points, depending on the number of participating waves. A numerical method of solution is described and examples are compared to the results of numerical simulations for moderate magnetic field strengths. The limit of vanishing magnetic field at fixed permeability and pressure is studied for two solution types. The relevant solutions correspond to the hydrodynamic triple-point with the shocked contact replaced by a singular structure consisting of a wedge, whose angle scales with the applied field magnitude, bounded by either two slow compound waves or two 180^o rotational discontinuities, each followed by a slow-mode expansion fan. These bracket the MHD contact which itself cannot support a tangential velocity jump in the presence of a non-parallel magnetic field. The magnetic field within the singular wedge is finite and the shock-induced change in tangential velocity across the wedge is supported by the expansion fans that form part of the compound waves or follow the rotational discontinuities. To verify these findings, an approximate leading order asymptotic solution appropriate for both flow structures was computed. The full and asymptotic solutions are compared quantitatively and there is shown to be excellent agreement between the two.

Contents

List of Figures

List of Tables

Chapter 1

Introduction

Consider the interaction of a shock wave with a perturbed interface separating two fluids of different properties. Such an interaction is illustrated in Fig. 1.1. In most cases the perturbations will grow following the interaction. This scenario was first considered by Markstein (1957). A rigorous theoretical and numerical analysis of the problem was later presented by Richtmyer (1960). Richtmyer's predictions were then confirmed by the shock tube experiments of Meshkov (1969). This class of problems is therefore known as the Richtmyer-Meshkov instability (RMI). The mechanism that drives the instability is the baroclinic generation of vorticity that occurs due to the misalignment of the pressure gradient across the incident shock and the density gradient across the interface, as shown in Fig. 1.1(a). For non-conducting fluids, and conducting fluids in the absence of an applied magnetic field, this vorticity is deposited on the interface during the shock refraction process. Subsequently, the vorticity distribution on the interface causes the perturbations to grow. As the interface becomes more distorted, secondary instabilities arise and a region of turbulent mixing eventually develops (Brouillette, 2002).

The RMI is important in a wide variety of applications. One of the most significant of these is inertial confinement fusion, which has been a major impetus for the study of shock accelerated interfaces (Brouillette, 2002). In direct-drive inertial confinement fusion, a capsule filled with fuel, typically deuterium and tritium, is placed at the focus of a spherical array of lasers. The lasers heat the surface of the capsule, which

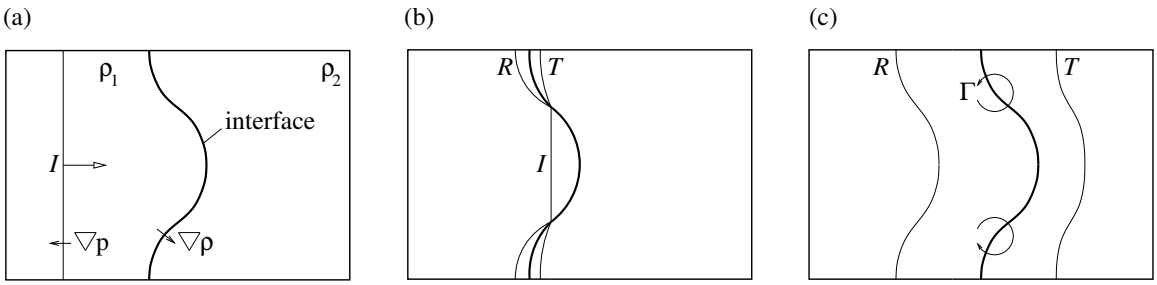

Figure 1.1: Illustration of a shock interaction that produces the Richtmyer-Meshkov instability for a case where transmitted and reflected shocks are generated. (a) Pre-interaction configuration. (b) Configuration during the interaction. (c) A post-interaction configuration. I, T, and R designate the incident, transmitted, and reflected shocks, respectively. ρ is density and p is pressure. The curved arrows indicate the local direction of the circulation, Γ.

drives a spherical shock into the target, with the goal being to compress the fuel to such an extent that the temperature and density at the center are sufficient to initiate a fusion reaction. The RMI promotes mixing between the capsule material and the fuel. This mixing limits the final compression of the fuel and hence the possibility of achieving energy break-even or production (Lindl et al., 1992). The RMI is also important in astrophysical phenomena. It has been used to account for the lack of stratification in the products of supernova 1987A and is required in stellar evolution models (Arnett, 2000). In supersonic and hypersonic air breathing engines, the RMI may be used to enhance the mixing of fuel and air (Yang et al., 1993). The RMI also arises in many combustion systems where shock-flame interactions occur, the resulting instability is significant in deflagration-to-detonation transition (Khokhlov et al., 1999). Finally, in reflected shock tunnels, the RMI is a possible mechanism for explaining driver gas contamination in the absence of shock bifurcation due to the wall boundary layer (Stalker and Crane, 1978, Brouillette and Bonazza, 1999).

In the first two applications of the RMI listed above, inertial confinement fusion and astrophysical phenomena, the fluids involved may be plasmas and hence be affected by magnetic fields. It is well known that the linear growth rate of the Rayleigh-Taylor instability, a hydrodynamic instability related to the RMI, is mitigated at high wavenumbers in the presence of a magnetic field (Chandrasekhar, 1961).

The effect of a magnetic field on the RMI, however, has not been thoroughly investigated (Samtaney, 2003). For one configuration, Samtaney (2003) has demonstrated, via numerical simulations, that the growth of the RMI is suppressed in the presence of a magnetic field. The goal of this thesis is to theoretically and numerically investigate the cause and extent of this suppression. In the remainder of this chapter, various results for the hydrodynamic RMI are reviewed, along with relevant results from magnetohydrodynamics (MHD). Literature specific to each of the subtopics addressed herein, but not the investigation as a whole, is reviewed in the relevant chapters. Finally, the problems that are addressed in this investigation are outlined and justified.

1.1 The Richtmyer-Meshkov instability in hydrodynamics

Richtmyer (1960) proposed that after the transmitted and reflected waves have traveled sufficiently far from the interface, the motion of the fluid around the interface can be considered incompressible. Motivated by this, Richtmyer applied the linear theory of Taylor (1950), for the growth of single mode perturbations on a discontinuous interface between incompressible fluids, to the case where the interface is impulsively accelerated. From this he obtained what is known as the impulse model for the growth rate of the interface, $\dot{\eta}$:

$$\dot{\eta} = k\Delta V \eta_0 \mathcal{A}. \tag{1.1}$$

Here, k is the wavenumber of the perturbation, ΔV is velocity imparted to the interface by the interaction with the incident shock, η_0 is the initial amplitude of the perturbations, and $\mathcal{A} \equiv (\rho_2 - \rho_1)/(\rho_2 + \rho_1)$ is the Atwood number formed from the post-shock densities to the left and right of the interface, ρ_1 and ρ_2, respectively. The post-shock value of a quantity is that which it takes immediately following the interaction of the incident shock with the interface. Eq. 1.1 is a model for the asymptotic

growth rate after the passage of the incident shock, but is only valid while $k\eta_0 \ll 1$.

Richtmyer (1960) numerically solved the compressible linearized RMI problem for the case where the incident shock is strong, the gases are ideal, and both the transmitted and reflected waves are shocks. The compressible linear theory has since been clarified and extended by a number of authors (Fraley, 1986, Mikaelian, 1994a,b, Yang et al., 1994, Wouchuk and Nishihara, 1997, Velikovich, 1996). The consensus of investigators is that in the impulse model, η_0 should be set to the post-shock amplitude of the interface if the reflected wave is a shock, and the average of the pre- and post-shock amplitudes for a reflected rarefaction (Zabusky, 1999). The latter prescription is due to Meyer and Blewett (1972). With the parameters chosen in this fashion, Yang et al. (1994) conclude that the impulse model agrees well with their compressible linear theory in the weak shock limit. As the shock strength is increased, the discrepancy between them can become quite large. Compressible linear models of the RMI exhibit the following important features (Brouillette, 2002): As the growth rate increases from zero towards the asymptotic value following the shock interaction, there is a kink in the growth rate. This is caused by the first convergence of the pair of transverse waves behind the transmitted shock, which temporarily decreases the growth rate. These transverse waves form because of the curvature of the shocks generated by the interaction of the incident shock with the interface. After sufficient time, the growth rate approaches its asymptotic value, which is well approximated by the impulse model for weak shocks. Subsequent oscillations of the growth rate are caused by the pressure field induced by the interaction of transverse waves downstream of the transmitted and (if present) reflected shocks.

Much can be learned about the RMI from the vortex paradigm, in which the instability is modeled by the evolution of a vortex sheet of varying strength that represents the shocked interface. The distribution of circulation deposited on the interface by the shock interaction can be estimated, for example, by using a local shock polar analysis at each point along the interface (Samtaney and Zabusky, 1994). An extensive discussion on the vortex paradigm can be found review of Zabusky (1999). A number of non-linear theories have also been developed for the late time

development of the RMI. These models were recently reviewed by Brouillette (2002), along with the issues relating to experimental investigations of the RMI, but are not discussed here as this thesis is concerned with the instability in the linear regime.

1.2 MHD results

As discussed earlier, Samtaney (2003) has utilized numerical simulations to demonstrate that the growth of the Richtmyer-Meshkov instability is suppressed in the presence of a magnetic field. The particular flow studied was that of a shock interacting with an oblique planar contact discontinuity (CD) separating conducting fluids of different densities within the framework of ideal MHD. The physical setup for this shock interaction problem is depicted in Figure 1.2. Two cases were simulated; one in which where was no magnetic field, and one in which an applied magnetic field was aligned with the motion of the incident shock. Figure 1.3 shows the density fields for these two cases after the incident shock has passed through the interface. For the case with no applied magnetic field, vorticity is deposited on the interface during the shock interaction. The interface is then a vortex layer and rolls up. For the case with an applied magnetic field, the interface remains smooth and no roll-up is observed, indicating that the instability is suppressed (Samtaney, 2003).

The suppression of the instability can be understood by examining how the shock refraction process at the interface changes with the application of a magnetic field. For the case with no applied magnetic field, the details of the shock refraction process are as follows: For Samtaney's choice of parameters, the incident shock bifurcates into a reflected shock and a transmitted shock. The shocked interface is a vortex sheet in the analytical solution, but in the simulation it becomes a vortex layer due to numerical diffusion. Thus, in the absence of an applied magnetic field, the shock refraction process deposits vorticity on the interface, causing it to be locally Kelvin-Helmholtz unstable. When a magnetic field is present, this solution is generally not valid because contact discontinuities cannot support a tangential velocity jump in MHD if the magnetic field is not parallel to the discontinuity (Sutton and Sherman,

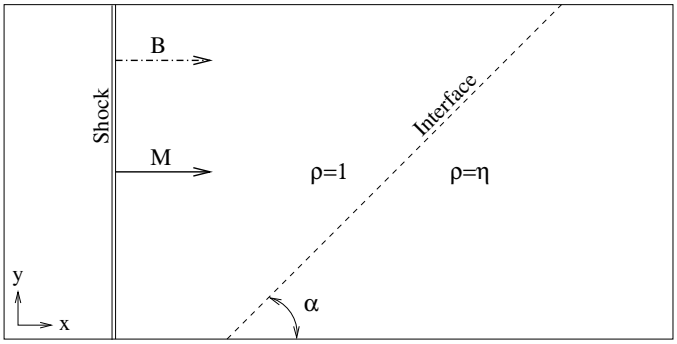

Figure 1.2: Physical setup for the Richtmyer-Meshkov simulations of Samtaney (2003). M is the incident shock *sonic* Mach number, η is the density ratio across the interface, α is the angle between the incident shock normal and the interface, and B is the applied magnetic field magnitude. The initial pressure in the unshocked regions is $p_0 = 1$. Symmetry boundary conditions are applied in the vertical direction.

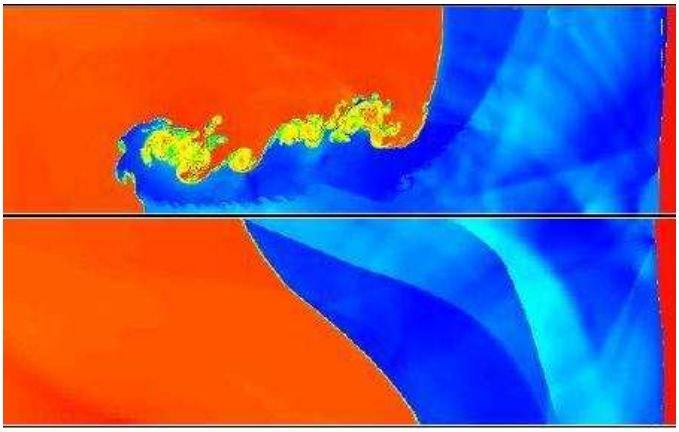

Figure 1.3: Density fields from the Richtmyer-Meshkov simulations of Samtaney (2003) after the incident shock has completely passed through the interface. The initial condition geometry is shown in Figure 1.2. The transmitted shock is located near the right-hand edge of each image. The top image is from a simulation with no magnetic field, while the bottom image is from a simulation where a magnetic field is present. Note that the vertical co-ordinate is reversed in the bottom image.

1965). In this case, Samtaney observes that a pair of transmitted shocks and a pair of reflected shocks result from the shock refraction process. These shocks support tangential velocity jumps and leave the shocked interface vorticity free, and hence locally Kelvin-Helmholtz stable.

At the time of Samtaney's paper, the MHD shock interaction problem had only been investigated for special cases where the incident shock velocity and the applied magnetic field are aligned in the reference frame of the intersection point between the shocks. In such cases, the MHD Rankine-Hugoniot relations ensure that the magnetic field is parallel to the shocked contact discontinuity, which allows jumps in tangential velocity and magnetic field across it. This permits three-shock solutions to what is referred to as the aligned field shock interaction problem (Ogawa and Fujiwara, 1996). Such solutions can be constructed using shock polar analysis and have been studied in detail by Bestman (1975) and Ogawa and Fujiwara (1996). Solutions to the aligned field shock interaction problem that involve expansion fans, compound waves, or rotational discontinuities were not investigated.

Wu and Roberts (1999) and Wu (2000, 2003) have simulated the instability of a shock accelerated tangential discontinuity in ideal MHD. The component of the magnetic field normal to a tangential discontinuity vanishes allowing it to support jumps in tangential magnetic field (B_t), tangential velocity, and pressure, provided that the total pressure is continuous. Cases were simulated both with and without a change in the sign of B_t across the tangential discontinuity. In the initial conditions, only the discontinuity in density was perturbed, the discontinuity in B_t and pressure remained planar. This implies that the initial interface is not a true tangential discontinuity, making rigorous interpretation of the results of the simulations difficult. They find that when B_t does not change sign across the discontinuity, the instability tends to be stabilized by the magnetic field, although the extent to which this occurs was not quantified. The mechanism behind the stabilization was stated to be field line tension. When B_t changes sign across the discontinuity, magnetic reconnection events were found to occur.

1.3 Thesis outline

Chapter 2: To demonstrate that the MHD RMI is suppressed in the presence of a magnetic field, Samtaney (2003) simulated a shock interacting with an oblique planar density interface. In hydrodynamics, a more widely studied flow results from a shock wave accelerating a density interface with a single-mode sinusoidal perturbation in amplitude. In Chapter 2, MHD simulations of this flow in the presence and absence of a magnetic field are presented. The numerical method used to carry out the simulations is described first, then the setup for the simulations is defined. Finally, the results of the simulations are presented and discussed. Of particular interest is the time evolution of the interface amplitude when a magnetic field is present, which shows that the growth of the interface is not completely suppressed. This behavior of the interface was not presented by Samtaney (2003) and could not be immediately explained.

Chapter 3: To understand the behavior of the interface seen in Chapter 2, and the effect of a magnetic field on the MHD RMI in general, a linearized model problem is studied in Chapter 3. The model problem consists of a sinusoidally perturbed interface separating incompressible conducting fluids of different densities that is impulsively accelerated at $t = 0$. There is a magnetic field aligned with the impulsive acceleration. The formulation, linearization, and analytical solution of the initial value problem are presented. The key features of the resulting incompressible linear model for the MHD RMI are then discussed.

Chapter 4: The model developed in Chapter 3 differs from the full MHD Richtmyer-Meshkov instability in that it is incompressible, linear, and is driven by an impulse rather than by the impact of a shock wave. In Chapter 4, the performance of the linear model is assessed for a variety of cases by comparing it with the results of compressible MHD simulations. In each case, impulse and shock driven linearized simulations and a non-linear simulation were carried out. This allows the effects on the flow of compressibility, shock acceleration, and non-linearity to be assessed systematically. The performance of the linear model is first analyzed for a baseline

case with small incident shock strength, initial perturbation amplitude, and applied magnetic field magnitude. We then examine how the performance of the linear model is affected as each of these are increased.

Chapter 5: Samtaney (2003) has identified the change in the MHD shock refraction process with the application of a magnetic field as the mechanism by which the MHD RMI is suppressed. In hydrodynamics, a solution to the shock refraction problem was required in order for the analysis of the compressible RMI to be carried out (Richtmyer, 1960). A solution technique for the MHD shock refraction problem therefore seems essential to the analysis of the MHD RMI. In Chapter 5, such a solution technique is developed. This technique is then used to demonstrate that the structure seen in Samtaney's simulations, and other similar structures, are entropy-satisfying weak solutions of the equations of ideal MHD. The effects of decreasing magnetic field magnitude on the shock refraction process are then investigated. We find that the types of waves arising from the shock refraction process undergo a number of transitions, resulting in a wide variety of flow structures. It is also demonstrated that entropy-satisfying weak solutions to the MHD shock refraction problem are generally not unique, thus other admissibility conditions are required to select a single physical solution.

Chapter 6: In the hydrodynamic triple-point solution to a shock refraction problem, which occurs in MHD in the absence of a magnetic field, the shocked contact discontinuity is a vortex sheet. If, however, a magnetic field is present, even if it is vanishingly small in magnitude, the contact discontinuity cannot support a tangential velocity jump. This appears to be a paradox. This problem is addressed in Chapter 6, where we examine how the solutions to the MHD shock refraction problem identified in Chapter 5 approach the hydrodynamic triple-point in the limit of vanishing applied magnetic field. Initially, this is done by applying the solution technique developed in Chapter 5 to cases in which the magnetic field is small. Next, the equations governing the leading order asymptotic solution of the shock refraction problem in the limit of vanishing applied magnetic field are derived. The chapter concludes with a

comparison between the asymptotic and full solutions.

Chapter 7: The major findings to arise from this thesis are summarized in Chapter 7.

Chapter 2

Initial Simulations

2.1 Introduction

Samtaney (2003) has demonstrated, via planar ideal MHD simulations, that the growth of the RMI is suppressed in the presence of a magnetic field. In his simulations, a shock interacted with an oblique planar contact discontinuity (CD) separating conducting fluids of different densities. The suppression of the instability is caused by changes in the shock refraction process at the CD with the application of a magnetic field, which will be discussed in detail in Chapter 5. A more widely studied flow results from a shock wave accelerating a density interface with a single-mode sinusoidal perturbation in amplitude. Our goal is to understand the effect of a magnetic field on this flow when conducting fluids are involved. As a first step towards this goal, this flow was simulated both in the presence and absence of a magnetic field. In this chapter, we first present the governing equations for the simulations. The setup for the simulations is then defined and the results of the simulations are presented. Finally, the significance of the results is discussed.

2.2 Governing equations

The governing equations for the simulations presented in this chapter are the ideal MHD equations. For completeness, we present the following brief account of the

assumptions that were made in deriving these equations. The complete details of their derivation may be found, for example, in Sutton and Sherman (1965). Consider the motion of a continuum fluid in the presence of an electromagnetic field, where the fluid contains species that are electrically charged so that currents may flow within it. For simplicity, the magnetization and polarization of individual particles are neglected. Due to the ability of the fluid to conduct electricity, the electromagnetic field has two primary effects: to create body forces that act on the fluid and to exchange energy with the fluid (Sutton and Sherman, 1965). Accounting for these two effects, the equations of mass, momentum, and energy conservation, respectively, in the absence of viscosity, thermal conductivity, and interspecies diffusion are (see e.g., Sutton and Sherman (1965)),

$$\begin{aligned}
\frac{\partial \rho}{\partial t} + \nabla \cdot (\rho \mathbf{u}) &= 0, \\
\rho \frac{D\mathbf{u}}{Dt} &= -\nabla p + \rho_e \mathbf{E} + \mathbf{J} \times \mathbf{B}, \\
\rho \frac{D}{Dt} \left(e + \frac{1}{2} \mathbf{u} \cdot \mathbf{u} \right) &= \mathbf{E} \cdot \mathbf{J} - \nabla \cdot (p\mathbf{u}).
\end{aligned}$$

Here, ρ is the density, p is the pressure, $\mathbf{u}$ is the velocity, $\mathbf{B}$ is the magnetic field, $\mathbf{E}$ is the electric field, e is the internal energy per unit mass, ρ_e is the free charge density, and $\mathbf{J}$ is the total current density, which is the sum of the conduction current and the transport of excess charge $\rho_e \mathbf{u}$. In the momentum equation, $\rho_e \mathbf{E}$ is the electrostatic body force and $\mathbf{J} \times \mathbf{B}$ is the Lorentz force. To complete the system, the equations governing the electromagnetic field are required. These are Maxwell's equations. Neglecting the magnetization of individual particles, Maxwell's equations

are (see e.g., Sutton and Sherman (1965)),

$$\nabla \cdot \mathbf{E} = \frac{\rho_e}{K_0},$$
$$\nabla \cdot \mathbf{B} = 0,$$
$$\nabla \times \mathbf{E} = -\frac{\partial \mathbf{B}}{\partial t},$$
$$\nabla \times \mathbf{B} = \mu_0 \left(\mathbf{J} + K_0 \frac{\partial \mathbf{E}}{\partial t} \right),$$

where K_0 is the permittivity and μ_0 is the magnetic permeability of vacuum.

In typical applications of magnetohydrodynamics, three approximations have been shown to be accurate (Sutton and Sherman, 1965): $K_0 \frac{\partial \mathbf{E}}{\partial t}$ can be neglected in Maxwell's equations, in the total current density $\rho_e \mathbf{u}$ is small compared to the conduction current, and $\rho_e \mathbf{E}$ may be neglected in the momentum equation. These are known as the magnetohydrodynamic approximations. The conduction current density is denoted $\mathbf{j}$ and is given by Ohm's law. With ion slip neglected, Ohm's law is,

$$\mathbf{j} = \sigma \left(\mathbf{E} + \mathbf{u} \times \mathbf{B} - \beta \mathbf{j} \times \mathbf{B} \right),$$

where σ is the electrical conductivity. Here, we consider the ideal MHD equations in which viscosity, thermal conductivity, and electrical resistivity σ^{-1} are taken to be zero. To further simplify the equations, the Hall current $\sigma\beta \mathbf{j} \times \mathbf{B}$ and ion slip are neglected in Ohm's law (Sutton and Sherman, 1965). After applying these assumptions and the magnetohydrodynamic approximations,

$$\mathbf{E} = -\mathbf{u} \times \mathbf{B},$$
$$\mathbf{j} = \frac{1}{\mu_0} \nabla \times \mathbf{B}.$$

Using these relations to eliminate $\mathbf{E}$ and $\mathbf{j}$, and again applying the magnetohydrody-

namic approximations, the following set of simplified equations are obtained:

$$\frac{\partial \rho}{\partial t} + \nabla \cdot (\rho \mathbf{u}) = 0, \tag{2.1}$$

$$\rho \frac{D\mathbf{u}}{Dt} = -\nabla p + \frac{1}{\mu_0} (\nabla \times \mathbf{B}) \times \mathbf{B}, \tag{2.2}$$

$$\rho \frac{D}{Dt} \left(e + \frac{1}{2} \mathbf{u} \cdot \mathbf{u} \right) = -\frac{1}{\mu_0} (\nabla \times \mathbf{B}) \cdot (\mathbf{u} \times \mathbf{B}) - \nabla \cdot (p\mathbf{u}). \tag{2.3}$$

$$\nabla \cdot \mathbf{B} = 0, \tag{2.4}$$

$$\frac{\partial \mathbf{B}}{\partial t} = \nabla \times (\mathbf{u} \times \mathbf{B}) \tag{2.5}$$

The final equation is known as the induction equation. It is convenient to normalize $\mathbf{B}$ by $\sqrt{\mu_0}$, thus eliminating μ_0 from the system of equations.

Eqs. 2.1-2.5 can be written in conservation form as follows:

$$\frac{\partial U}{\partial t} + \frac{\partial F_j(U)}{\partial x_j} = 0, \tag{2.6}$$

where the vector of conserved variables $U \equiv U(x_i, t)$ is,

$$U = \{\rho, \rho u_i, B_i, \rho e_T\}^T,$$

and the flux vectors $F_j(U)$ are,

$$F_j(U) = \Big\{ \rho u_j \, , \, \rho u_i u_j + (p + \frac{1}{2} B_k B_k)\delta_{ij} - B_i B_j \, , \\ u_j B_i - u_i B_j \, , \, (\rho e_T + p + \frac{1}{2} B_k B_k) u_j - B_j (B_k u_k) \Big\}^T .$$

Here, ρe_T is the total energy per unit volume of the plasma. The plasma is assumed to be ideal with constant specific heats, allowing the following equation of state to be used to close the set of equations:

$$\rho e_T = \frac{p}{\gamma - 1} + \frac{1}{2} \rho u_k u_k + \frac{1}{2} B_k B_k.$$

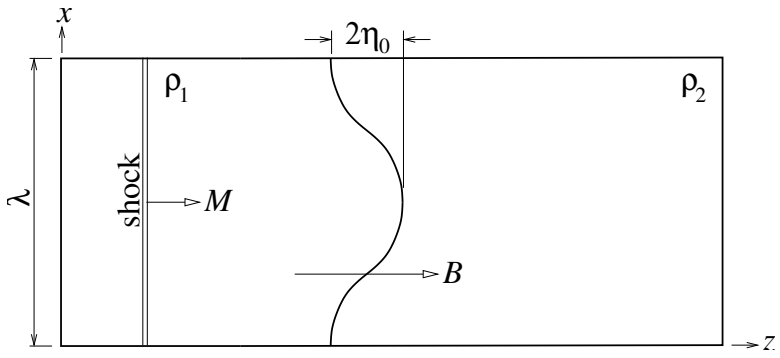

Figure 2.1: Initial condition geometry for initial MHD RMI simulation.

2.3 Initial simulation setup

The simulations presented in this chapter were carried out using a method developed by Ravi Samtaney (Computational Plasma Physics Group, Princeton Plasma Physics Laboratory, Princeton University, NJ) for obtaining numerical solutions to the ideal MHD equations. The numerical method is a non-linear compressible MHD solver that uses the 8-wave upwinding formulation of Powell et al. (1999a) within an unsplit upwinding method (Colella, 1990a). The solenoidal property of the magnetic field is enforced at each time step using a projection method. A constrained transport step is then used remove divergence modes with a centered finite difference representation. This uses the formulation prescribed by Toth (2000). The details of the numerical method are presented in Appendix A.

The initial condition geometry for the simulations is illustrated in Fig. 2.1. As in the simulations of Samtaney (2003), the magnetic field is initially aligned with the motion of the shock. This implies that the hydrodynamics are decoupled from the magnetic field until the incident shock begins to interact with the interface. The flow is characterized by the incident shock sonic Mach number, M, the density ratio across the interface, ρ_2/ρ_1, the ratio of the interfaces initial amplitude to its wavelength, η_0/λ, the ratio of specific heats, γ, and the non-dimensional strength of the applied magnetic field, $\beta^{-1} = B^2/(2p_0)$. Here B is the magnitude of the applied magnetic field and p_0 is the initial pressure in the unshocked regions of the flow.

For both simulations presented in this chapter, $M = 2$, $\rho_2/\rho_1 = 3$, $\eta_0/\lambda = 0.1$,

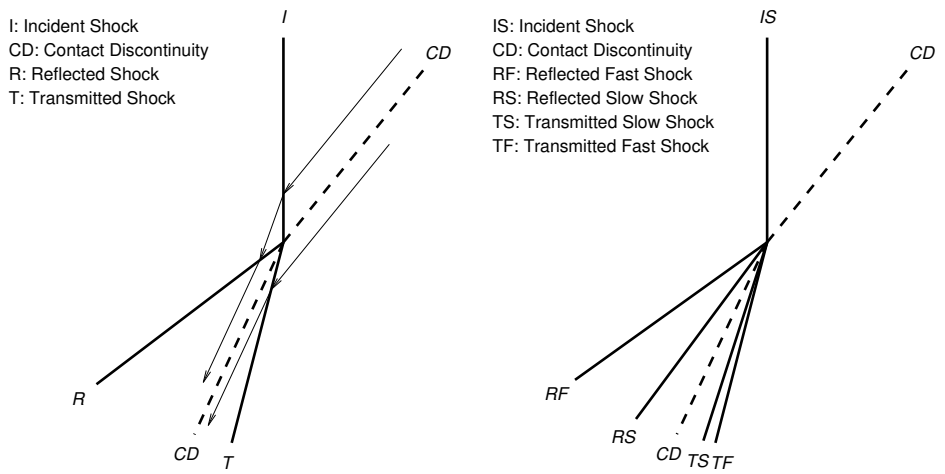

(a) (b)

Figure 2.2: (a) Triple-point wave structure and streamlines resulting from a shock refraction process with $M = 2$, $\alpha = 1$, $\rho_2/\rho_1 = 3$ and $\gamma = 5/3$ in the absence of an applied magnetic field ($\beta^{-1} = 0$). (b) Wave structure resulting from a MHD shock refraction process with $M = 2$, $\alpha = 1$, $\rho_2/\rho_1 = 3$, $\gamma = 5/3$, and $\beta = 1$. Here α is the angle between the incident shock normal and the unshocked interface. These structures were computed using the technique detailed in Chapter 5.

and $\gamma = 5/3$. In the simulation in which a magnetic field is present, $\beta^{-1} = 1$. This set of parameters was chosen because it can be shown, using the method detailed in Chapter 5, that the shock refraction process at the interface does not produce any intermediate MHD shocks (the various types of MHD discontinuities are defined in Section 5.2.2). Examples of the computed structures produced by the shock refraction process for one particular angle of incidence are shown in Fig. 2.2. In the case without a magnetic field, transmitted and reflected hydrodynamic shocks are generated. These are labeled T and R, respectively. In the case with a magnetic field, four MHD shocks are generated; a transmitted fast shock TF, a transmitted slow shock TS, a reflected fast shock RF, and a reflected slow shock RS. It is desirable to avoid the generation of intermediate shocks at the interface because the physical relevance of such shocks is not yet completely clarified, as discussed in Section 5.2.3. In the simulation that Samtaney (2003) presented in detail, one intermediate shock was generated by the shock refraction process.

To reduce the cost of the computations, only a half period of the interface is simulated, thus the length of each computational domain in the x-direction is $L_x = \lambda/2$. This is possible because symmetry boundary conditions are enforced on the boundaries $x = 0$ and $x = L_x$. The simulations were run for a period $T_{sim}/t^* = 5$, where $t^* = \lambda/\sqrt{p_0/\rho_1}$. The length of each computational domain in the z-direction is $L_z = 12\lambda$. At $z = 0$ and $z = L_z$, zero gradient boundary conditions are applied. Spurious reflections would occur if shocks crossed these boundaries, thus the simulations are terminated before any shocks exit the domain. Each physical domain is discretized into a mesh of $N_x \times N_z$ mesh points. Here $N_x = 128$ and $N_z = 3072$ so that the cells are square.

The interface is initially centered at $z_{if} = 3.36\lambda$. This is so that the fastest transmitted and reflected shocks generated by the shock refraction process at the interface reach the ends of the domain at approximately the same time, maximizing the duration of the simulation. Where the interface initially crosses a cell, the density in that cell is set to the appropriate area weighted average of ρ_1 and ρ_2. In the initial condition, the incident shock is represented by the appropriate discontinuous change in fluid properties at $z_{shock} = z_{if} - \lambda/5$.

2.4 Initial simulation results

Time sequences of density and vorticity fields from the simulations without (i) and with (ii) an initial magnetic field are shown in Fig. 2.3. In the simulation without a magnetic field, the transmitted and reflected shocks are clearly visible in the density fields. Although these shocks are curved, and are therefore sources of vorticity, the vorticity they produce is too small in magnitude to be visible in all the vorticity fields. Note the presence of the transverse waves that are generated downstream of the leading transmitted and reflected shocks in each simulation. It can be seen from Fig. 2.3(i) that the vorticity generated by the shock refraction process remains at the interface. This causes the interface to roll up into the mushroom shape characteristic of the hydrodynamic RMI. In ideal MHD, the evolution equation for the magnetic

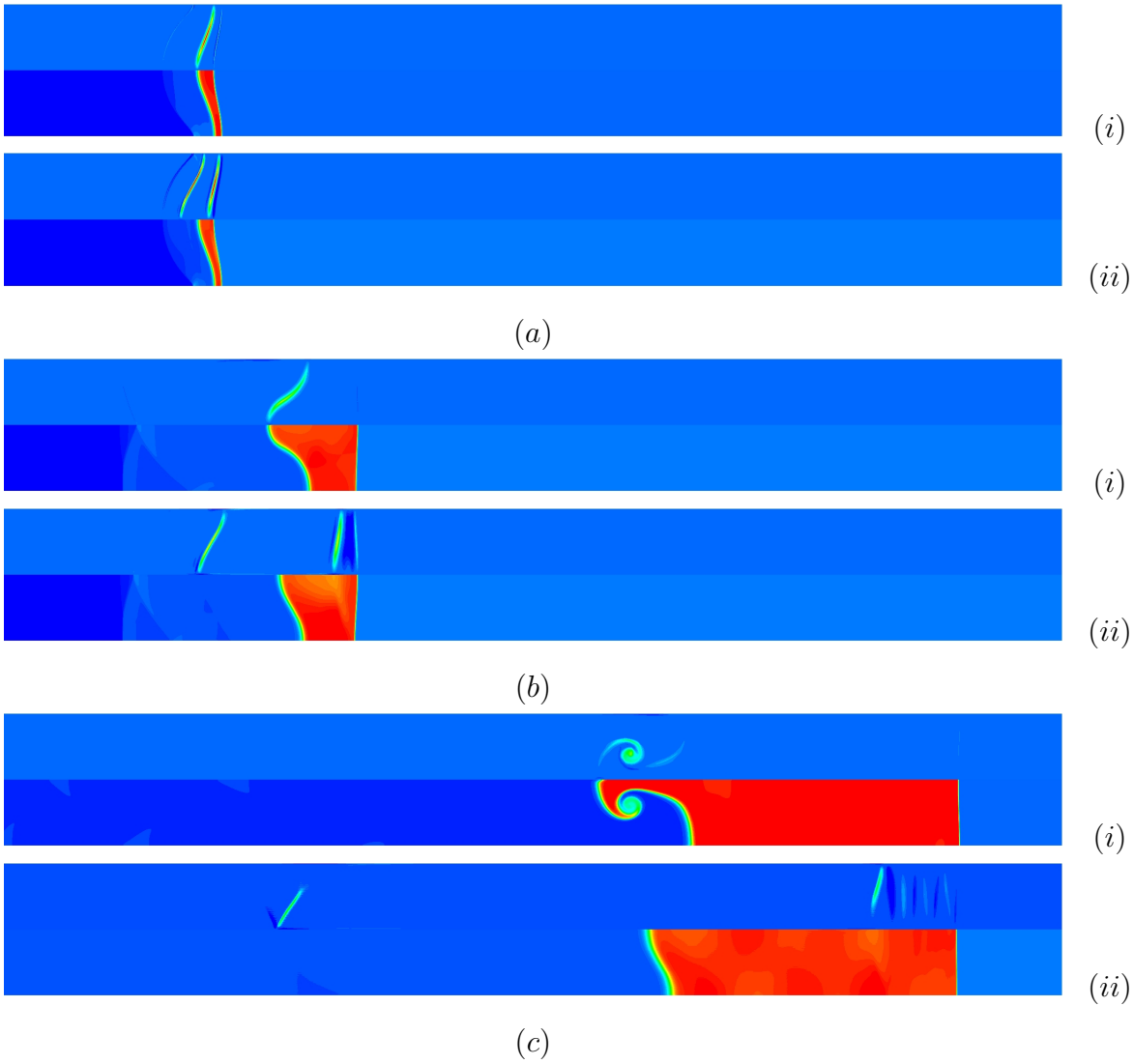

Figure 2.3: Vorticity and density fields from compressible simulations with $M = 2$, $\rho_2/\rho_1 = 3$, $\eta_0/\lambda = 0.1$, $\gamma = 5/3$, and (i) $B = 0$ or (ii) $\beta = 1$ at (a) $t/t^* = 0.2$, (b) $t/t^* = 0.8$, and (c) $t/t^* = 3.4$. The top half of each plot shows vorticity while the bottom half shows density. At the time of these images, the incident shock has interacted with the interface. In (c), the resulting transmitted fast shock is located near the right-hand end of each image while the reflected fast shock is located beyond the left-hand edge of each image. Note that the full computational domain is not shown; in the plots, $2 < z/\lambda < 10$.

field ensures that if it is zero initially, it remains zero throughout the simulation. Thus, in the absence of a magnetic field at $t = 0$, the fact that conducting fluids are involved does not alter the RMI from the hydrodynamic case. In the simulation with a magnetic field, the transmitted and reflected fast shocks that are are clearly visible in the density fields. The tangential velocity jumps across these shocks are considerably smaller than those across the slow shocks, thus they are not as visible in the vorticity fields. The transmitted and reflected slow shocks have small density jumps across them and therefore do not feature prominently in the density fields. It can be seen from the vorticity fields, however, that the majority of the vorticity generated during the shock refraction process is transported away from the interface via the tangential velocity jumps across the slow shocks. In the ideal case, this leaves the interface with zero circulation-per-unit-length, which drastically alters its evolution. This is evident from a comparison of Fig. 2.3(c)(i) and Fig. 2.3(c)(ii), where the interface from the simulation with a magnetic field present exhibits none of the roll up seen in the hydrodynamic case.

When a magnetic field is present, the additional shocks form to transport vorticity away from the interface because in MHD, a contact discontinuity cannot support a tangential velocity jump in the presence of a non-parallel magnetic field. To understand why this is so, consider a discontinuity in the plane $x = 0$, across which ρ, p and B_x are continuous and non-zero, $u_x = u_z = B_y = B_z = 0$, while the tangential velocity u_y is discontinuous and is given by,

$$u_y(x) = [\bar{v} + \Delta v H(x)]/2,$$

where $H(x)$ is the Heaviside function. The electric field is then given by,

$$\mathbf{E} = -\mathbf{u} \times \mathbf{B} = [\bar{v} + \Delta v H(x)] B_x \hat{\mathbf{e}}_z/2,$$

where $\hat{\mathbf{e}}_z$ is the unit vector in the $z-$direction. Using this to evaluate the time

derivative of the magnetic field, we obtain,

$$\frac{\partial \mathbf{B}}{\partial t} = -\nabla \times \mathbf{E} = \Delta v \delta(x) B_x \hat{\mathbf{e}}_y / 2,$$

where $\delta(x)$ is the Dirac delta function. The magnetic field in the $y-$direction that develops as a result of this will produce a Lorentz force at the discontinuity. Thus the discontinuity is not a steady solution to the equations of ideal MHD.

In the simulations, the amplitude of the interface perturbation η is computed follows: Let ρ_4 and ρ_5 be the average densities immediately to the left and right of the interface, respectively, after the incident shock has interacted with the interface. The density midway though the thickness of the interface is then approximately,

$$\rho_{mid} = \frac{\rho_4 + \rho_5}{2}.$$

The interface amplitude is approximated as half the difference between the maximum and minimum values of z where $\rho = \rho_{mid}$;

$$\eta = \frac{\max\left(z : \rho = \rho_{mid}\right) - \min\left(z : \rho = \rho_{mid}\right)}{2}.$$

The values of z where $\rho = \rho_{mid}$ are computed using linear interpolation between the cell centered values. The η histories computed from the two simulations using this procedure are shown in Fig. 2.4. Also shown is the behavior predicted by the incompressible hydrodynamic impulse model of Richtmyer (1960), which was introduced in Section 1.1;

$$\dot{\eta} = \eta_0 k \Delta V \frac{\rho_5 - \rho_4}{\rho_5 + \rho_4}, \tag{2.7}$$

where ΔV is the magnitude of the impulse and k is the wavenumber of the perturbation. We take ΔV to be the mean velocity imparted to the interface during the shock refraction process, which is $1.0709\sqrt{p_0/\rho_1}$ for the parameters considered here. Following the discussion in Section 1.1, the post-shock value of η_0 is used as the reflected wave is a shock. For the simulation with $B = 0$, η initially grows linearly

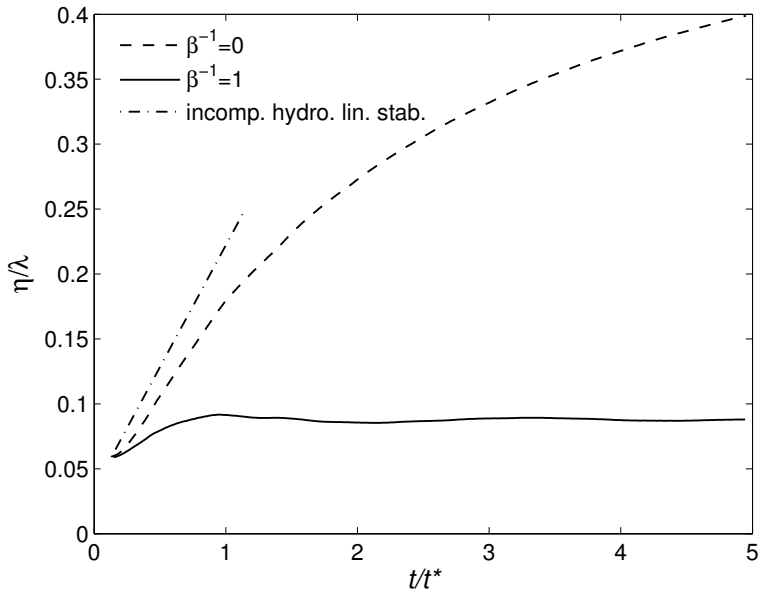

Figure 2.4: Interface perturbation amplitude histories from simulations with $M = 2$, $\rho_2/\rho_1 = 3$, $\eta_0/\lambda = 0.1$, $\gamma = 5/3$, and $B = 0$ or $\beta = 1$. The behavior according to the incompressible hydrodynamic linear stability analysis (Richtmyer, 1960) is also shown.

after a small discrepancy following the shock interaction. Such a discrepancy was also seen in the $M = 1.2$, $\eta_0/\lambda = 0.064$ hydrodynamic simulations summarized by Brouillette (2002). The linear growth rate after the discrepancy is less (approximately 18%) than that predicted by Eq. 2.7. This is similar to the findings of Cook et al. (2004) for the Rayleigh-Taylor instability. They observe that the growth factor of the interface is approximately 10% less than the value from linear stability theory for $\eta_0/\lambda = 0.1$. This disagreement is attributed to non-linear effects (Cook et al., 2004). In the $M = 1.2$, $\eta_0/\lambda = 0.064$ hydrodynamic results summarized by Brouillette (2002), the growth rates from the front tracking simulation of Holmes et al. (1995) and the experiments of Benjamin (1992) are consistently below that predicted by the impulse model. At $t/t^* \approx 1$, the interface begins to roll-up and the growth rate starts to decrease. The behavior of the interface in the simulation with $\beta = 1$ is quite different. The interface amplitude does increase initially, but the growth rate does not appear to be constant as in the hydrodynamic case. The growth rate then decays to zero at $t/t^* \approx 0.95$, after which η appears to undergo long period oscil-

lations about a mean value of 0.088λ. This is a factor of approximately 1.5 greater than the amplitude of the interface immediately after shock compression.

2.5 Discussion

The results of the MHD RMI simulations with a sinusoidally perturbed interface are in qualitative agreement with the simulations of Samtaney (2003), in which the interface was planar and oblique: When a magnetic field is present, additional MHD shocks are generated during the shock refraction process that transport vorticity away from the density interface, suppressing the growth of the RMI. The most significant result to arise from the simulations presented in this chapter is that the interface amplitude still exhibits some growth in the presence of a magnetic field. The behavior of the interface amplitude in this case, a short period of growth followed by oscillations about a constant mean, was not reported by Samtaney and warrants further investigation. The physics behind this behavior is explored in the chapters that follow.

Chapter 3

Incompressible Linear Theory

3.1 Introduction

Our goal is to understand the effect of a magnetic field on the RMI of a sinusoidally perturbed density interface when conducting fluids are involved. We consider the case where the magnetic field is aligned with the motion of the shock. The initial condition for this flow is illustrated in Fig. 3.1(a). As a model for this flow, we will examine the growth of a sinusoidally perturbed interface separating incompressible conducting fluids that is impulsively accelerated at $t = 0$. The setup for the model problem is illustrated in Fig. 3.1(b). This problem is characterized by the normalized densities on either side of the interface ρ_1/ρ^* and ρ_2/ρ^*, the ratio of initial perturbation amplitude to its wavelength η_0/λ, the non-dimensional strength of the applied magnetic field $\beta^{-1} = B^2/(2p_0)$, and the normalized magnitude of the impulse $\Delta V\sqrt{\rho^*/p_0}$. Here, p_0 is the initial pressure of the flow and we choose ρ^* to be ρ_1 from the corresponding shock driven flow.

3.2 Formulation

3.2.1 Governing equations of ideal, incompressible MHD

In this investigation, it is convenient to consider solutions to the linearized equations of ideal, incompressible MHD in a non-inertial reference frame that has acceleration

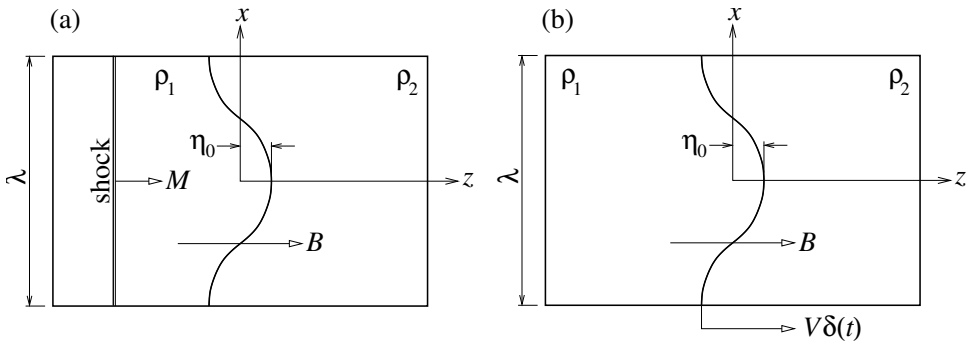

Figure 3.1: (a) Initial condition geometry for compressible RM instability. (b) Geometry for incompressible model problem.

$\Delta V \delta(t)$ in the z-direction. Here, $\delta(t)$ is the Dirac delta function and $\Delta V \ll c$, where c is the speed of light. In this reference frame, the ideal incompressible equations are

$$\nabla \cdot (\mathbf{u}) = 0 \ , \tag{3.1}$$

$$\rho \frac{\partial \mathbf{u}}{\partial t} + \rho \left(\mathbf{u} \cdot \nabla \right) \mathbf{u} = -\nabla p + (\nabla \times \mathbf{B}) \times \mathbf{B} - \rho \Delta V \delta(t) \mathbf{e_z} \ , \tag{3.2}$$

$$\nabla \cdot \mathbf{B} = 0 \ , \tag{3.3}$$

$$\frac{\partial \mathbf{B}}{\partial t} = \nabla \times (\mathbf{u} \times \mathbf{B}) \ . \tag{3.4}$$

Here, ρ is the density, p is the pressure, $\mathbf{u}$ is the velocity, $\mathbf{B}$ is the magnetic field, and $\mathbf{e_z}$ is the unit vector that points in the z-direction.

3.2.2 Base flow

Eqs. 3.1-3.4 are linearized about a base flow that results from the impulsive acceleration of an unperturbed interface. This flow has no x-dependence and zero vertical velocity (u). Our choice of reference frame results in the horizontal velocity (w) being zero for all time. The base flow pressure is found by integrating Eq. 3.2. The complete

base flow is thus

$$\rho_0(z) = \rho_1 + H(z)\,(\rho_2 - \rho_1)\,,$$
$$u_0 = 0,$$
$$w_0 = 0,$$
$$B_{x0} = 0,$$
$$B_{z0} = B,$$
$$p_0(z,t) = -\rho_1 \Delta V \delta(t) z - H(z)\,(\rho_2 - \rho_1)\,\Delta V \delta(t) z,$$

where $H(z)$ is the Heaviside function. When the interface is perturbed the density becomes $\rho_0(z-h)$, where $h(x,t)$ is the position of the interface and $h \ll \lambda$.

3.2.3 Linearized equations

The linearized equations are obtained by assuming that all flow quantities, except density, are of the form

$$q(x,z,t) = q_0(z,t) + q'(x,z,t),$$

where q' are small perturbations to the base flow. These expressions are then substituted into the governing equations; Eqs. 3.1-3.4. Neglecting terms involving products of perturbations, the resulting linearized equations are

$$\frac{\partial u'}{\partial x} + \frac{\partial w'}{\partial z} = 0, \tag{3.5}$$
$$\rho \frac{\partial u'}{\partial t} + \frac{\partial p'}{\partial x} = B\left(\frac{\partial B'_x}{\partial z} - \frac{\partial B'_z}{\partial x}\right), \tag{3.6}$$
$$\rho \frac{\partial w'}{\partial t} + \frac{\partial p'}{\partial z} = (\rho_2 - \rho_1)\,[H(z) - H(z-h)]\,\Delta V \delta(t), \tag{3.7}$$
$$\frac{\partial B'_x}{\partial x} + \frac{\partial B'_z}{\partial z} = 0, \tag{3.8}$$
$$\frac{\partial \mathbf{B}'}{\partial t} = B \frac{\partial \mathbf{u}'}{\partial z}. \tag{3.9}$$

Note that the forcing resulting from the impulse is non-zero only in a small region between $z = 0$ and the interface. We assume that all perturbations have the form

$$q'(x, z, t) = \hat{q}(z, t)e^{ikx}, \tag{3.10}$$

as we will see that the solution is not separable in z and t. We take our initial conditions to be at $t = 0^-$, just prior to the impulsive acceleration, when the velocity and magnetic field perturbations are zero. Taking the temporal Laplace transforms of Eqs. 3.5-3.9 outside of the forced region in each fluid gives

$$ikU_i + DW_i = 0, \tag{3.11}$$

$$s\rho_i U_i + ikP_i = B\left[DH_{x_i} - ikH_{z_i}\right], \tag{3.12}$$

$$s\rho_i W + DP_i = 0, \tag{3.13}$$

$$ikH_{x_i} + DH_{z_i} = 0, \tag{3.14}$$

$$sH_{x_i} = BDU_i, \tag{3.15}$$

$$sH_{z_i} = BDW_i, \tag{3.16}$$

where U, W, H_x, H_z, and P are the temporal Laplace transforms of $\hat{u}$, $\hat{w}$, $\hat{B}_x$, $\hat{B}_z$, and $\hat{p}$, respectively, $i = 1$ or 2, and $D \equiv \partial/\partial z$.

3.2.4 Spatial behavior

Eqs. 3.11-3.16 can be combined to give the following ODE for W:

$$\left(D^2 - \frac{\rho_i s^2}{B^2}\right)\left(D^2 - k^2\right)W_i = 0, \tag{3.17}$$

which has the general solution

$$W_i = A_i(s)e^{kz} + B_i(s)e^{-kz} + C_i(s)e^{sz/C_{Ai}} + D_i(s)e^{-sz/C_{Ai}}, \tag{3.18}$$

where $C_{Ai} = B/\sqrt{\rho_i}$ is the Alfvén wave speed in fluid i. The inverse Laplace transforms (ILTs) of the first two terms have the form $f(t)e^{\pm kz}$ while the ILTs of the last two terms have the form $H(t \pm z/C_{Ai})f(t \pm z/C_{Ai})$. This causes the solution to be non-separable in z and t.

3.2.5 Boundary conditions

Solutions to Eqs. 3.5-3.9 are subject to a number of boundary conditions. The perturbations must be bounded as $|z| \to \infty$, thus $A_2(s) = 0$ and $B_1(s) = 0$. Also, we require that there be no incoming waves from $z = \pm\infty$, thus $C_2(s) = 0$ and $D_1(s) = 0$. Note that we have assumed $B > 0$ and $k > 0$. The resulting expressions for W_1 and W_2 are

$$W_1(z, s) = A_1(s)e^{kz} + C_1(s)e^{sz/C_{A1}}, \tag{3.19}$$

$$W_2(z, s) = B_2(s)e^{-kz} + D_2(s)e^{-sz/C_{A2}}. \tag{3.20}$$

At the contact ($z = h(x, t) = \eta(t)e^{ikx}$), w', B'_x, and B'_z must be continuous (Chandrasekhar, 1961). Taking the Laplace transforms of these variables and using Eqs. 3.11-3.16 to express each in terms of W, these boundary conditions become, to leading order in h,

$$[W]_{z=0} = 0, \tag{3.21}$$

$$[DW]_{z=0} = 0, \tag{3.22}$$

$$\left[D^2W\right]_{z=0} = 0, \tag{3.23}$$

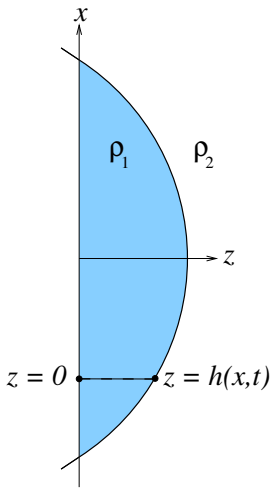

Figure 3.2: The region (shaded area) and integration path (dashed line) considered in deriving the dynamic condition.

where $[q]_{z=0} \equiv q_2|_{z=0} - q_1|_{z=0}$. Using Eq. 3.19 and Eq. 3.20 to express these boundary conditions in terms of the unknown coefficients, we obtain,

$$A_1 + C_1 = B_2 + D_2, \tag{3.24}$$

$$kA_1 + \frac{sC_1}{C_{A1}} = -kB_2 - \frac{sD_2}{C_{A2}}, \tag{3.25}$$

$$k^2 A_1 + \frac{s^2 C_1}{C_{A1}^2} = k^2 B_2 + \frac{s^2 D_2}{C_{A2}^2}. \tag{3.26}$$

The continuity of pressure across the contact is referred to as the dynamic condition. We derive the dynamic condition appropriate here as follows: Consider the fluid in a thin region between the contact and $z = 0$, where x is such that $h(x,t) > 0$. Such a region is shown in Fig. 3.2. From Eq. 3.7, the linearized z-momentum equation in this region is

$$\rho_1 \frac{\partial w'}{\partial t} = -\frac{\partial p'}{\partial z} + (\rho_2 - \rho_1)\Delta V \delta(t) \ .$$

Integrating this equation with regard to z from 0 to $h(x,t)$ and rearranging yields

$$p'(x,h,t) - p'(x,0,t) = (\rho_2 - \rho_1)\Delta V \delta(t) h - \rho_1 \int_0^h \frac{\partial w'}{\partial t} dz. \tag{3.27}$$

The integral on the right is a higher order term and hence can be neglected. As p' is

continuous across the contact, $p'(x,h,t) = p'_2(x,h,t)$, which to leading order is given by $p'_2(x,0,t)$. Using this and $p'(x,0,t) = p'_1(x,0,t)$, to leading order Eq. 3.27 becomes

$$p'_2(x,0,t) - p'_1(x,0,t) = (\rho_2 - \rho_1)\Delta V \delta(t)\eta(t)e^{ikx}.$$

Taking the Laplace transform of this equation and using Eq. 3.11, Eq. 3.12, Eq. 3.15, and Eq. 3.16 to express P_i in terms of W_i, we obtain

$$\frac{B^2}{sk^2}\left(D^3W_2 - DW_2 - D^3W_1 + DW_1\right) + \frac{s}{k^2}\left(\rho_1 DW_1 - \rho_2 DW_2\right) = \left(\rho_2 - \rho_1\right)\Delta V \eta(0).$$

Using the forms for W_1 and W_2 given in Eq. 3.19 and Eq. 3.20, respectively, the dynamic condition can be expressed as

$$\rho_1\left(\frac{sA_1}{k} + \frac{BC_1}{\sqrt{\rho_1}}\right) + \rho_2\left(\frac{sB_2}{k} + \frac{BD_2}{\sqrt{\rho_2}}\right) = \left(\rho_2 - \rho_1\right)\Delta V \eta_0. \tag{3.28}$$

The result is the same if we consider a region where $h(x,t) < 0$.

3.3 Solution

Eqs. 3.24-3.26 and Eq. 3.28 are solved for the four unknown coefficients; $A_1(s)$, $B_2(s)$, $C_1(s)$, and $D_2(s)$. After considerable algebra, the resulting coefficients can be expressed as,

$$A_1(s) = K_A \frac{s(s+\alpha_1)}{(s-\alpha_1)(s-\sigma-i\tau)(s-\sigma+i\tau)}, \tag{3.29}$$

$$B_2(s) = K_A \frac{s(s+\alpha_2)}{(s-\alpha_2)(s-\sigma-i\tau)(s-\sigma+i\tau)}, \tag{3.30}$$

$$C_1(s) = K_C \frac{s+\alpha_2}{(s-\alpha_1)(s-\sigma-i\tau)(s-\sigma+i\tau)}, \tag{3.31}$$

$$D_2(s) = K_D \frac{s+\alpha_1}{(s-\alpha_2)(s-\sigma-i\tau)(s-\sigma+i\tau)}, \tag{3.32}$$

where,

$$\alpha_1 = \frac{Bk}{\sqrt{\rho_1}}, \tag{3.33}$$

$$\alpha_2 = \frac{Bk}{\sqrt{\rho_2}}, \tag{3.34}$$

$$\sigma = -\frac{Bk\left(\sqrt{\rho_1}+\sqrt{\rho_2}\right)}{\rho_1+\rho_2}, \tag{3.35}$$

$$\tau = \frac{\left[B^2k^2\left(\rho_1+\rho_2-2\sqrt{\rho_1\rho_2}\right)\right]^{1/2}}{\rho_1+\rho_2}, \tag{3.36}$$

and

$$K_A = k\Delta V\eta_0\mathcal{A}, \tag{3.37}$$

$$K_C = -\frac{2Bk^2\Delta V\eta_0\mathcal{A}\rho_2}{\sqrt{\rho_1}\rho_2+\sqrt{\rho_2}\rho_1}, \tag{3.38}$$

$$K_D = \frac{\rho_1}{\rho_2}K_C. \tag{3.39}$$

The Atwood number $\mathcal{A} \equiv (\rho_2-\rho_1)/(\rho_2+\rho_1)$. The inverse Laplace transforms of $A_1(s)$, $B_2(s)$, $C_1(s)$, and $D_2(s)$, respectively, can be expressed as

$$a_1(t) = K_A\left[\frac{2\alpha_1^2e^{\alpha_1 t}}{(\alpha_1-\sigma)^2+\tau^2} + \Re\left(\frac{(\sigma+i\tau)(\alpha_1+\sigma+i\tau)e^{(\sigma+i\tau)t}}{i\tau(\sigma+i\tau-\alpha_1)}\right)\right], \tag{3.40}$$

$$b_2(t) = K_A\left[\frac{2\alpha_2^2e^{\alpha_2 t}}{(\alpha_2-\sigma)^2+\tau^2} + \Re\left(\frac{(\sigma+i\tau)(\alpha_2+\sigma+i\tau)e^{(\sigma+i\tau)t}}{i\tau(\sigma+i\tau-\alpha_2)}\right)\right], \tag{3.41}$$

$$c_1(t) = K_C\left[\frac{(\alpha_1+\alpha_2)e^{\alpha_1 t}}{(\alpha_1-\sigma)^2+\tau^2} + \Re\left(\frac{(\alpha_2+\sigma+i\tau)e^{(\sigma+i\tau)t}}{i\tau(\sigma+i\tau-\alpha_1)}\right)\right], \tag{3.42}$$

$$d_2(t) = K_D\left[\frac{(\alpha_1+\alpha_2)e^{\alpha_2 t}}{(\alpha_2-\sigma)^2+\tau^2} + \Re\left(\frac{(\alpha_1+\sigma+i\tau)e^{(\sigma+i\tau)t}}{i\tau(\sigma+i\tau-\alpha_2)}\right)\right]. \tag{3.43}$$

The above expressions are not valid if $\tau = 0$, but this requires that either $B = 0$, $k = 0$, or $\rho_1 = \rho_2$, which correspond to cases that are not of interest here. In the general case, from Eq. 3.19 and Eq. 3.20, the complete solutions for w in each fluid

are

$$w_1 = \left[a_1(t)e^{kz} + H(t + z/C_{A1})c_1(t + z/C_{A1})\right] e^{ikx}, \tag{3.44}$$

$$w_2 = \left[b_2(t)e^{-kz} + H(t - z/C_{A2})d_2(t - z/C_{A2})\right] e^{ikx}. \tag{3.45}$$

3.4 Solution features

3.4.1 Boundedness of velocity

In our solution for w, the exponents $\alpha_1 t$ and $\alpha_2 t$ are positive, admitting the possibility that the maximum velocity grows exponentially in time. This does not occur for the following reasons: First consider fluid 2. For $0 < z < C_{A2}t$, the terms in w_2' involving the exponent $\alpha_2 t$ are

$$\left[\frac{2K_B\alpha_2^2}{(\alpha_2 - \sigma)^2 + \tau^2}e^{\alpha_2 t - kz} + \frac{K_D(\alpha_1 + \alpha_2)}{(\alpha_2 - \sigma)^2 + \tau^2}e^{\alpha_2(t - z/C_{A2})}\right] e^{ikx}.$$

Now, because $\alpha_2/C_{A2} = k$ these are equal to

$$\frac{1}{(\alpha_2 - \sigma)^2 + \tau^2}\left[2K_B\alpha_2^2 + K_D(\alpha_1 + \alpha_2)\right] e^{\alpha_2 t - kz + ikx} = 0.$$

The equality holds because $2K_B\alpha_2^2 + K_D(\alpha_1 + \alpha_2) = 0$. Thus w_2' does not grow exponentially in time for $0 < z < C_{A2}t$. For $z > C_{A2}t$, the term in w_2' involving the exponent $\alpha_2 t$ has the form

$$Ke^{\alpha_2 t - kz}e^{ikx} = Ke^{-k(z - C_{A2}t)}e^{ikx}. \tag{3.46}$$

This term decays exponentially in the moving co-ordinate $z - C_{A2}t$, which is positive for $z > C_{A2}t$. Thus the maximum of w_2' does not grow exponentially in time. Similar arguments hold in fluid 1.

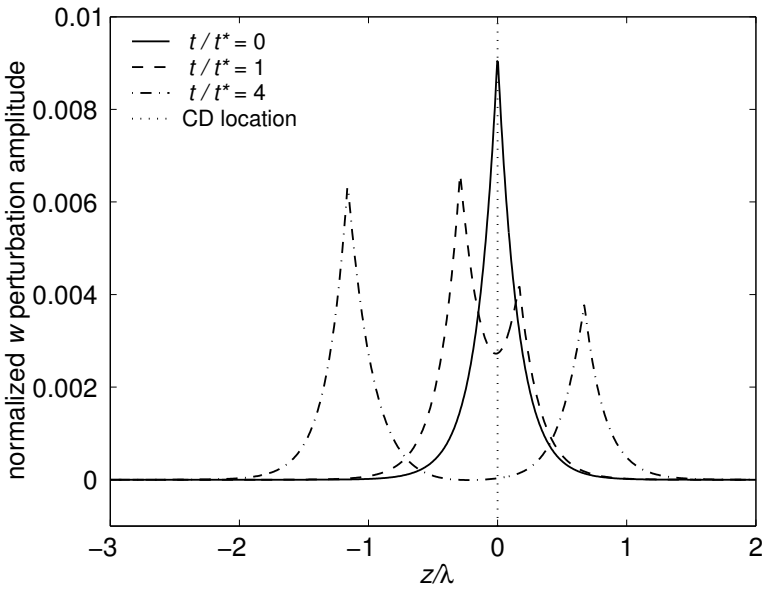

Figure 3.3: Profiles of $\hat{w}(z,t)\sqrt{\rho^*/p_0}$ at $t/t^* = 0$, $t/t^* = 1$, and $t/t^* = 4$, for $\rho_1/\rho^* = 1.48372$, $\rho_2/\rho^* = 4.43159$, $\Delta V\sqrt{\rho^*/p_0} = 0.319125$, $\eta_0/\lambda = 0.00799276$, and $\beta = 16$. Here $t^* \equiv \lambda\sqrt{\rho^*/p_0}$. The maxima of $\hat{w}(z,t)$ coincide with the Alfvén fronts.

3.4.2 Initial solution and growth rate

Profiles of $\hat{w}(z,t)$ at various times are shown in Fig. 3.3 for one set of parameters. The initial ($t = 0^+$) velocity distribution,

$$w(x,z,0^+) = \eta_0 k \Delta V \mathcal{A} e^{-k|z|+ikx},$$

is identical to the steady velocity distribution that arises from the hydrodynamic ($B = 0$) case. This implies that the initial growth rate of the interface, which to leading order is given by $\hat{w}_i(0,0)$, is unaffected by the presence of a magnetic field. Indeed, from Eq. 3.44 or Eq. 3.45 it can be shown that this initial growth rate is,

$$\left.\frac{\partial \eta}{\partial t}\right|_{t=0} = \eta_0 k \Delta V \mathcal{A}, \tag{3.47}$$

as in the hydrodynamic case (Richtmyer, 1960). This is consistent with the fact that the baroclinic generation of vorticity ω is unaffected by the presence of the magnetic

field.

3.4.3 Circulation distribution

On any interface with unit tangent $\hat{\mathbf{t}}$, the circulation per unit length Δu is given by,

$$\Delta u = \left[\mathbf{u} \cdot \hat{\mathbf{t}}\right].$$

For the interfaces in our problem, $\mathbf{u} \cdot \hat{\mathbf{t}} = u$ to leading order. Using the fact that $u = iDw/k$,

$$\Delta u = [u] = \frac{i}{k}\left[Dw\right] = \frac{i}{k}\left[D\hat{w}\right]e^{ikx}.$$

Thus the gradient discontinuities in $\hat{w}$ seen in Fig. 3.3 indicate the presence of interfaces that carry circulation on a half period. At $t = 0^+$, Fig. 3.3 shows that circulation is present on the density interface at $z = 0$. This was baroclinically generated during the impulsive acceleration of the interface. Away from the interface the flow is irrotational at $t = 0^+$, thus the total circulation in a half period of the domain must be equal to,

$$\Gamma_{1/2} = \frac{i}{k}\left[D\hat{w}\right]_{z=0,\,t=0}\int_0^{\lambda/2} e^{ikx}dx = 4\eta_0\Delta V\mathcal{A}. \tag{3.48}$$

In MHD, the incompressible vorticity equation,

$$\frac{\partial\omega}{\partial t} + (\mathbf{u}\cdot\nabla)\omega = (\omega\cdot\nabla)\mathbf{u} + \frac{\nabla\rho\times\nabla p}{\rho^2} + \frac{\nabla\times[(\nabla\times\mathbf{B})\times\mathbf{B}]}{\rho}, \tag{3.49}$$

has an additional term involving the magnetic field. The additional term implies that even in the absence of baroclinic generation, vortex lines are not necessarily material lines as they are in hydrodynamics. For $t > 0^+$, $\hat{w}$ is smooth around $z = 0$, indicating that the circulation has been removed from the density interface. Instead, circulation is carried by two fronts that propagate at the local Alfvén speed in each fluid. These fronts correspond to the locations where the Heaviside functions change magnitude.

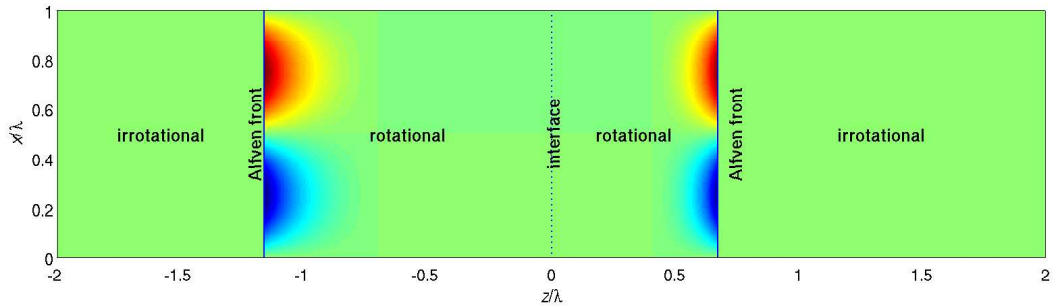

Figure 3.4: Vorticity field at $t/t^* = 4$ for $\rho_1/\rho^* = 1.48372$, $\rho_2/\rho^* = 4.43159$, $\Delta V\sqrt{\rho^*/p_0} = 0.319125$, $\eta_0/\lambda = 0.00799276$, and $\beta = 16$. Here $t^* \equiv \lambda\sqrt{\rho^*/p_0}$.

At their locations, the solution satisfies the following set of jump conditions:

$$[w'] = 0 \ , \tag{3.50}$$

$$[B_z'] = 0 \ , \tag{3.51}$$

$$[p'] = 0 \ , \tag{3.52}$$

$$[u'] = -sign(z)\frac{1}{\sqrt{\rho_0}}\,[B_x'] \, . \tag{3.53}$$

These correspond to the MHD Rankine-Hugoniot relations (in the shock stationary reference frame) for a discontinuity with a small amplitude corrugation, linearized about a uniform flow propagating at the Alfvén speed either parallel or anti-parallel to the magnetic field.

In the smooth regions of the flow, the vorticity is given by,

$$\omega = \frac{\partial w}{\partial x} - \frac{\partial u}{\partial z} = \frac{i}{k}\left(k^2 w - D^2 w\right) . \tag{3.54}$$

By substituting our solution for w into the above equation, we find that the flow is irrotational upstream of the Alfvén fronts in each fluid. Downstream of the Alfvén fronts, however, we find that the vorticity is non-zero. This is illustrated in Fig. 3.4, which shows the vorticity field for one particular case. Note that the vorticity decays exponentially downstream of each Alfvén front.

3.4.4 Interface behavior

The value of $\hat{w}(z,t)$ at $z=0$ is the growth rate of the interface. From Fig. 3.3, it can be seen that as t increases and the Alfvén fronts propagate away from the interface, carrying away the majority of the vorticity produced by the impulsive acceleration, the growth rate of the interface decays to zero. Thus the instability of the interface is suppressed and its amplitude asymptotes to a constant value. For $t \to \infty$, the interface amplitude tends to

$$\eta_\infty = \eta_0 + \int_0^\infty \hat{w}(0,t)dt = \eta_0 \left[1 + \frac{\Delta V}{B}(\sqrt{\rho_2} - \sqrt{\rho_1})\right]. \tag{3.55}$$

This shows that the change in interface amplitude is inversely proportional to B. Thus for $B \to 0$, $\eta_\infty \to \infty$, which is in agreement with the result from hydrodynamic linear stability analysis (Richtmyer, 1960). Interestingly, η_∞ is independent of wavenumber. For finite times the interface amplitude is given by,

$$\eta(t) = \eta_0 + \int_0^t \hat{w}(0,T)dT = \eta_\infty - (\eta_\infty - \eta_0)e^{\sigma t}\cos\tau t, \tag{3.56}$$

where σ and τ are as defined in Eq. 3.35 and Eq. 3.36, respectively.

3.5 Summary

In conclusion, we have examined the behavior of an impulsively accelerated perturbed interface separating incompressible conducting fluids of different densities, in the presence of a magnetic field that is parallel to the acceleration. This was done by analytically solving the appropriate linearized initial value problem. We find that the initial growth rate of the interface is unaffected by the presence of a magnetic field, hence the perturbations still grow in this case. The growth rate then decays due to the transport of vorticity via Alfvén fronts, resulting in the interface amplitude asymptoting to a constant value. The difference between the initial and final interface amplitudes is inversely proportional to the magnetic field magnitude. Thus

the instability of the interface is suppressed by the presence of the magnetic field, but there is still growth of the interface perturbations at early times.

Chapter 4

Comparison with Simulation

4.1 Introduction

In Chapter 3 a linear model was developed for the MHD Richtmyer-Meshkov instability. The model differs from the full MHD Richtmyer-Meshkov instability in that it is incompressible, linear, and is driven by an impulse rather than by the impact of a shock wave. In this chapter, the performance of the model is assessed for a variety of cases by comparing it to the results of compressible numerical simulations. In each case, an impulse driven linearized (IDL) simulation, a shock driven linearized (SDL) simulation, and a non-linear (NL) simulation were carried out. This allows the effects on the flow of compressibility, shock acceleration, and non-linearity to be assessed systematically: differences between the linear model and an IDL simulation are mainly due to the effects of compressibility, differences between IDL and SDL simulations are due to the effects of shock rather than impulsive acceleration, and differences between SDL and NL simulations are due to non-linear effects.

It is expected that the effects of compressibility increase with shock Mach number M, while non-linear effects increase with the initial amplitude of the interface η_0. From the linear model, the propagation speeds of the fronts that carry circulation away from the interface scale like C_A. This must be small compared to the sound speed, which corresponds to $\beta \equiv 2a^2/\gamma C_A^2$ being large, if these fronts are not to interact with the shocks present in the compressible case. Thus it is anticipated that

the model will be most accurate for a flow characterized by small M, small η_0, and large β. The performance of the model for such a set of parameters is analyzed as baseline case. We then examine how the performance of the model is affected as M, η_0, and β^{-1} are increased.

4.2 Simulation techniques

4.2.1 Numerical method for linearized simulations

The linearized simulations presented in this chapter were carried out using a method developed by Samtaney (2004) for obtaining numerical solutions to the linearized ideal MHD equations when the base flow is temporally evolving. In this method, the equations of compressible ideal MHD presented in Section 2.2 are specialized to two dimensions; x and z. The solution is then assumed to have the form,

$$U(x, z, t) = U^o(z, t) + \epsilon\, \hat{U}(z, t) \exp(ikx),$$

where $\epsilon \ll 1$, $U^o(z, t)$ is an unsteady one-dimensional base flow, and $\epsilon\hat{U}(z, t) \exp(ikx)$ is the perturbation to the base flow. A finite volume upwind approach is adopted to solve for both the base flow and the perturbations. The equations are integrated in time using a third order TVD Runge-Kutta scheme and the fluxes are evaluated using Roe's method. The details of the method are described in Appendix B.

4.2.2 Setup for shock driven linearized simulations

Let us first consider the initial conditions for the base flow of an SDL simulation. Prior to the interaction of the incident shock with the density interface, which is unperturbed in the base flow, we designate the quiescent conditions to the left ($z < z_{if}$) and right ($z > z_{if}$) of the interface as states 1 and 2, respectively. The conditions downstream of the incident shock are referred to as state 3. For given values of γ and the incident shock Mach number M, state 3 is obtained from the normal shock

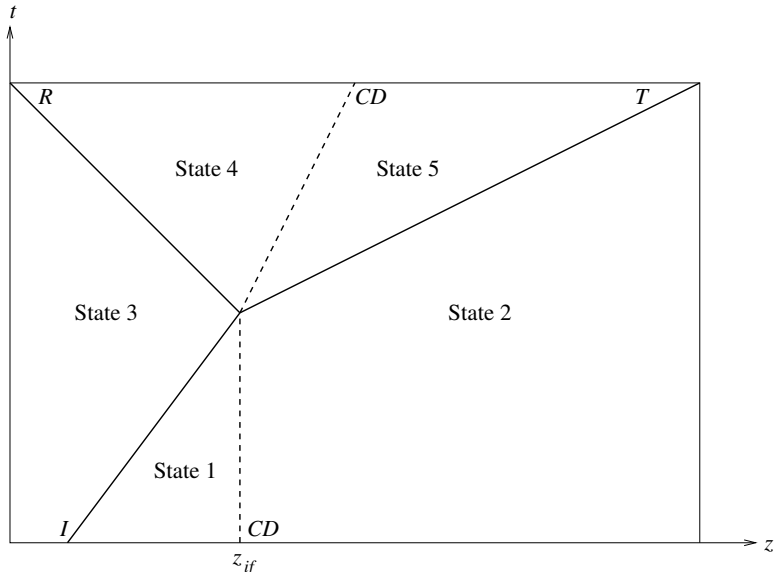

Figure 4.1: Illustration of the base flow for SDL simulations in the $z - t$ plane. The lines shown are the paths of the discontinuities in the flow. I, T, and R designate the incident, transmitted, and reflected shocks, respectively, while CD designates the contact discontinuity.

relations for an ideal gas. For the range of parameters considered in this thesis, the interaction of the incident shock with the interface generates a reflected shock and a transmitted shock. The conditions downstream of the reflected and transmitted shocks are referred to as states 4 and 5, respectively. These states are shown in Fig. 4.1, which shows the paths of the discontinuities in the base flow in the $z - t$ plane.

In the initial condition for the base flow, the incident shock is represented by a sharp discontinuity located at $z_{shock} = z_{if} - \lambda/5$. The flow is initialized to state 3 for $z < z_{shock}$ and state 1 for $z > z_{shock}$. For $z > z_{shock}$, the base flow density is set to,

$$\rho^o(x,0) = \frac{1}{2}\left\{(\rho_2 + \rho_1) + (\rho_2 - \rho_1)\tanh[\alpha(z - z_{if})]\right\},$$

to represent the density interface. With this initial condition, the base flow for an SDL simulation is the numerical solution to the Riemann problem that arises from the interaction of a shock with an unperturbed density interface. The only non-zero

perturbation at $t = 0$ is that in density, which approximates a delta function as follows;

$$\hat{\rho}(z,0) = -2\alpha(\rho_R - \rho_L)\frac{\exp[2\alpha(z - z_{if})]}{\{1 + \exp[2\alpha(z - z_{if})]\}^2}. \tag{4.1}$$

For all simulations we chose $\alpha = 80$. Note that the initial perturbation amplitude of the interface, η_0, has been scaled out of the problem. For comparison with the results of NL simulations and the incompressible linear model, the scaled perturbations from the linearized simulations must be multiplied by η_0.

4.2.3 Setup for impulse driven linearized simulations

For IDL simulations, the base flow is initialized to state 4 for $z < z_{if}$ and state 5 for $z > z_{if}$. These are the post-shock states from the Riemann problem described in the previous section. The sharp interface between these two uniform states is approximated by hyperbolic tangent profile, with all quantities having the form:

$$q(z,t) = \frac{1}{2}\left\{q_L + q_R + (q_R - q_L)\tanh[\alpha(z - z_{if})]\right\},$$

where the subscripts L and R indicate values to the left and right of the interface, respectively. The perturbations are initialized as described in Section 4.2.2. When scaling the perturbations from IDL simulations for comparison with other results, the initial perturbation amplitude of the interface is taken from the corresponding NL simulation immediately after the interface has been compressed by the passage of the shock wave. These same post-shock initial conditions are used in the incompressible linear model.

4.2.4 Setup for non-linear simulations

The non-linear simulations were carried out with a non-linear compressible MHD solver developed by Ravi Samtaney. It uses the 8-wave upwinding formulation of Powell et al. (1999a) within an unsplit upwinding method (Colella, 1990a). The solenoidal property of the magnetic field is enforced at each time step using a pro-

jection method. A constrained transport step is then used remove divergence modes with a centered finite difference representation. This uses the formulation prescribed by Toth (2000). A detailed description of the solver is presented in Appendix A. The setup for the NL simulations is the same as for the initial simulations presented in Chapter 2, except with different parameter values. The setup for these simulations is detailed in Section 2.3.

4.2.5 Characterization of interface behavior

In the linearized simulations, the interface corresponds to the location where the density perturbation is maximum. The interfacial growth rate $\dot{\eta}$ is approximated by the magnitude of the z-velocity perturbation at this location. The interface amplitude η_{lin} is then computed by numerically integrating $\dot{\eta}$. At time-step N, η_{lin} is given by,

$$\eta_{lin} = \eta_0 + \sum_{n=1}^{n=N} \dot{\eta}_n \Delta t_n,$$

where the subscript n denotes a quantity is evaluated at the nth time-step. In the NL simulations, the amplitude of the interface perturbations is computed using the procedure defined in Section 2.4.

For simulations where the interface is shock accelerated, the time origin of the interface amplitude histories is shifted to the point where the amplitude is minimum. This is done to allow direct comparison to the results arising from an impulsive acceleration at $t = 0$. The interface amplitude histories obtained from the simulations must be quantitatively compared to the behavior from the incompressible linear model, which is given by Eq. 3.56;

$$\eta(t) = \eta_\infty - (\eta_\infty - \eta_0) e^{\sigma t} \cos \tau t.$$

Here, η_∞ is the saturation value of the interface amplitude, while σ governs the saturation timescale. As $|\tau| < |\sigma|$ for $\rho_1 \neq \rho_2$, the oscillations due to the sinusoidal factor are not highly visible. For the simulations, values of these parameters can be

estimated by fitting the following function to the amplitude histories;

$$\eta_{fit}(t) = \eta_\infty - (\eta_\infty - \eta_0)e^{\sigma(t-t_0)}\cos\tau(t-t_0). \tag{4.2}$$

This is done using a non-linear least squares fitting routine that determines the values of η_∞, σ, and t_0 that minimize the L2 norm of the residuals between the data from the simulations and the fitted function. The result of this procedure for a typical interface amplitude history from a NL simulation (η_{NL}) is shown in Fig. 4.2(a). To understand why a value of τ is not also computed, consider Fig. 4.2(b), which shows the fitted function that results if τ is also determined by the routine. In this case the values of σ and τ have been determined such that the fitted function accurately captures the first of the long period oscillations that occur in η_{NL}. It is shown in Section 4.3, however, that these oscillations are due to the pressure field induced by the interaction of transverse waves downstream of the transmitted and reflected shocks and/or the reflection of outgoing waves from the shocks. These shocks are not present in the incompressible linear model, hence the oscillations should not appear in a fitted function that has the same form as the model η history. Adjusting the values of σ and τ to capture the first of these oscillations results an overestimate of σ (note that $\sigma < 0$), which is evident in the fitted function asymptoting to η_∞ slower than the phase average of η_{NL}. To avoid this problem, τ is set to the appropriate value from the incompressible linear model. The virtual origin t_0 is included in the fitted function to avoid an underestimate of σ due to the positive curvature of η_{NL} near $t = 0$. An example of such an underestimate is shown in Fig. 4.2(c).

4.3 Results

4.3.1 Baseline case

As a baseline case, we will study a shock accelerated interface with $M = 1.1$, $\beta = 16$, $\rho_2/\rho_1 = 3$, $\eta_0/\lambda = 0.01$ and $\gamma = 5/3$. In the following sections, we will investigate the effects of M, β, and η_0/λ on the performance of the linear model by individually

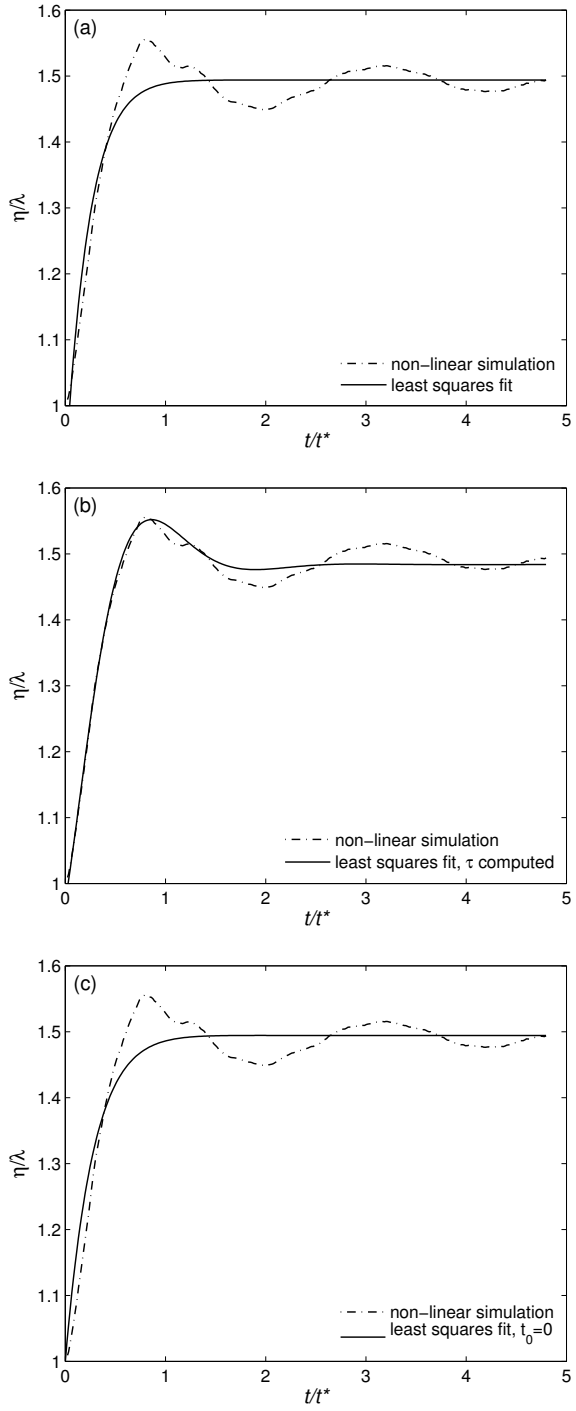

Figure 4.2: Interface amplitude history from a NL simulation with $M = 2$, $\beta = 1$, $\rho_2/\rho_1 = 3$, $\eta_0/\lambda = 0.1$ and $\gamma = 5/3$ along with fitted functions of the form shown in Eq. 4.2. For the function shown in (a) $\hat{\eta}_\infty$, $\hat{\sigma}$, and t_0 were calculated by the fitting routine. For the function shown in (b) τ was also calculated. For the function shown in (c) $t_0 = 0$.

varying them from their baseline values and comparing the results to those presented in this section. The linearized simulations of the baseline case were carried out in the domain $-10\lambda \leq z \leq 10\lambda$, which was discretized into $N_z = 3200$ control volumes. The simulations were run for $N_t = 6000$ time-steps with a CFL number of 0.5. All linearized simulations discussed in this chapter were carried out with the same domain, discretization, and CFL number, unless otherwise noted. For the NL simulation of the baseline case, $L_x = \lambda/2$, $L_z = 12\lambda$, $z_{if} = 7.06\lambda$, $N_x = 128$, and $N_z = 3072$, where these variables are as defined in Section 2.3. The simulation was run with a CFL number of 0.7 for the duration $T_{sim}/t^* = 5.6$, which is approximately double the time the linear model predicts for the interface to reach 99% of its final amplitude, t_{99}. All NL simulations discussed in this chapter were run with this CFL number for a duration that is approximately $2t_{99}$, unless otherwise noted. An NL simulation was also run with half the resolution in each direction. The η histories from the two different resolution simulations are shown in Fig. 4.3. Both histories contain spurious, time-step scale oscillations. As the amplitude of these oscillations does not grow with time, they do not appear to indicate the presence of a numerical instability. Fig. 4.3 shows that the two histories are very similar, with the main difference being a reduction in the amplitude of the spurious oscillations in the results of the higher resolution simulation. Thus the behavior of interest, specifically the growth of the interface, is not very sensitive to the resolution. It is important to note that as we are solving a set of equations with no physical dissipation to set a minimum length scale, numerical solutions to these equations will not formally converge with increasing resolution. This is because each increase in resolution will decrease the numerical dissipation in the simulation, and hence alter the solution. The higher resolution results are used for comparison to the linear model and the linearized simulations because of the smaller amplitude oscillations. In the remainder of this chapter, the η histories from the NL simulations are filtered to remove these oscillations before plotting.

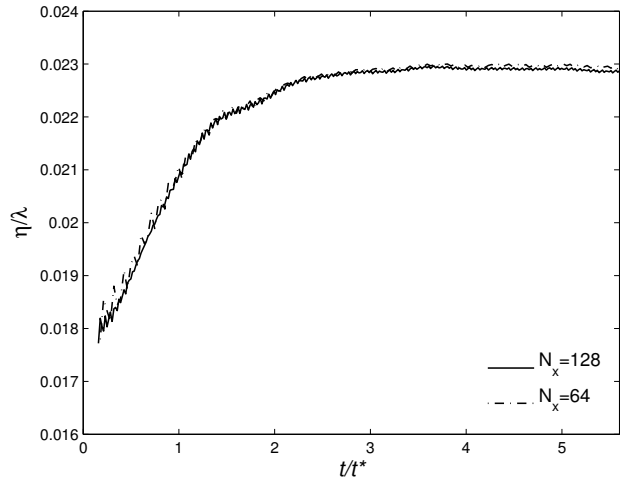

Figure 4.3: Interface amplitude histories from non-linear compressible simulations of a shock accelerated interface with $M = 1.1$, $\beta = 16$, $\rho_2/\rho_1 = 3$, $\eta_0/\lambda = 0.01$ and $\gamma = 5/3$. Results are shown from simulations with 64×1536 and 128×3072 mesh points.

Time evolution comparison

Fig. 4.4 shows the η histories from the linear model developed in Chapter 3 and the three simulations for the baseline case. The model η history is given by Eq. 3.56. The values of η_∞ and σ computed from these are shown in Table 4.1. The histories from the linearized simulations deviate from both the linear model and the NL simulation for a brief period just after the interface is accelerated. This may be due to the approximate initial density perturbation used in the linearized simulations, which is given by Eq. 4.1. There is close agreement between the behavior of the interface predicted by the linear model and the IDL simulation, with the final interface amplitudes being within approximately 0.2% of each other. The values of σ, which governs the time to saturation, agree to within 7.2%. The main difference between the two histories is the presence of small amplitude oscillations in the simulation result, the source of which will be discussed in the next subsection. The amplitude of these oscillations appears to decay with time and they are also seen in the histories from the SDL and NL simulations. Comparing the histories from the IDL and SDL simulations gives an indication of the effect of the interface being shock accelerated rather than impulsively accelerated. The qualitative behavior of the interface is similar in

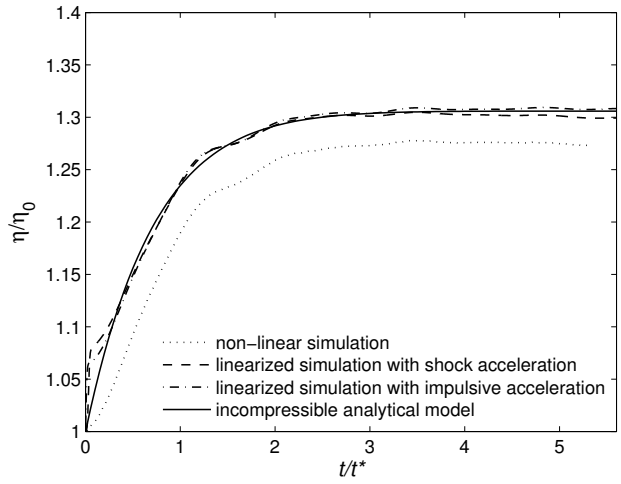

Figure 4.4: Interface amplitude histories from the current linear model and a compressible linearized simulation with an approximate impulsive acceleration, both with $\rho_1/\rho^* = 1.19223$, $\rho_2/\rho^* = 3.57529$, $\Delta V\sqrt{\rho^*/p_0} = 0.135324$, $\eta_0/\lambda = 0.00904708$, and $\beta = 16$, and both linearized and non-linear compressible simulations of a shock accelerated interface with $M = 1.1$, $\beta = 16$, $\rho_2/\rho_1 = 3$, $\eta_0/\lambda = 0.01$ and $\gamma = 5/3$.

both cases, but the shock acceleration appears to result in a slight reduction in the growth of the interface amplitude, with η_∞ being reduced by approximately 0.9%. In addition, the amplitudes from both the shock driven simulations is decreasing slightly near the end of the simulations. This is part of a long period oscillation. In the hydrodynamic case, oscillations in growth rate are known to be caused by the pressure field induced by the interactions of transverse waves downstream of the transmitted and reflected shocks (Brouillette, 2002). In addition, the oscillations may also be due to the reflection of outgoing waves from the shocks, which will be discussed in the next subsection. Comparing the histories from the IDL and NL simulations indicates that the main effect of non-linearity on the evolution of the interface is a significant decrease in its growth, with η_∞ being approximately 1.5% less in the NL simulation. The cause of the lower interface amplitudes in the NL simulation appears to be the low growth rates that occur immediately after the acceleration of the interface, which are significantly lower than those predicted by the linear model. Low growth rates at early times also occur in the absence of a magnetic field, as can be seen from the results of the initial simulation shown in Fig. 2.4. In that simulation, the growth

	Model	IDL Simulation	SDL Simulation	NL Simulation
η_∞/λ	0.0117237	0.0117465	0.0116413	0.0114644
σt^*	-1.38982	-1.28969	-1.42071	-1.31402

Table 4.1: Interface perturbation parameters from the linear model and simulations corresponding to a shock accelerated interface with $M = 1.1$, $\beta = 16$, $\rho_2/\rho_1 = 3$, $\eta_0/\lambda = 0.01$ and $\gamma = 5/3$.

rate is initially mitigated, then increases to close to the constant value predicted by the hydrodynamic impulse model, Eq. 1.1. The results of compressible linear models indicate that this behavior is typical of the RMI (Brouillette, 2002), and is expected as the impulse model predicts the asymptotic growth rate after the shocks are sufficiently far from the interface (Richtmyer, 1960). The low growth rates at early times do not significantly affect the extent to which the interface develops in the hydrodynamic case as the growth rate is then approximately constant until the interface enters the non-linear phase of its development. When a magnetic field is present, however, mitigation of the growth rate at early times significantly reduces the final amplitude of the interface as this is when the growth rate is predicted to be at its maximum.

Profile comparison

Profiles of u' and w' from the linear model developed in Chapter 3 and the IDL simulation of the baseline case are shown in Fig. 4.5 for $t/t^* = 4$. The w' profiles from the linear model are given by Eqs. 3.44 and 3.45 in fluids 1 and 2, respectively. The model u' profiles are computed from the w' profiles using Eq. 3.5 and the form of the perturbations given in Eq. 3.10 as follows:

$$u' = -\frac{1}{ik}\frac{\partial w'}{\partial z}.$$

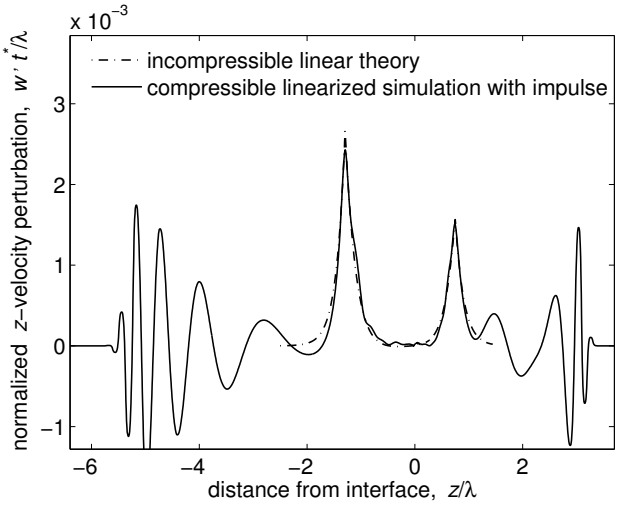

(a)

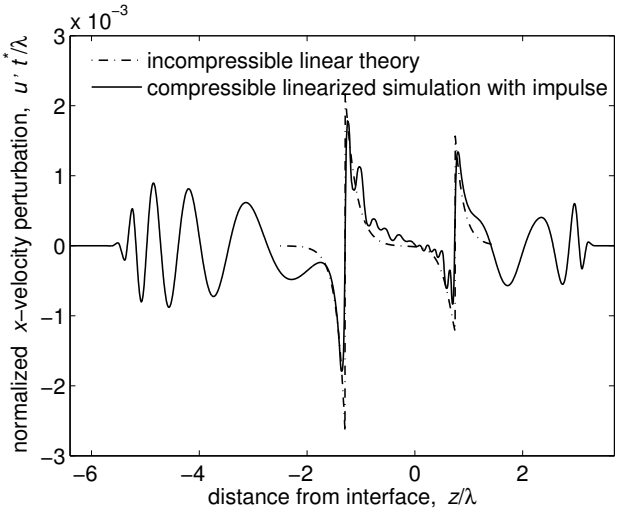

(b)

Figure 4.5: Profiles of (a) w' at $x = 0$ and (b) u' at $x = \lambda/4$ at $t/t^* = 4$ from the linear model and the IDL simulation corresponding to a shock accelerated interface with $M = 1.1$, $\beta = 16$, $\rho_2/\rho_1 = 3$, $\eta_0/\lambda = 0.01$ and $\gamma = 5/3$.

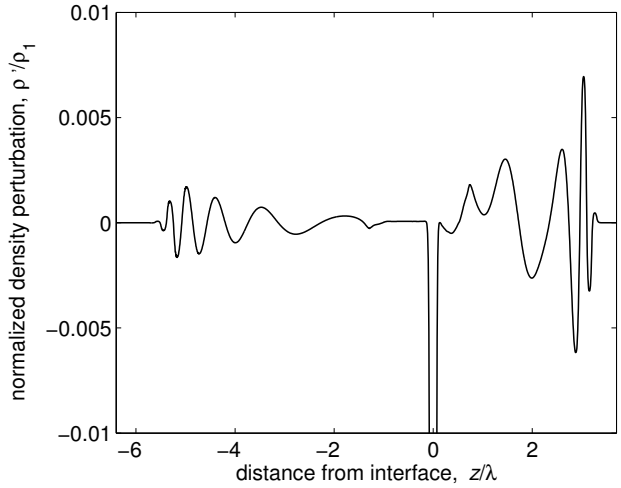

(a)

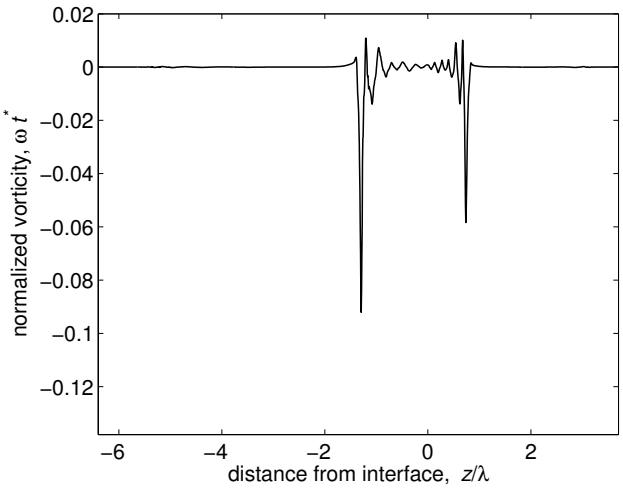

(b)

Figure 4.6: Profiles of (a) ρ' at $x = 0$ and (b) ω at $x = \lambda/4$ at $t/t^* = 4$ from the IDL simulation corresponding to a shock accelerated interface with $M = 1.1$, $\beta = 16$, $\rho_2/\rho_1 = 3$, $\eta_0/\lambda = 0.01$ and $\gamma = 5/3$.

The profiles of u' and w' are plotted at locations where the perturbation amplitudes are maximum, at $x = \lambda/4$ and $x = 0$, respectively. Additional waves can clearly be seen in the profiles from the IDL simulation. The leading edges of these waves propagate outward from the interface at the fast characteristic speed in each fluid. In this case, where the waves are propagating parallel to the base flow magnetic field, the fast characteristic speed corresponds to the sound speed $a_i = \sqrt{\gamma p_0/\rho_i}$, while both the slow and intermediate characteristic speeds are equal to the Alfvén speed $C_{Ai} = B/\sqrt{\rho_i}$. It can be seen from Fig. 4.6(a) that the additional waves are compressible as the density perturbations associated with them are non-zero, hence they cannot be represented in the incompressible linear model. The amplitudes of the velocity perturbations associated with the compressible waves are comparable those associated with the model. Despite this, Fig. 4.4 shows the linear model is able to predict the evolution of the interface in the IDL simulation quite accurately. The reason for this is that the behavior of the interface is governed by the vorticity distribution and the compressible waves do not have any vorticity associated with them, as can be seen from Fig. 4.6(b). The vorticity field from the simulation is dominated by the two peaks that approximately coincide with the locations of the Alfvén fronts in the linear model. Fig. 4.5 shows that the flow in this region and around interface, particularly w', is well represented by the Alfvén fronts and the incompressible flow field from the linear model, although it does not capture the small amplitude waves that appear near the interface. The reason a direct comparison of the vorticity fields has not been made is that the vorticity associated with the tangential velocity jumps across the Alfvén fronts in the linear model is infinite, while in the simulation the discontinuities have been smeared out over a few cells so that the vorticity is finite.

Now, the value of w' at $z = 0$ in the plotted profiles corresponds to the growth rate of the interface as the perturbations have a sinusoidal variation in x. Thus, when a wave with a w perturbation associated with it crosses the interface, it will cause a small oscillation in the interface amplitude. This is the cause of the oscillations that were noted earlier in the η histories from the compressible simulations. In the

IDL simulation, these oscillations decay with time as the high amplitude compressible waves propagate away from the interface at the beginning of the simulation and do not return.

Profiles of u' and w' from the linear model and the SDL simulation of the baseline case are shown in Fig. 4.7 at $t/t^* = 4$ in the simulation. The profiles from the linear model are shown at $t/t^* = 4 - (z_{if} - z_{shock})/(M\sqrt{\gamma})$, the approximate time after the acceleration of the interface in the simulation, because the acceleration occurs at $t = 0$ in the model. This adjustment is made whenever the linear model is compared to the results of a shock driven simulation. In the SDL simulation, the perturbations are restricted to the region between the two shocks in the base flow. The base flow downstream of the shocks is subsonic with respect to the fast characteristic speed, thus the compressible waves in the solution can catch up to the shocks and interact with them. This process can be seen occurring on the right side of Fig. 4.7, while Fig. 4.8 shows a close up picture of a wave intersecting the location transmitted shock at three different times, in the reference frame of the shock. The interaction of the waves with the shock can only produce reflected waves are the flow upstream of the shocks is supersonic with regard to the fast characteristic speed. Such reflected waves are not clearly visible in Fig. 4.8. Fig. 4.7 shows that the linear model reproduces the flow field around the interface from the SDL simulation with approximately the same accuracy as for the IDL simulation.

Profiles of $u = u'$ and w in the reference frame of the interface from the linear model and the NL simulation of the baseline case are shown in Fig. 4.9 for $t/t^* = 4$. As the full z-velocity is plotted, the transmitted and reflected fast shocks are visible in the profile from the NL simulation. By comparing Fig. 4.9 with Fig. 4.5 and Fig. 4.7, it can be seen that the flow around Alfvén fronts from the linear model does not predict the flow in that region from the NL simulation as accurately as it did for the linearized simulations. This is most likely because in the NL simulation the discontinuities downstream of the fast shocks are not Alfvén fronts, but include non-linear discontinuous waves. It will be shown in Chapter 5 that the inner-most discontinuous waves produced by the shock refraction process at the interface may

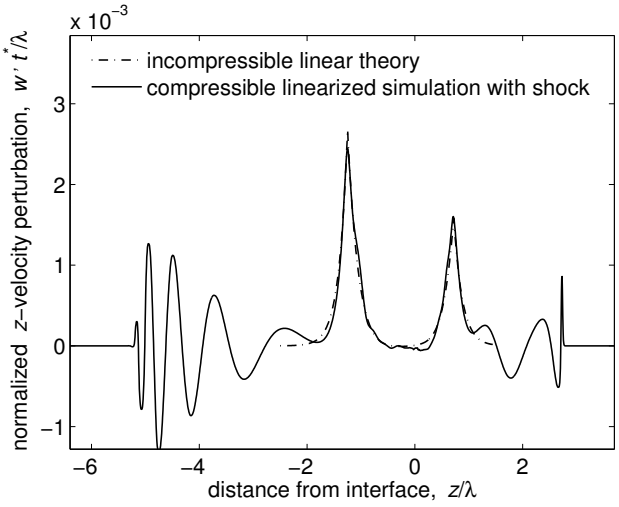

(a)

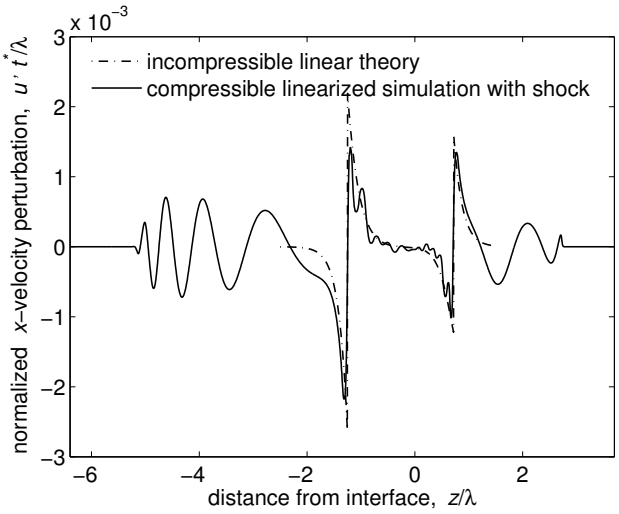

(b)

Figure 4.7: Profiles of (a) w' at $x = 0$ and (b) u' at $x = \lambda/4$ at $t/t^* = 4$ from the linear model and the SDL simulation of a shock accelerated interface with $M = 1.1$, $\beta = 16$, $\rho_2/\rho_1 = 3$, $\eta_0/\lambda = 0.01$ and $\gamma = 5/3$.

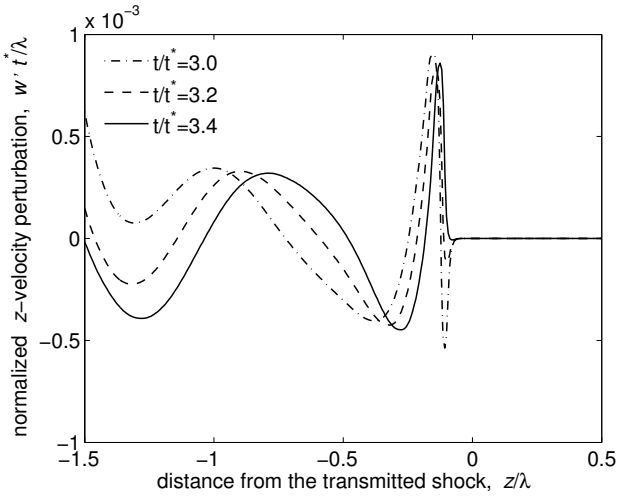

Figure 4.8: Profiles of w' at $x = 0$ in the reference frame of the transmitted base flow shock at $t/t^* = 4$ from the SDL simulation of a shock accelerated interface with $M = 1.1$, $\beta = 16$, $\rho_2/\rho_1 = 3$, $\eta_0/\lambda = 0.01$ and $\gamma = 5/3$.

be slow or intermediate shocks, 180^0 rotational discontinuities, slow-mode expansion fans, compound waves, or combinations of these. The performance of linear model depends on how well the Alfvén fronts approximate the non-linear discontinuous waves that are present in the NL simulation. However, the type of waves present vary with position along the interface, as the shock refraction process varies with the incidence angle, and with time as they propagate outward and evolve, making difficult to assess the performance of the linear model in this fashion. For this reason we assess the performance of the linear model based on how well it predicts the overall evolution of the interface, as shown in Fig. 4.4

4.3.2 Effect of increased shock strength

In this section the effect of increasing the incident shock Mach number M on the performance of the linear model is examined. This is done by studying two additional cases with $M = 1.25$ and $M = 2$. The other parameters are the same as in the baseline case. The linearized simulations of these cases were run for $N_t = 4000$ time-steps on the same domain as for the baseline case. For the NL simulation of the $M = 1.25$ case, $L_x = \lambda/2$, $L_z = 13\lambda$, $z_{if} = 6.8\lambda$, $N_x = 128$, $N_z = 3328$, and $T_{sim}/t^* = 6.5$, while

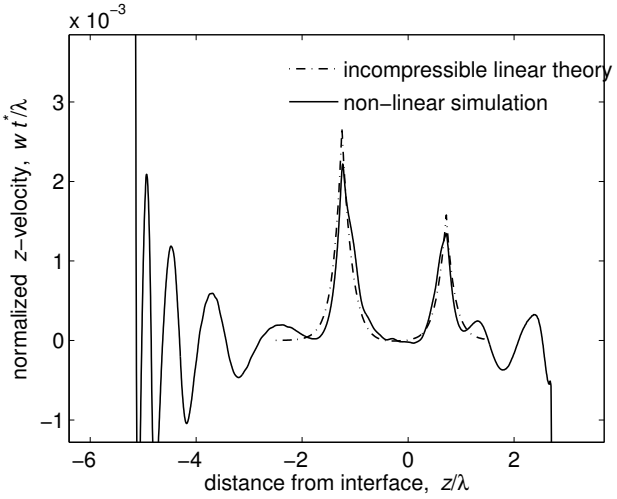

(a)

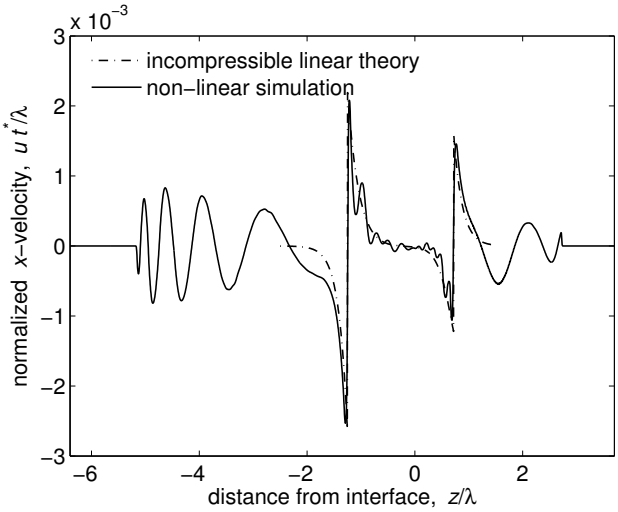

(b)

Figure 4.9: Profiles of (a) w in the reference frame of the interface at $x = 0$ and (b) u at $x = \lambda/4$ at $t/t^* = 4$ from the linear model and the NL simulation of a shock accelerated interface with $M = 1.1$, $\beta = 16$, $\rho_2/\rho_1 = 3$, $\eta_0/\lambda = 0.01$ and $\gamma = 5/3$.

M	Model	IDL Simulation	SDL Simulation	NL Simulation
		η_∞/λ		
1.1	0.0117237	0.0117465	0.0116413	0.0114644
1.25	0.0144258	0.0145142	0.0133635	0.0135617
2.0	0.0265009	0.0257331	0.0154361	0.0206051
		σt^*		
1.1	-1.38982	-1.28969	-1.42071	-1.31402
1.25	-1.248	-1.17046	-1.44987	-1.46507
2.0	-0.938511	-0.90709	-1.76315	-1.73981

Table 4.2: Interface perturbation parameters from the linear model and simulations corresponding to a shock accelerated interface with varying M and $\beta = 16$, $\rho_2/\rho_1 = 3$, $\eta_0/\lambda = 0.01$ and $\gamma = 5/3$.

for the $M = 2$ case, $L_x = \lambda/2$, $L_z = 20.5\lambda$, $z_{if} = 5.75\lambda$, $N_x = 128$, $N_z = 5248$, and $T_{sim}/t^* = 8.5$. Fig. 4.10 shows the η histories from the linear model and the three simulations for the $M = 1.1$, $M = 1.25$, and $M = 2$ cases. The values of η_∞ and σ computed from these are shown in Table 4.2.

From Fig. 4.10, it can be seen that the agreement between the η histories from linear model and the IDL simulation does not degrade as the magnitude of the impulse, ΔV, is increased with M. Thus the linear dependence of $\eta_\infty - \eta_0$ on ΔV predicted by the linear model also appears to hold in the compressible case. The η histories from the IDL and SDL simulations diverge as M increases, indicating that approximating the result of the shock interaction process as an impulsive acceleration becomes less accurate as the shock strength increases. The η histories from the SDL and NL simulations also diverge as M increases, indicating that non-linearities become more dominant as the shock strength increases. It is apparent from Fig. 4.10 that in the shock driven η histories, the amplitude of the long period oscillations, relative to $\eta_\infty - \eta_0$, increases with M. As discussed earlier, these oscillations appear to be due

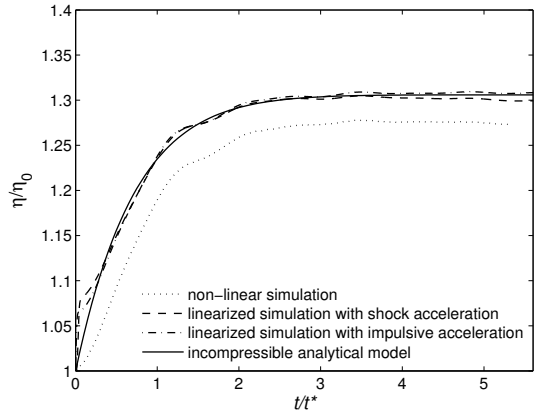

(a)

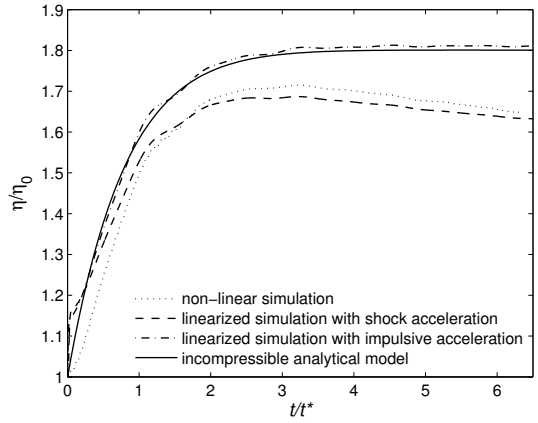

(b)

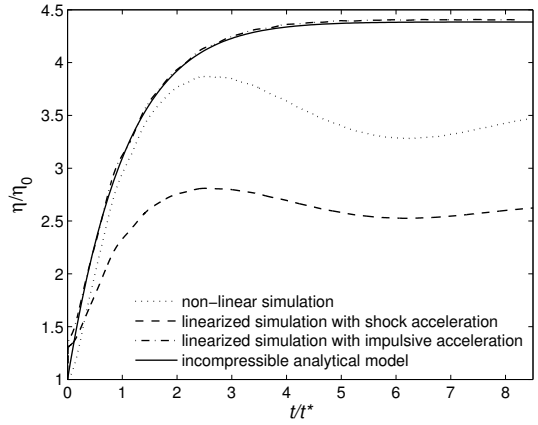

(c)

Figure 4.10: Interface amplitude histories from the incompressible linear model, IDL, SDL, and NL compressible simulations corresponding to a shock accelerated interface with $\beta = 16$, $\rho_2/\rho_1 = 3$, $\eta_0/\lambda = 0.01$, $\gamma = 5/3$ and (a) $M = 1.1$, (b) $M = 1.25$, or (c) $M = 2$.

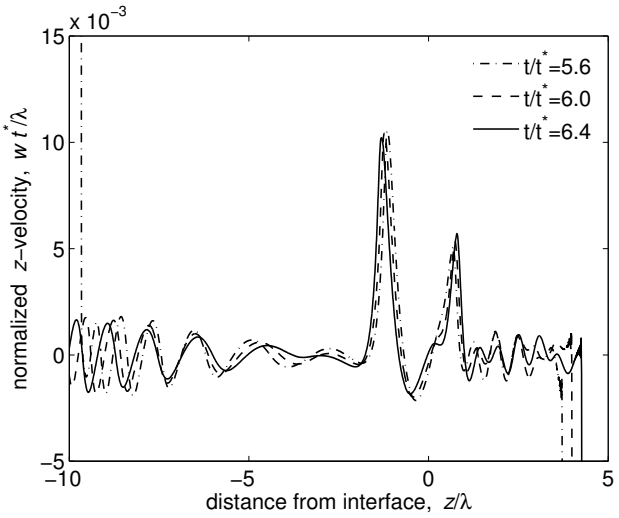

Figure 4.11: Profiles of w at $x = 0$ in the reference frame of the interface from the NL simulation of a shock accelerated interface with $M = 2$, $\beta = 16$, $\rho_2/\rho_1 = 3$, $\eta_0/\lambda = 0.01$ and $\gamma = 5/3$.

to disturbances caused by the interaction of transverse waves downstream of the reflected and transmitted shocks, and/or outgoing waves that have been reflected from the shocks. An example of such a disturbance crossing the interface can be seen in Fig. 4.11, which shows profiles of w from the $M = 2$ NL simulation at three different times. At $t/t^* = 6.4$, the disturbance appears as the small peak in w between the two large peaks that bracket the interface, which is located at $z = 0$. The disturbance approaches $z = 0$ from the right and increases the growth rate of the interface as it crosses it. This event corresponds to the change from negative to positive growth seen in the η history near $t/t^* \approx 6.2$. The increase in amplitude of the oscillations in η with M therefore indicates an increase in the effect of transverse and/or reflected waves, which is consistent with compressibility effects becoming more dominant.

Fig. 4.12 shows profiles of w in the reference frame of the interface from the linear model and the NL simulations of the three different M cases. These show that as M is increased, the linear model is less able to accurately represent the primary features of the flow, resulting in the increasing disagreement between the interface statistics from the model and the shock driven simulations seen in Table 4.2. For $M = 1.25$, the linear model over-predicts η_∞ from the IDL, SNL, and NL

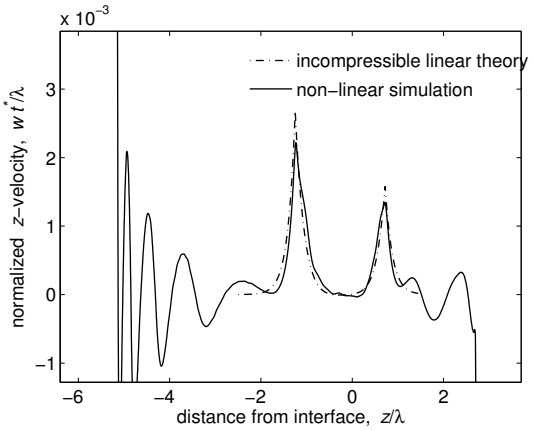

(a)

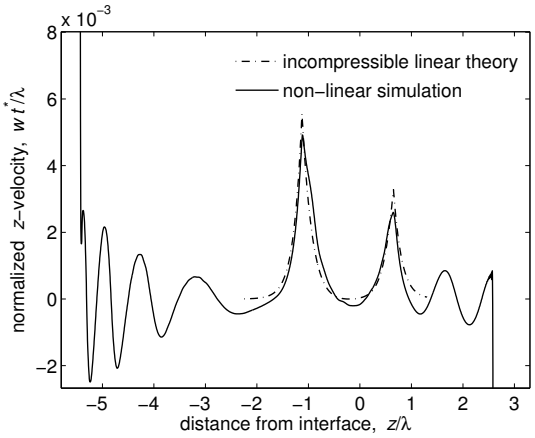

(b)

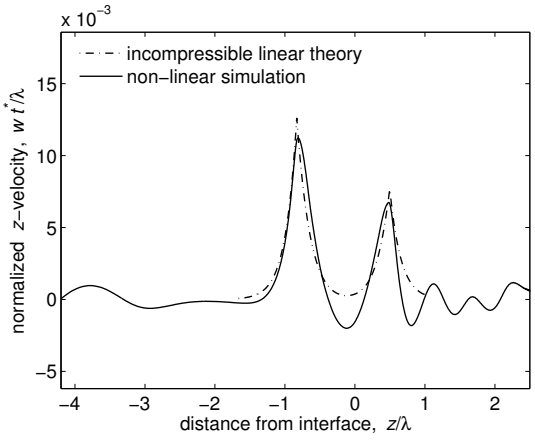

(c)

Figure 4.12: Profiles of w at $x = 0$ in the reference frame of the interface at $t/t^* = 4$ from the linear model and NL simulations corresponding to shock accelerated interfaces with $\beta = 16$, $\rho_2/\rho_1 = 3$, $\eta_0/\lambda = 0.01$, $\gamma = 5/3$ and (a) $M = 1.1$, (b) $M = 1.25$, or (c) $M = 2$.

simulations by -0.61%, 0.74%, and 0.60%, respectively, while σ is underestimated by -6.2%, 16.2%, and 17.4%, respectively. For $M = 2$, the linear model over predicts η_∞ from the IDL, SNL, and NL simulations by -0.55%, 39.7%, and 19.5%, respectively, while σ is underestimated by -3.3%, 87.9%, and 85.4%, respectively.

4.3.3 Effect of increased magnetic field

In this section the effect of increasing the magnetic field magnitude B on the performance of the linear model is examined. This is done by studying two additional cases with $\beta = 4$ and $\beta = 1$. The other parameters are the same as in the baseline case. The linearized simulations of these cases were run for $N_t = 4000$ time-steps on the same domain as for the baseline case. For the NL simulation of the $\beta = 4$ case, $L_x = \lambda/2$, $L_z = 6\lambda$, $z_{if} = 3.53\lambda$, $N_x = 256$, $N_z = 3072$, and $T_{sim}/t^* = 3$. For the $\beta = 1$ case, $L_x = \lambda/2$, $L_z = 9.5\lambda$, $z_{if} = 5.59\lambda$, $N_x = 128$, $N_z = 2432$, and $T_{sim}/t^* = 4.8$. This simulation was run for longer than $2t_{99} \approx 1.4$ because the value of η_∞ was not apparent at that time. Fig. 4.13 shows the η histories from the linear model and the three simulations for the $\beta = 1$, $\beta = 4$, and $\beta = 16$ cases. The values of η_∞ and σ computed from these are shown in Table 4.3.

For $\beta = 4$, the agreement between the linear model and the linearized simulations remains reasonable, with η_∞ deviating from the predicted value by 0.56% and 0.40% in the IDL and SDL simulations, respectively. The deviations in σ are 14.5% and 17.9%, respectively. The differences between the linear model and the NL simulation increase more substantially, with η_∞ and σ deviating by 3.6% and 25.4% from their predicted values, respectively. As $\beta \equiv 2p_0/B^2 = 2(a/C_A)^2/\gamma$ is decreased further, the Alfvén speed C_A in the undisturbed flow approaches the acoustic sound speed a and they become equal at $\beta = 2/\gamma = 6/5$. Thus for the $\beta = 1$ case, in the undisturbed flow C_A is greater than a and is therefore the fast and intermediate characteristic speed, while a is the slow characteristic speed. This situation if different from all the cases examined so far, and has serious consequences for the performance of the linear model. Fig. 4.14 shows profiles of w or w', as appropriate, in the reference frame of

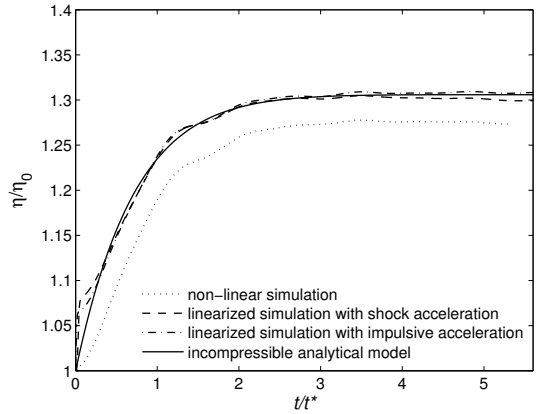

(a)

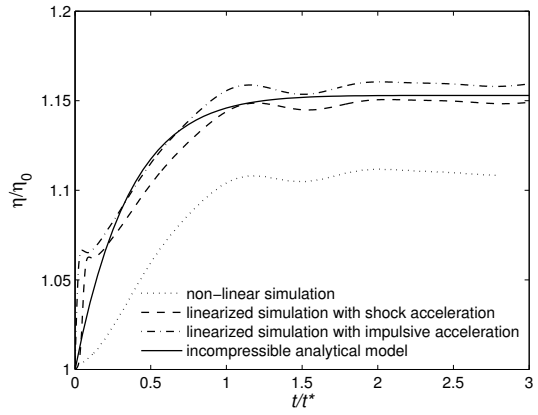

(b)

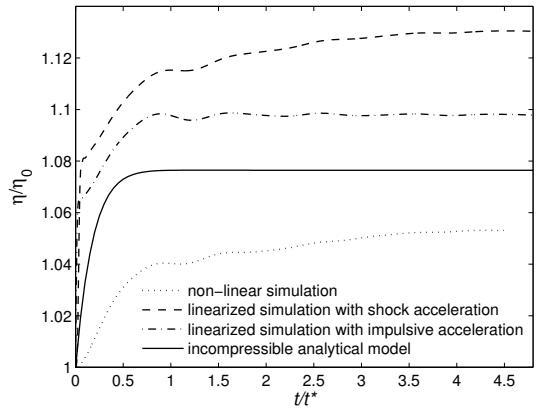

(c)

Figure 4.13: Interface amplitude histories from the incompressible linear model, IDL, SDL, and NL compressible simulations corresponding a shock accelerated interface with $M = 1.1$, $\rho_2/\rho_1 = 3$, $\eta_0/\lambda = 0.01$, $\gamma = 5/3$ and (a) $\beta = 16$, (b) $\beta = 4$, or (c) $\beta = 1$.

β	Model	IDL Simulation	SDL Simulation	NL Simulation
		η_∞/λ		
16	0.0117237	0.0117465	0.0116413	0.0114644
4	0.0103975	0.0104561	0.0103559	0.0100219
1	0.00975063	0.00994364	0.0102021	0.00949106
		σt^*		
16	-1.38982	-1.28969	-1.42071	-1.31402
4	-2.77963	-2.3755	-2.28134	-2.07366
1	-5.55927	-2.89482	-2.84995	-2.40185

Table 4.3: Interface perturbation parameters from the linear model and simulations corresponding to a shock accelerated interface with varying β and $M = 1.1$, $\rho_2/\rho_1 = 3$, $\eta_0/\lambda = 0.01$ and $\gamma = 5/3$.

the interface from the linear model and the three different simulations of the $\beta = 1$ case. The initial pressure in the IDL simulation is set to the post-shock interaction pressure, p_4, as stated in Section 4.2.3. At this pressure $\beta = 1.34143 > 6/5$, thus a is still slightly greater than C_A. They are close enough, however, that during the period when the interface is growing, information cannot propagate far enough upstream of the locations of the Alfvén fronts for a structure similar to that seen in the linear model to form upstream of the front locations. This in turn significantly alters the downstream flow, as is evident in Fig. 4.14(a). In the shock driven simulations, the propagation speed of the outermost shocks is approximately the same as that of the Alfvén fronts in the linear model. This results in constant interaction between the outermost shocks and the flow features that govern the overall evolution of the interface (which were reasonably well represented by the linear model in the other cases) rather than the separation that was present in the cases examined previously. In all three simulations, it can be seen from Fig. 4.14 that these factors cause the flow in the vicinity of the interface to deviate significantly from the linear model,

which results in the large differences in η histories shown in Fig. 4.13. Fitted values of η_∞ and σ from the $\beta = 1$ simulations are shown in Table 4.3, but in the shock driven cases the estimates are highly unreliable as η is still increasing at the end of the simulations. In summary, the performance of the linear model is reasonable for weak magnetic fields, but is compromised once the magnetic field becomes sufficiently strong that the Alfvén speed approaches the acoustic sound speed.

4.3.4 Effect of increased perturbation amplitude

In this section the effect of increasing the initial perturbation amplitude η_0 on the performance of the linear model is examined. This is done by studying two additional cases with $\eta_0/\lambda = 0.025$ and $\eta_0/\lambda = 0.1$. The other parameters are the same as in the baseline case. Additional linearized simulations are not required for these cases as η_0 is scaled out of the linear problem. η/η_0 histories for these cases are identical to the baseline case. For the NL simulations of the $\eta_0/\lambda = 0.025$ and $\eta_0/\lambda = 0.1$ cases, $L_x = \lambda/2$, $L_z = 20\lambda$, $z_{if} = 11.76\lambda$, $N_x = 64$, $N_z = 2560$, and $T_{sim}/t^* = 5.6$. Fig. 4.15 shows the η histories from the linear model and the three simulations for the $\eta_0/\lambda = 0.01$, $\eta_0/\lambda = 0.025$, and $\eta_0/\lambda = 0.1$ cases. The values of η_∞ and σ computed from these are shown in Table 4.4. From Fig. 4.15, it can be seen that the primary effect of increasing η_0 is to increase percent by which the impulsive linear model under-predicts the growth rate of the interface in the NL simulation. This effect has also been documented by Cook et al. (2004) for the hydrodynamic Rayleigh-Taylor instability. The increasing under-prediction of the growth rate by the linear model results in the over-prediction of the value of η_∞ observed in the NL simulation increasing from 2.2% to 2.9% to 3.4% as η_0/λ is increased from 0.01 to 0.025 to 0.1. The over-prediction of σ, however, does not increase monotonically; it changes from 7.8% to 5.5% then 13.4% as η_0 is increased. Overall, the performance of the model slowly degrades as the initial perturbation amplitude is increased, as is expected for a linear model. Comparing the results presented in this section to those in Section 4.3.2 and Section 4.3.3, it appears that the performance of the linear model

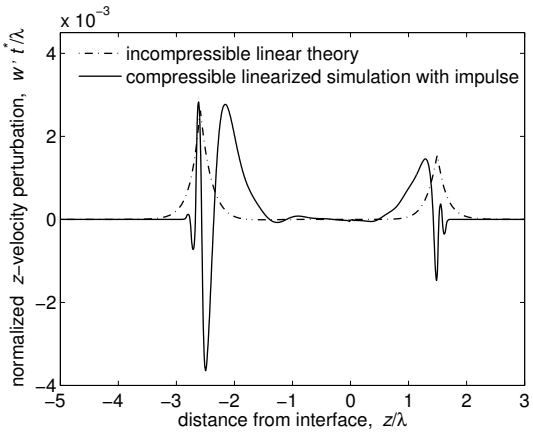

(a)

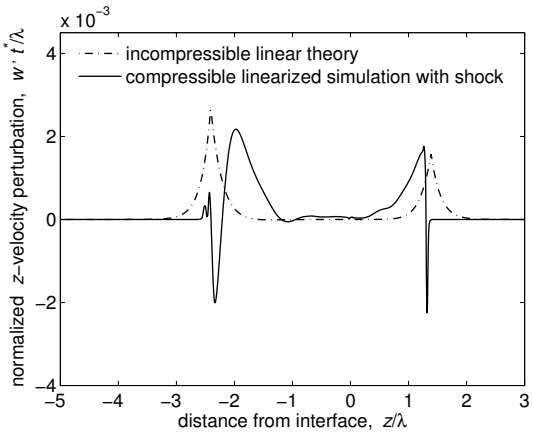

(b)

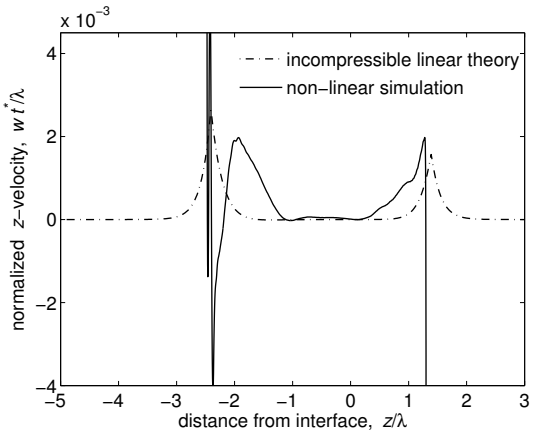

(c)

Figure 4.14: Profiles of w at $x = 0$ in the reference frame of the interface at $t/t^* = 2$ from the incompressible linear model and (a) IDL, (b) SNL, and (c) NL simulations corresponding to a shock accelerated interface with $M = 1.1$, $\rho_2/\rho_1 = 3$, $\eta_0/\lambda = 0.01$, $\gamma = 5/3$ and $\beta = 1$.

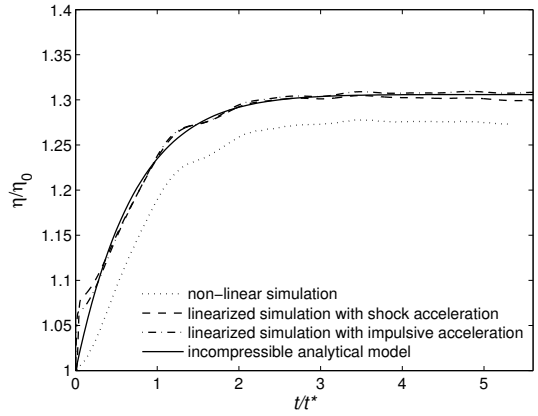

(a)

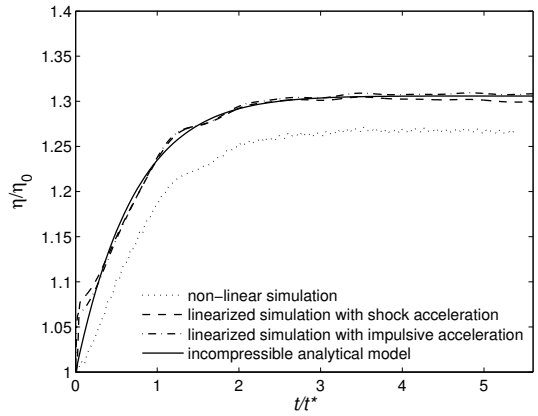

(b)

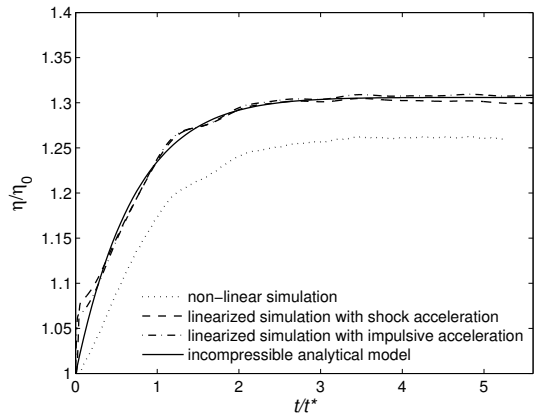

(c)

Figure 4.15: Interface amplitude histories from the incompressible linear model, IDL, SDL, and NL compressible simulations corresponding a shock accelerated interface with $M = 1.1$, $\beta = 16$, $\rho_2/\rho_1 = 3$, $\gamma = 5/3$ and (a) $\eta_0/\lambda = 0.01$, (b) $\eta_0/\lambda = 0.025$, or (c) $\eta_0/\lambda = 0.1$.

η_0/λ	Model	IDL Simulation	SDL Simulation	NL Simulation
			η_∞/λ	
0.01	0.0117237	0.0117465	0.0116413	0.0114644
0.025	0.0293214	0.0293784	0.0291154	0.0284653
0.1	0.119314	0.119546	0.118476	0.115273
			σt^*	
0.01	-1.38982	-1.28969	-1.42071	-1.31402
0.025	-1.38982	-1.28969	-1.42071	-1.31294
0.1	-1.38982	-1.28969	-1.42071	-1.20338

Table 4.4: Interface perturbation parameters from the linear model and simulations corresponding to a shock accelerated interface with varying η_0/λ and $M = 1.1$, $\beta = 16$, $\rho_2/\rho_1 = 3$ and $\gamma = 5/3$.

is less sensitive to increases in η_0 than it is to increases in either M or B; the of error in η_∞ increases by only 1.2% as η_0 is increased by an order of magnitude.

4.3.5 Chapter 2 case

In this section, the performance of the linear model is assessed for the case that was presented in Chapter 2; $M = 2$, $\beta = 1$, $\eta_0/\lambda = 0.1$, $\rho_2/\rho_1 = 3$, and $\gamma = 5/3$. This case represents what would appear to be the worst combination of the parameter values investigated in the previous three sections, from the perspective of model accuracy. The linearized simulations of this case were carried out in the domain $-20\lambda \leq z \leq 20\lambda$, which was discretized into $N_z = 6400$ control volumes. The simulations were run for $N_t = 8000$ time-steps with a CFL number of 0.5. These simulations were run for a longer duration that for the other cases in order to examine the long period oscillations for more than one cycle. For the NL simulation of this case, $L_x = \lambda/2$, $L_z = 12\lambda$, $z_{if} = 3.4\lambda$, $N_x = 128$, and $N_z = 3072$. The simulation was run for the duration $T_{sim}/t^* = 5$, which is approximately $5t_{99}$. Fig. 4.16 shows the η

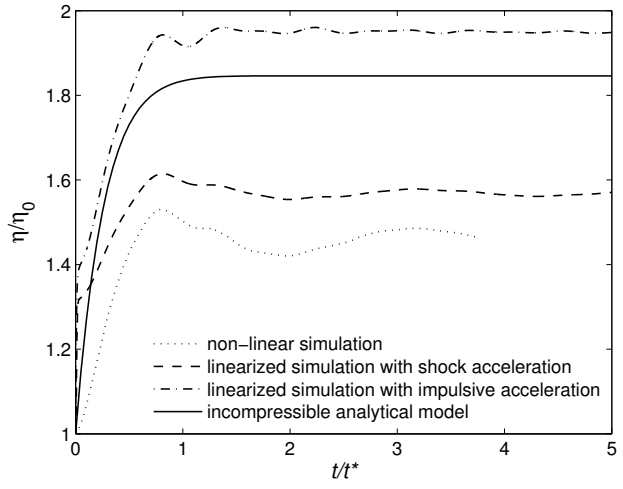

Figure 4.16: Interface amplitude histories from the linear model and simulations corresponding to a shock accelerated interface with $M = 12$, $\beta = 1$, $\rho_2/\rho_1 = 3$, $\eta_0/\lambda = 0.1$ and $\gamma = 5/3$.

	Model	IDL Simulation	SDL Simulation	NL Simulation
η_∞/λ	0.109167	0.11532	0.0928587	0.0868428
σt^*	-3.75405	-2.86994	-4.1807	-5.06429

Table 4.5: Interface perturbation parameters from the linear model and simulations corresponding to a shock accelerated interface with $M = 2$, $\beta = 1$, $\rho_2/\rho_1 = 3$, $\eta_0/\lambda = 0.1$ and $\gamma = 5/3$.

histories from the linear model and the three simulations for the current case. The values of η_∞ and σ computed from these are shown in Table 4.5.

Comparing Fig. 4.16 and Fig. 4.13(c), it appears that there is better agreement between the linear model and the simulations of the present case than for the $M = 1.1$, $\eta_0/\lambda = 0.01$, $\beta = 1$ case. This is confirmed by the smaller fractional deviations in σ from the predicted value in the simulations of the present case. The improved agreement is due to the higher incident shock Mach number in the present case. In the IDL simulation, this increases the initial pressure so that a is significantly greater than C_A, allowing information to propagate further upstream of the Alfvén front locations. In the shock driven simulations, stronger outermost transmitted and reflected shocks

are generated, which propagate significantly faster than the Alfvén fronts in the linear model, reducing the interaction that limited the accuracy of the linear model in the $M = 1.1$ case. This allows the linear model to better predict the flow in the vicinity of the interface, as can be seen by comparing Fig. 4.14 with Fig. 4.17, which shows profiles of w in the reference frame of the interface from the model and the three simulations. The results for this case indicate that for strong shocks, large initial perturbations, and strong magnetic fields, the linear model may still give a rough estimate of the interface behavior, but it is not quantitatively accurate.

4.4 Summary

To assess the performance of the incompressible linear model of the MHD RMI developed in Chapter 3, predictions from the model were compared to the results of impulse driven linearized (IDL), shock driven linearized (SDL), and non-linear (NL) compressible MHD simulations for a variety of cases. The performance of the linear model was first assessed for a baseline case with $M = 1.1$, $\eta_0/\lambda = 0.01$, $\beta = 16$, $\rho_2/\rho_1 = 3$, and $\gamma = 5/3$. For this case, the agreement between the linear model and the interface behavior from the IDL simulation is excellent, with the model predicting the final amplitude of the interface to within 0.2%. Compressible waves present in the simulation caused small amplitude, short period oscillations in the amplitude of the interface that are not present in the linear model. These waves do not effect the overall evolution of the interface as they have no vorticity associated with them. The agreement between the linear model and the SDL simulation is also excellent, while the final interface amplitude from the NL simulation is over-predicted by 2.2%. For all simulations of this case, the linear model represents the flow structures that dominate the evolution of the interface with reasonable accuracy. In the shock driven simulations, the interface amplitude also exhibits a long period oscillation caused by the interaction of transverse waves behind the shocks and/or outgoing waves reflected from the shocks. When the incident shock Mach number M is increased, the linear model still accurately predicts the behavior of the interface in the IDL simulation,

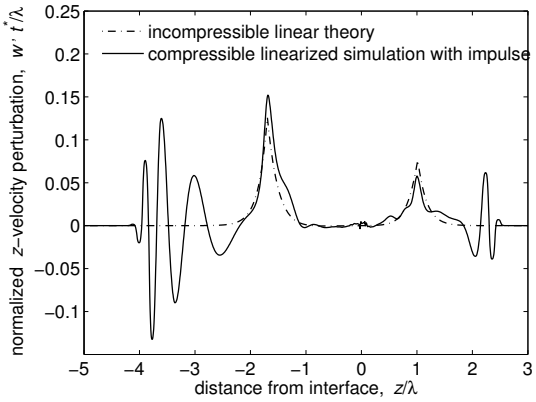

(a)

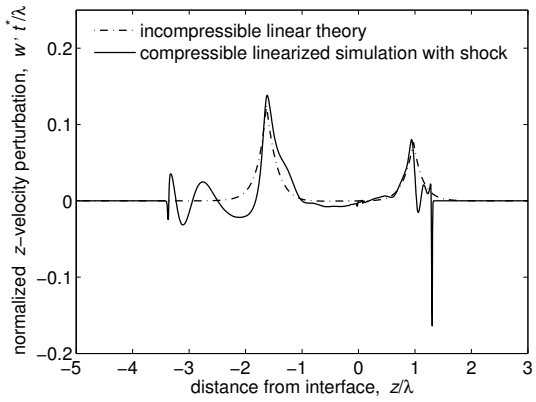

(b)

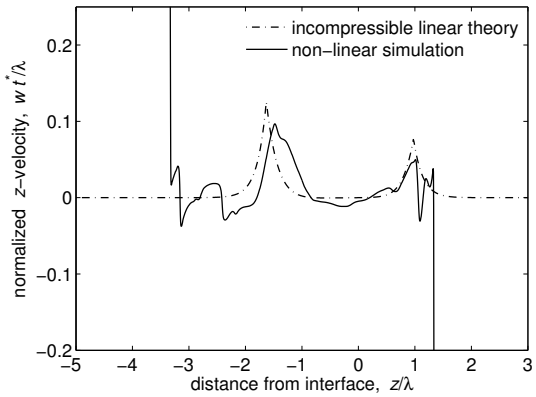

(c)

Figure 4.17: Profiles of w at $x = 0$ in the reference frame of the interface at $t/t^* = 2$ from the incompressible linear model and (a) IDL, (b) SDL, and (c) NL simulations corresponding to a shock accelerated interface with $M = 2$, $\rho_2/\rho_1 = 3$, $\eta_0/\lambda = 0.1$, $\gamma = 5/3$ and $\beta = 1$.

but it increasingly overestimates the amplitude of the interface η in the shock driven cases. The amplitude of the long period oscillations in the shock driven simulations increases with M. As the non-dimensional strength of the magnetic field β^{-1} is increased, the linear model less accurately predicts the results of all simulations. The accuracy of the linear model was found to be severely compromised once the magnetic field is sufficiently strong that the Alfvén wave speed approaches the acoustic sound speed, particularly if the incident shock is weak. When this occurs, the features of the flow that dominate the evolution of the interface deviate significantly from the linear model. One such case with $\beta = 1$ and $M = 1.1$ was investigated. When initial perturbation amplitude of the interface η_0 is increased, the agreement between the linear model and the linearized simulations is unchanged. The degree to which the linear model over-predicts η from NL simulations gradually increases with η_0. The performance of the linear model for all cases investigated, other than the case with $\beta = 1$ and $M = 1.1$ where reliable statistics could not be calculated, is summarized in Fig. 4.18. This shows the values of the final interface amplitude η_∞ and the time constant for the saturation of the interface σ that were calculated from the simulations plotted against the values predicted by the linear model. It can be seen that the linear model collapses the data from the simulations well. In conclusion, the interface behavior given by the incompressible linear model developed in Chapter 3 well approximates that seen in compressible linearized simulations when $M-1$, η_0/λ, and β^{-1} are small. For such cases, the agreement with interface behavior that occurs non-linear simulations is also reasonable. When $M-1$, η_0/λ, and β^{-1} are increased, the linear model becomes less accurate. For strong shocks, large initial perturbation amplitudes, and strong magnetic fields, the linear model may give a rough estimate of the interface behavior, but it is not quantitatively accurate.

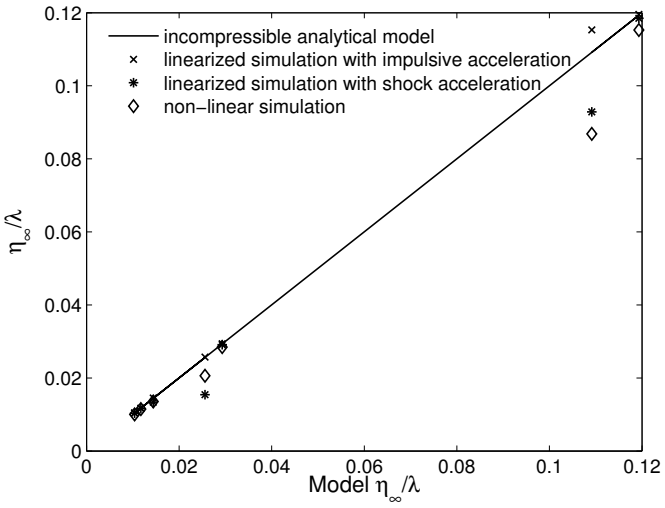

(a)

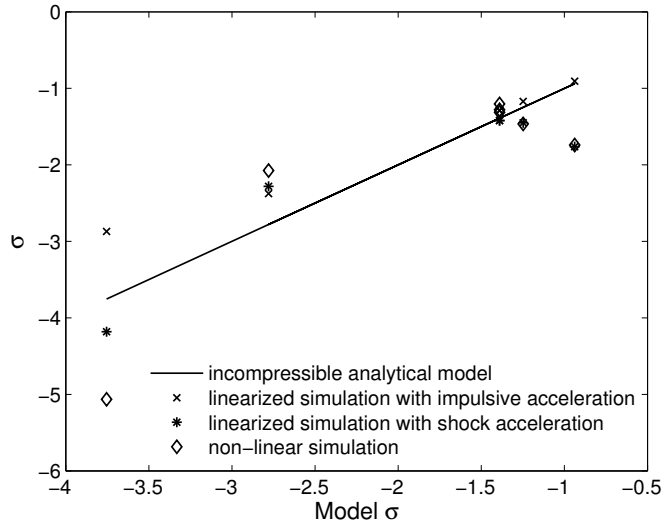

(b)

Figure 4.18: Interface perturbation parameters η_∞ and σ from all NL, SDL, and IDL simulations versus the values predicted by the incompressible linear model.

Chapter 5

Regular Shock Refraction at an Oblique Planar Density Interface in Magnetohydrodynamics

5.1 Introduction

As discussed in Chapter 1, Samtaney (2003) has demonstrated, via numerical simulations, that the growth of the Richtmyer-Meshkov instability is suppressed in the presence of a magnetic field. The particular flow studied was that of a shock interacting with an oblique planar contact discontinuity (CD) separating conducting fluids of different densities within the framework of strongly planar ideal magnetohydrodynamics (MHD). Here, we define a flow to be *planar* if there are no derivatives in the out of plane (z) direction, and *strongly planar* if there is also a reference frame in which there are no vector components in the z-direction. The physical setup for this shock interaction problem is depicted in Figure 5.1. The applied magnetic field is aligned with the motion of the incident shock. Other than the symmetry boundary conditions in the vertical direction, this is identical to the physical setup for the shock refraction problem that is investigated in this chapter. This flow is characterized by five dimensionless parameters: the incident shock *sonic* Mach number (M), the density ratio across the interface (η), the angle between the incident shock normal and the interface (α), the non-dimensional strength of the applied magnetic field

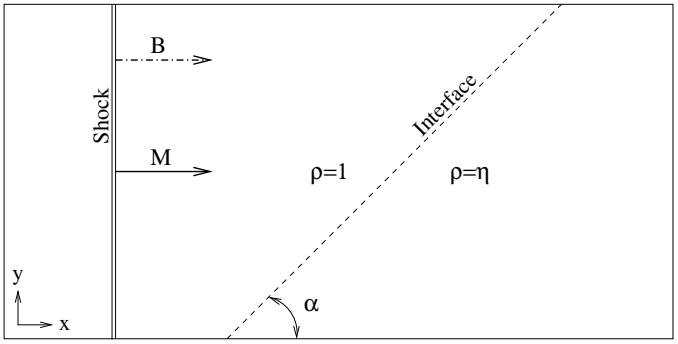

Figure 5.1: Physical setup for the Richtmyer-Meshkov simulations of Samtaney (2003) and the MHD shock refraction problem studied in this chapter. The initial pressure in the unshocked regions is $p_0 = 1$. In the simulations, symmetry boundary conditions are applied in the vertical direction.

($\beta^{-1} = B^2/2\mu_0 p_0$), and the ratio of specific heats γ. Here, the magnitude of the applied magnetic field (B) is made dimensionless against the square root of the product of the permeability (μ_0) and the pressure (p_0) of the gas. Samtaney presented detailed numerical results for cases with $M = 2$, $\eta = 3$, $\alpha = \pi/4$, $\beta^{-1} = 0$ (no magnetic field) or 0.5 (magnetic field present), and $\gamma = 1.4$.

In Chapter 1, it was stated the suppression of the RMI in MHD can be understood by examining how the shock refraction process at the interface changes with the application of a magnetic field. We will now consider this change in more detail, both to introduce necessary notation and clearly define the mathematical problem that is studied in this chapter. For the case with no applied magnetic field, $\beta^{-1} = 0$, the details of the shock refraction process are shown in Figure 5.2(a). The velocity vectors shown are in the reference frame where the point of intersection between the shocks and the interface is stationary. For Samtaney's choice of parameters, the incident shock (I) is transformed into a reflected shock (R) and a transmitted shock (T). This is the case for all sets of parameters considered here, although other wave configurations involving expansion fans are possible for other parameter sets. The angles of R and T to the flow are such that the flow angles and pressures (p) on either side of the interface are matched. The doubly shocked flow downstream of R has a lower velocity than the flow on the other side of the interface, which has been

decelerated only by T, resulting in a shear across the interface. Thus, in the absence of an applied magnetic field, the shock refraction process deposits vorticity on the interface, causing it to roll-up due to local Kelvin-Helmholtz instability.

In general, this wave configuration is not a valid solution of the equations of ideal MHD if a magnetic field is present. The reason for this is that a MHD CD cannot support a jump in either tangential velocity (u_t) or magnetic field (B_t) if the magnetic field has a component normal to the discontinuity (see e.g., Sutton and Sherman (1965)). Thus, there are four constraints that must be satisfied at the interface: continuous total pressure, flow angle, tangential velocity, and tangential magnetic field (the normal magnetic field must also be continuous, but this is not independent of the other constraints for this flow). There are only two degrees of freedom in the system, the angles of R and T, so that, in general, there is no solution. An exception occurs when the incident shock velocity and the applied magnetic field ($\mathbf{B}$) are aligned in the reference frame of the intersection point ($\mathbf{B}$ is parallel to the density interface). In this case, the MHD Rankine-Hugoniot relations ensure that the magnetic field and velocity vectors will be aligned in all regions of the flow, which allows jumps in u_t and B_t across the CD. Hence, there are two fewer constraints to be satisfied, admitting three-shock solutions to the aligned field shock interaction problem (Ogawa and Fujiwara, 1996). Such solutions have been studied in detail by Bestman (1975) and Ogawa and Fujiwara (1996).

In cases where the normal magnetic field (B_n) at the interface is non-zero, such as the problem under consideration here, a different system of waves must arise from the shock refraction process. From his numerical results, Samtaney (2003) observed that, in the presence of a magnetic field, R and T are replaced by fast magneto-sonic shocks, denoted RF and TF respectively. In addition, the vortex layer bifurcates into a structure that we will call the *inner layer*, which consists of two sub-fast magneto-sonic shocks, called RS and TS respectively, bracketing a MHD CD. This wave configuration is shown in Figure 5.2(b) and will henceforth be referred to as a *quintuple-point*. Note that the presence of shocks RS and TS provides the additional two degrees of freedom necessary to satisfy the two additional constraints at the

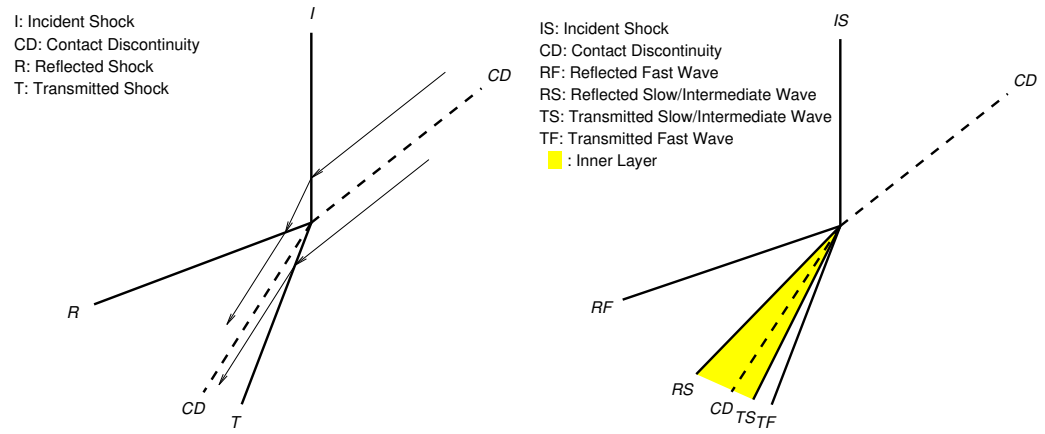

Figure 5.2: (a) Triple-point wave structure and streamlines resulting from a shock refraction process with $M = 2$, $\alpha = \pi/4$, and $\eta = 3$ in the absence of an applied magnetic field ($\beta^{-1} = 0$). (b) Quintuple-point wave structure resulting from a MHD shock refraction process with $M = 2$, $\alpha = \pi/4$, $\eta = 3$, and $\beta = 2$.

interface identified by Ogawa and Fujiwara (1996). It is well known that magnetosonic shocks support tangential velocity jumps (see e.g., Sutton and Sherman (1965)). This allows shocks RS and TS to eliminate the velocity discrepancy between the flow downstream of shock RF and that downstream of shock TF, leaving the MHD CD vorticity free. Thus, we see that the application of a magnetic field can suppress the Kelvin-Helmholtz instability because, in most cases, the shock refraction process does not deposit vorticity on the density interface.

In this chapter, we develop a solution technique for the MHD shock refraction problem, then use this to demonstrate that the quintuple-point and other similar structures are entropy-satisfying weak solutions of the equations of ideal MHD. In Section 5.2, we formulate the equations required to solve the problem. The solution technique is then outlined in Section 5.3. Section 5.4 contains a detailed account of the quintuple-point solution for Samtaney's set of parameters, along with a comparison to his numerical results. A second solution that is not realized in the numerical simulation is also described. As B is decreased, we find that the types of waves arising

from the shock refraction process undergo a number of transitions. These transitions in solution type are discussed in Section 5.5. How the solutions approach the hydrodynamic triple-point in the limit of vanishing applied magnetic field is addressed in Chapter 6. Finally, the work presented in this chapter is summarized in Section 5.6.

5.2 Formulation

5.2.1 The governing equations of ideal MHD

In this investigation, we will consider solutions to the equations of ideal MHD. These equations govern the motion of a quasi-neutral conducting fluid if viscosity, thermal conductivity, the Hall effect, and electrical resistivity are neglected (Sutton and Sherman, 1965). The steady state forms of these equations are

$$\nabla \cdot (\rho \mathbf{u}) = 0 \ , \tag{5.1}$$

$$\rho \left(\mathbf{u} \cdot \nabla \right) \mathbf{u} = -\nabla p + \frac{1}{\mu_0} \left(\nabla \times \mathbf{B} \right) \times \mathbf{B} \ , \tag{5.2}$$

$$\rho \left(\mathbf{u} \cdot \nabla \right) h_T = \frac{1}{\mu_0} \left(\nabla \times \mathbf{B} \right) \times \mathbf{B} \cdot \mathbf{u} \ , \tag{5.3}$$

$$\nabla \cdot \mathbf{B} = 0 \ , \tag{5.4}$$

$$\nabla \times (\mathbf{u} \times \mathbf{B}) = 0 \ . \tag{5.5}$$

Here, ρ is the density, p is the pressure, $\mathbf{u}$ is the velocity, $\mathbf{B}$ is the magnetic field, μ_0 is the magnetic permeability, and $h_T = h + 1/2 \left(\mathbf{u} \cdot \mathbf{u} \right)$, where h is the enthalpy. In addition, the plasma is assumed to be a perfect gas with constant specific heats C_p and C_v. In this case

$$p = \rho R T \ ,$$

$$h = C_p T \ ,$$

$$h_T = \frac{\gamma}{\gamma - 1} \frac{p}{\rho} + \frac{1}{2} \mathbf{u} \cdot \mathbf{u} \ ,$$

where T is temperature, $R = C_p - C_v$, and $\gamma = C_p/C_v$. Note that in this system of equations, $\mathbf{B}$ has different units than in the earlier chapters, where it was normalized by $\sqrt{\mu_0}$ to make the equations more compact. In the sequel, we consider discontinuous solutions to these equations, solutions for expansion fans, solutions for compound waves, and matching conditions at contact discontinuities. These are then combined to construct multiple-wave solutions corresponding to the interaction of a shock with an oblique density discontinuity.

5.2.2 The MHD Rankine-Hugoniot relations

The MHD Rankine-Hugoniot (RH) relations govern weak solutions to the equations of ideal MHD corresponding to discontinuous changes from one state to another. It is assumed that all dependent variables vary only in the direction normal to the shock front, which is denoted with the subscript n. Under this assumption, Eq. 5.4 implies that B_n is continuous across the shock. We also assume that all velocities and magnetic fields are coplanar, as we are seeking strongly planar ideal solutions. Under these assumptions, the set of jump relations for a stationary discontinuity separating two uniform states are (see e.g., Sutton and Sherman (1965)),

$$[\rho u_n] = 0 \ , \tag{5.6}$$

$$\left[\rho u_n^2 + p + \frac{B_t^2}{2\mu_0}\right] = 0 \ , \tag{5.7}$$

$$\left[\rho u_n u_t - \frac{1}{\mu_0} B_n B_t\right] = 0 \ , \tag{5.8}$$

$$\left[\frac{\rho u_n}{2}\left(u_n^2 + u_t^2\right) + \frac{\gamma u_n p}{\gamma - 1} + \frac{1}{\mu_0} u_n B_t^2 - \frac{1}{\mu_0} u_t B_n B_t\right] = 0 \ , \tag{5.9}$$

$$[u_n B_t - u_t B_n] = 0 \ . \tag{5.10}$$

Here, the subscript t denotes the component of a vector tangential to the shock, and $[A] \equiv A_2 - A_1$ denotes the difference in the quantity A between the states upstream (subscript 1) and downstream (subscript 2) of the shock.

We utilize the method of Kennel et al. (1989) for obtaining solutions to the copla-

nar RH relations for propagating discontinuities ($u_{n1} \neq 0$). First, the following convenient set of normalized variables is introduced:

$$r = \frac{u_{n2}}{u_{n1}} \ , \quad b = \frac{B_{t2}}{B_1} \ , \quad U_t = \frac{u_{t2}}{u_{n1}} \ , \quad \sin\theta_1 = \frac{B_{t1}}{B_1} \ ,$$

where θ_1 is the angle between the upstream magnetic field and the shock normal. Also, reference upstream Alfvén, intermediate, and sonic Mach numbers are defined as

$$M_{A1}^2 = \frac{u_{n1}^2}{C_{A1}^2} = \frac{\mu_0 \rho_1 u_{n1}^2}{B_1^2} \ , \quad M_{I1}^2 = \frac{u_{n1}^2}{C_{I1}^2} = \frac{M_{A1}^2}{\cos(\theta_1)^2} = \frac{\mu_0 \rho_1 u_{n1}^2}{B_n^2} \ , \quad M_{S1}^2 = \frac{u_{n1}^2}{C_{S1}^2} = \frac{\rho_1 u_{n1}^2}{\gamma p_1} \ .$$

It can then be shown that Eqs. 5.6-5.9 reduce to the following algebraic equation in r and b obtained by Liberman and Velikhovich (1986):

$$F(r,b) = Ar^2 + B(b)r + C(b) = 0 \ ,$$

where A, B, and C are defined in Eq. C.3 in Appendix C. The relation $F(r,b) = 0$ defines a curve in (r,b) space on which the fluxes of mass, momentum, and energy are equal to those upstream of the shock. The final jump condition can be expressed as

$$Z(r,b) = bX - Y\sin\theta_1 = 0 \ ,$$

where X and Y are defined in Eqs. C.3 and C.5 in Appendix C. The intersections of the curves defined by $F = 0$ and $Z = 0$ are the locations in (r,b) space where all jump conditions are satisfied. The two equations, $F = 0$ and $Z = 0$, can be combined into a quartic equation in r, which we know has at least one real solution ($r = 1$). Thus the quartic must have either two or four real solutions, implying that there are either two or four intersections between the two curves. We refer to the three non-unity solutions of the quartic as roots A, B, and C. Expressions for these roots are included in Appendix C. Figure 5.3 shows the curves $F = 0$ and $Z = 0$ for a choice of parameters where there are four intersections, labeled

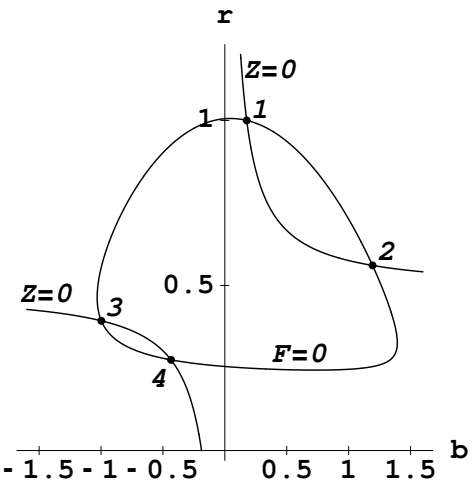

Figure 5.3: Graphical solution to the MHD Rankine-Hugoniot relations for $\sin^2\theta_1 = \frac{1}{32}$, $M_{A1}^2 = 2$, $M_{S1} \to \infty$, and $\gamma = \frac{5}{3}$ (choice of parameters from Kennel et al. (1989))

1-4 in order of decreasing r. The velocities at each of these points bear a definite relationship to the fast (C_F), intermediate (C_I), and slow (C_{SL}) MHD characteristic speeds: $u_n(1) \geq C_F \geq C_I \geq C_{SL}$, $C_F \geq u_n(2) \geq C_I \geq C_{SL}$, $C_F \geq C_I \geq u_n(3) \geq C_{SL}$, and $C_F \geq C_I \geq C_{SL} \geq u_n(4)$. The entropies of the four states are ordered $S(1) \leq S(2) \leq S(3) \leq S(4)$, indicating that only six of the transitions between these states coincide with entropy-increasing shocks. Of these, transitions $1 \to 2$ are fast shocks, $3 \to 4$ are slow shocks, while $1 \to 3$, $1 \to 4$, $2 \to 3$, and $2 \to 4$ are intermediate shocks. Further details of how we solve the MHD RH relations for the flow state downstream of a shock are contained in Appendix C.

5.2.3 Admissibility of MHD discontinuities

To this point, we have discussed weak solutions to the ideal MHD equations. We now discuss their admissibility. This topic is an active research field and open questions remain. In the three-dimensional MHD system of equations, the evolutionary condition (see e.g. Akhiezer et al. (1959); Polovin and Demutskii (1990); Jeffrey and Taniuti (1964)) restricts physically admissible discontinuities to fast shocks, slow shocks, contact discontinuities, and rotational discontinuities (RDs). In a series of numerical experiments Wu (1987, 1990, 1995), however, identified intermediate shocks

within numerical solutions to the full (here, full implies non-zero dissipation) MHD equations, which was interpreted as a failure of the evolutionary condition by Myong and Roe (1997) amongst others. Subsequently, Myong and Roe (1997) applied their viscosity admissibility condition to show that in the strongly planar system $1 \rightarrow 3$, $1 \rightarrow 4$, and $2 \rightarrow 4$ intermediate shocks are physical, while $2 \rightarrow 3$ intermediate shocks are not. They also found that 180^o RDs, which are a special case of $2 \rightarrow 3$ intermediate shocks, have no role in strongly planar problems. These results are in agreement with many numerical simulations by Wu (1987, 1990, 1995). In the full three-dimensional system, Wu (1990, 1995) observes $2 \rightarrow 3$ intermediate shocks to be possible, along with the other shock types, while RDs are regarded as unphysical. Wu (1990) also finds that the particular choice of dissipation coefficients can effect the admissibility of MHD shocks in the full system; see Wu (1990) and cited references therein for details.

Falle and Komissarov (2001) (hereafter referred to as FK) argue that the viscosity admissibility condition and the evolutionary condition are complementary; a shock is physical only if it satisfies both. Hence, the subsets of discontinuities admissible in planar and strongly planar flows are not identical because only the former admit Alfvén waves. In this framework, $1 \rightarrow 3$ and $2 \rightarrow 4$ intermediate shocks along with slow (C_1) and fast (C_2) compound waves (using the notation in Myong and Roe (1997)) are shown to be evolutionary (satisfy the evolutionary condition) and have unique dissipative structures in the strongly planar case. Both $2 \rightarrow 3$ intermediate shocks and 180^o RDs are found to be non-evolutionary in the strongly planar system. These results are in agreement with those of Myong and Roe (1997). This is not the case for $1 \rightarrow 4$ intermediate shocks as these are shown to be non-evolutionary and hence inadmissible, although they do have a non-unique steady dissipative structure in the strongly planar case.

For the full three-dimensional MHD system, of which the planar (u_z, B_z may be non-zero) system is a subset, FK reiterate the following results: fast and slow shocks are evolutionary and have unique structurally stable dissipative structures, while all intermediate shocks are non-evolutionary and can be destroyed by interactions with

Alfvén waves. Thus, in contrast to Wu (1987, 1990, 1995), FK argue that intermediate shocks are always inadmissible in the three-dimensional system. FK also state that, in the three-dimensional system, $1 \rightarrow 3$, $1 \rightarrow 4$, and $2 \rightarrow 4$ intermediate shocks possess non-unique steady dissipative structures, while $2 \rightarrow 3$ intermediate shocks possess a unique steady dissipative structure. CDs and RDs are found to be evolutionary but do not possess a steady dissipative structure as they are linear and hence have no non-linear steepening to balance spreading due to dissipation. They nevertheless consider RDs to be admissible in the three-dimensional system, in contrast to Wu (1990, 1995). FK also analyze the admissibility of discontinuities that travel at the same speed as certain characteristics, such as switch-on and switch-off shocks.

To interpret our results, we have adopted the framework of FK because of its completeness, but we acknowledge that the physical relevance of intermediate shocks and RDs is not yet completely clarified. Following Torrilhon (2003a), we divide our solutions to the ideal MHD system into two categories: regular (r) and irregular (c) solutions. r-solutions include only fast and slow waves (shocks or expansion fans), RDs, and CDs. According to FK, all discontinuities in $r-$solutions are evolutionary in the planar system. Here, c-solutions are those that include discontinuities that are non-evolutionary in the planar system but are evolutionary in the strongly planar system according to FK.

5.2.4 Governing equations for MHD expansion fans and slow compound waves

The basic equations governing the flow through a centered, steady MHD expansion fan can be obtained by writing Eqs. 5.1-5.2 and Eqs. 5.4-5.5 in cylindrical co-ordinates, then assuming variations only occur with the polar angle φ (Yang and Sonnerup, 1976, Krisko and Hill, 1991). Further, the flow is assumed to be isentropic; hence, the energy equation is replaced by an entropy equation. These equations can then be manipulated into a system of non-linear coupled ODEs for a set of non-dimensional variables within the expansion fan. The system of ODEs and an outline of their

derivation is contained in Appendix D. In the equations, the magnetic field is represented by the non-dimensional vector

$$\mathbf{K} \equiv \frac{\mathbf{B}}{\sqrt{2\mu_0 p}} \ .$$

Note that $K \equiv |\mathbf{K}| = \beta^{-1/2}$, $K_n = K\cos\theta$, and $K_t = K\sin\theta$, so $\mathbf{K}$ can be used interchangeably with $(\beta,\ \theta)$. Appendix D also includes the relation required to determine the location of the leading wavelet of an expansion fan. The complete solution throughout an expansion fan can be found by numerically integrating the system of ODEs with respect to φ from the leading wavelet.

In the strongly planar system, Myong and Roe (1997) recommend the use of compound waves as a substitute for $2 \rightarrow 3$ intermediate shocks, which are inadmissible under their viscosity admissibility condition and the evolutionary condition. Compound waves are discussed in more detail in Appendix E. The compound wave relevant to this study consists of a $2 \rightarrow 3 = 4$ intermediate shock, for which $u_{n2} = C_{SL2}$, followed immediately downstream by a slow-mode expansion fan. This is the steady two-dimensional analogue of the unsteady one-dimensional slow compound wave referred to as C_1 by Myong and Roe (1997). We will use the same designation for the two-dimensional compound wave. A relation for determining the location of a $2 \rightarrow 3 = 4$ intermediate shock is included in Appendix E, along with a procedure for determining the flow state downstream of a C_1 compound wave.

5.2.5 Matching conditions at the contact discontinuity

For the proposed wave configuration to be a valid solution of the equations of ideal MHD, the following matching conditions must hold across the shocked contact (SC):

$$p_3 = p_5 \ , \tag{5.11}$$

$$u_{3x} = u_{5x} \ , \tag{5.12}$$

$$u_{3y} = u_{5y} \ , \tag{5.13}$$

$$|\mathbf{K}_3| = |\mathbf{K}_5| \ , \tag{5.14}$$

$$\mathbf{K}_3/|\mathbf{K}_3| = \mathbf{K}_5/|\mathbf{K}_5| \ . \tag{5.15}$$

Here, states 3 and 5 are the conditions to the left and right of the SC, respectively. This is indicated in Figure 5.4, which shows how the various angles and regions of uniform flow in a solution are defined. In Appendix F, we outline our procedure for determining the conditions on either side of the SC from the problem parameters and guessed values of the unknown wave angles.

5.3 Solution technique

We seek solutions to the strongly planar ideal MHD equations. In the equivalent dissipative solutions, the out of plane components of **B** and **u** may be non-zero within the internal structures of certain waves. This implies that some of our solutions are planar, not strongly planar, in the presence of dissipation. For a given set of problem parameters, (M, β, η, α, γ), a solution to the MHD shock refraction problem is obtained by first postulating a wave configuration. We restrict our attention to wave configurations in which the number of unknown wave angles equals the number of independent matching conditions at the SC (four). Families of solutions may be possible if additional waves are introduced, for example, by replacing a $2 \rightarrow 4$ intermediate shock or a C_1 compound wave by a $2 \rightarrow 3$ intermediate shock followed by a slow wave (shock or expansion fan). Wu (1995) found this for certain coplanar MHD

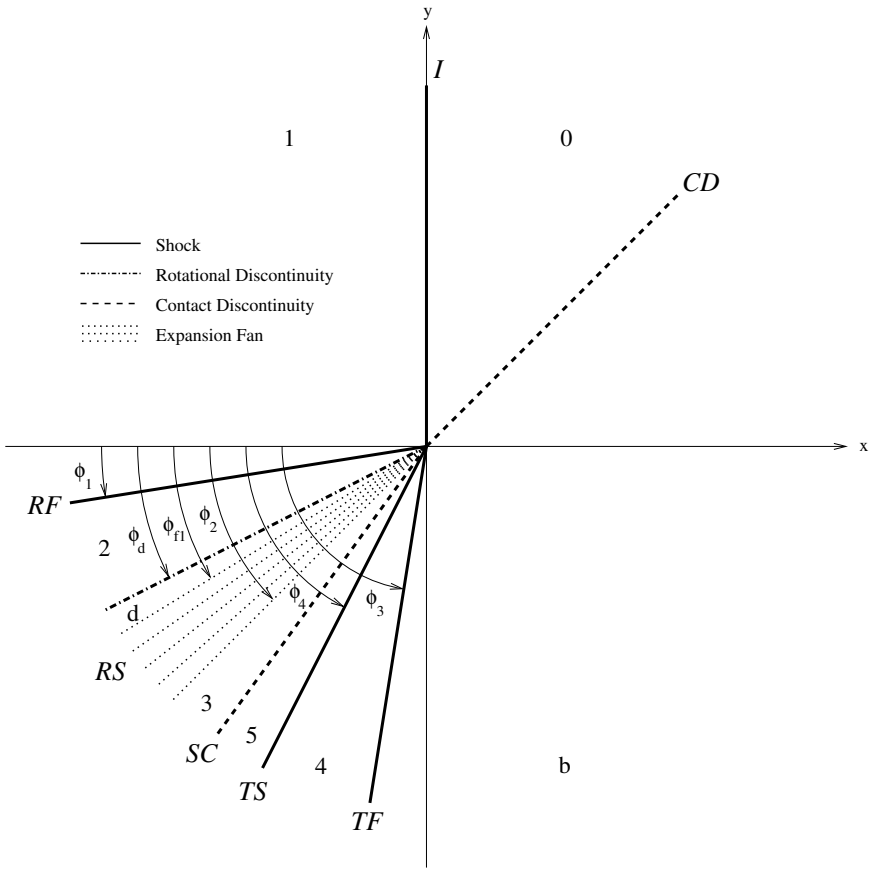

Figure 5.4: Designations of the angles and regions of uniform flow for a shock refraction problem where the RS wave-group consists of a RD followed by a slow-mode expansion fan, and the TS wave is a shock. This type of solution is referred to as a *sextuple-point*. The undisturbed conditions to the left and right of the CD are denoted states 0 and b, respectively.

Riemann problems, which are analogous to the flows considered here. We remark that the families of solutions identified by Wu (1995) appear to always include $2 \rightarrow 3$ intermediate shocks; we have not considered structures involving this shock type in depth as they are inadmissible according to FK. For the range of parameters under consideration here, for which RF and TF are always fast shocks, a wave configuration is postulated by specifying whether the RS and/or the TS wave-group consists of a shock, a C_1 compound wave, a RD, a RD followed by a slow shock, or a RD followed by a slow-mode expansion fan. Next, the types of all shocks in the system must be specified by selecting which root of Eq. C.6 is used to compute r for each shock. Once the wave configuration has been specified in this manner, guesses are made for each of the four unknown angles in the system: ϕ_1, ϕ_2, ϕ_3, and ϕ_4. As indicated in Figure 5.4, ϕ_1 specifies the location of shock RF, ϕ_2 specifies either the location of shock RS or the last expansion fan wavelet in wave-group RS, ϕ_3 specifies the location of shock TF, and finally, ϕ_4 specifies either the location of shock TS or the last expansion fan wavelet in wave-group TS, depending on the wave configuration postulated. The procedure outlined in Appendix F is then used to compute the conditions on either side of the SC for the guessed wave angles. An approximate solution to the MHD shock refraction problem is then obtained by iterating on the wave angles using a secant method until matching conditions Eqs. 5.11-5.14 are satisfied to six significant figures. To check the consistency of this procedure, the wave angles obtained from the iterative process are then substituted into matching condition Eq. 5.15 to ensure that it is also satisfied.

5.4 A detailed local solution; case S1

In subsequent sections, we will explore several branches corresponding to the solution of Eqs. 5.11-5.14 in the parameter space of M, η, α, β, and γ. For the purposes of discussion, we define a branch to be a set of solutions along a line in parameter space that all satisfy the same admissibility condition. The lines in parameter space considered here have fixed M, η, α, and γ with β in the range $\beta_{min} \leq \beta \leq \beta_{max}$. We

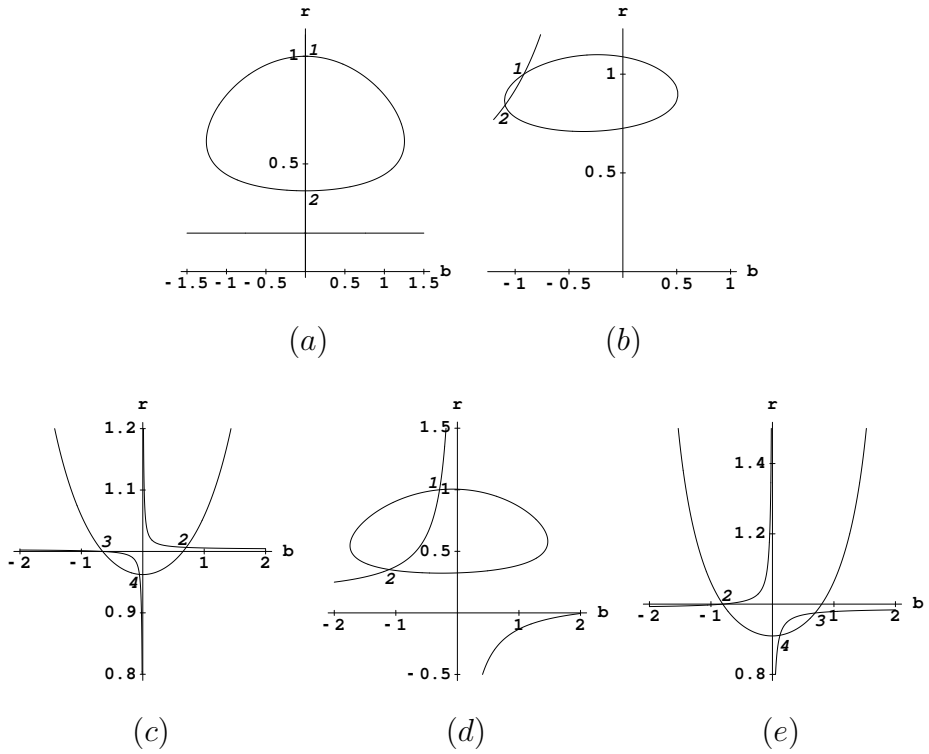

Figure 5.5: Graphical solutions of the MHD Rankine-Hugoniot relations for conditions upstream of (a) shock I, (b) shock RF, (c) shock RS, (d) shock TF, (e) shock TS in case S1.

will study in detail solutions along four such lines that we denote as Lines I-IV. The parameters defining these are summarized in Table 5.1. To illustrate the application of our solution technique for a particular case, we choose Line I ($M = 2$, $\eta = 3$, $\alpha = \pi/4$, and $\gamma = 1.4$) with $\beta = \beta_{min} = 2$. This parameter set corresponds to that used by Samtaney (2003). In the following discussion, for convenience, we denote this as case S1.

5.4.1 Irregular solution

First, we examine the solution suggested by Samtaney's numerical results, in which four shocks arise from the shock refraction process for case S1. We demonstrate that this is a c-solution. Including the incident shock, there are five shocks in the system, hence the solution is referred to as a quintuple-point. The incident shock is

hydrodynamic and has no effect on the magnetic field, as can be seen from Figure 5.5(a), which shows the graphical solution of the RH relations for the conditions upstream of this shock. The value of r for this shock is given by root A of the RH relations. In this instance root A is the only real root, disregarding $r = 1$, and gives $r_0 = 0.375$ while $b_0 = 0$. Note that hydrodynamic shocks are non-evolutionary if the upstream u_n is super-Alfvénic and the downstream u_n is sub-Alfvénic in the reference frame of the shock. This criteria is not met for case S1 so the incident shock is evolutionary, as is the case for all other sets of parameters considered here. With reference to Figure 5.4, RF was found to lie at $\phi_1 = 0.405693$ and is a fast shock. Root A gives $r_1 = 0.844$ resulting in $b_1 = -1.09$. Figure 5.5(b) shows that this is the only real root other than 1. RS is a slow shock and was found to lie at $\phi_2 = 0.917018$. Figure 5.5(c) shows that all three roots are real for RS, but as intersection 3 corresponds to the upstream state, only a transition to intersection 4 will result in $r_2 < 1$ and thus satisfy the entropy condition. This transition corresponds to a slow shock for which root B gives the value of r. r_2 and b_2 were found to be 0.963 and -0.0547, respectively. TF was found to lie at $\phi_3 = 1.27673$ and is a fast shock for which root A gives $r_b = 0.352$, while $b_b = -1.11$. Finally, TS is a $2 \rightarrow 4$ intermediate shock and was found to lie at $\phi_4 = 1.19426$. The presence of this intermediate shock implies that this quintuple-point is a c-solution, which we denote solution S1c. Figure 5.5(e) shows that all three roots are real for TS and intersection 2 corresponds to the upstream state. A transition to intersection 1, corresponding to root A, would violate the entropy condition. A transition to intersection 3, corresponding to root C, satisfies the entropy condition but it was found that, for case S1, the matching conditions Eqs. 5.11-5.15 could not be satisfied if TS was assumed to be a $2 \rightarrow 3$ intermediate shock. Thus, r_4 is given by root B and was found to be 0.911 while $b_4 = 0.122$.

The shock and CD angles from solution S1c are overlaid on the numerical results of Samtaney (2003) in Figures 5.6(a) and (b). Figure 5.6(a) shows contours of density which clearly display the location of the CD. Streamlines are also plotted in this figure to show how the various shocks in the system deflect the flow. In region 2, the

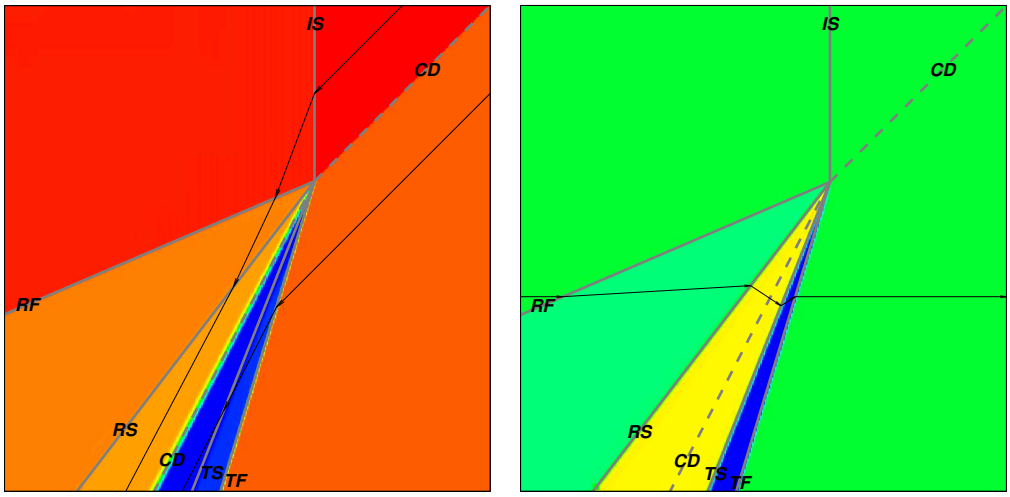

(a) (b)

Figure 5.6: Computed shock and CD angles for case S1 (c-solution) overlaid on (a) density contours and (b) B_y contours from the numerical results of Samtaney (2003). Sample streamlines and field lines are shown in (a) and (b), respectively.

streamlines are angled toward the SC. Shock RS then deflects them away from the shock normal, aligning them with the SC in region 3. Conversely, in region 4, the streamlines are angled away from the SC and shock TS brings them into alignment by deflecting them toward the shock normal. This type of deflection is not possible for hydrodynamic shocks as they do not support a tangential velocity jump. Figure 5.6(b) shows contours of B_y to clearly display the locations of the weaker shocks that have small density jumps across them. A typical magnetic field line is also plotted in this figure to show how the various shocks in the system deflect the field. Figure 5.7 shows normalized ρ and B_y profiles along a horizontal line that passes though RS, the SC, TS, and TF. Profiles from solution S1c are compared to those from the numerical results of Samtaney (2003). From Figures 5.6 and 5.7, it can be seen that there appears to be close agreement between solution S1c and the numerical results.

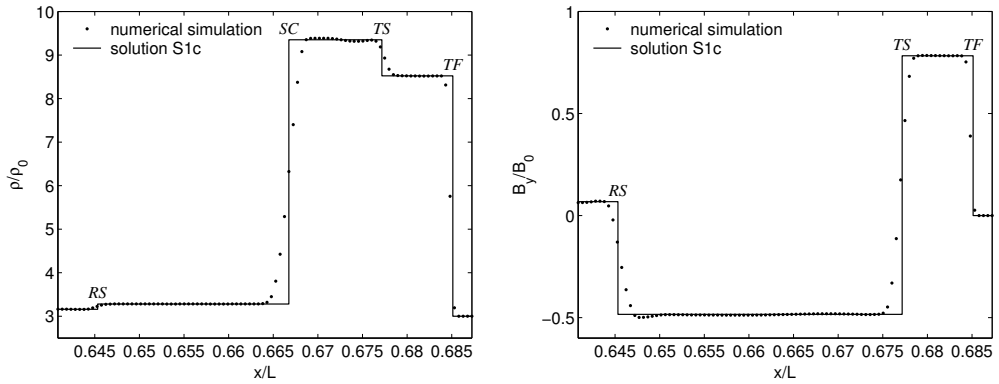

(a) (b)

Figure 5.7: Normalized profiles of (a) ρ and (b) B_y from the numerical results of Samtaney (2003) at $y/L = 0.62524$ compared to profiles from solution S1c. L is the vertical extent of the computational domain. RF is not shown because it is in a coarse region of the computational grid and is at a shallow angle to the x-axis, hence its structure is highly diffuse. The profiles have been aligned such that the center of the SC lies at the same location in each profile. They could not be aligned exactly due to the uncertainty in the location of the intersection point in the numerical results.

5.4.2 Regular solution

In general, two-dimensional c-solutions are not unique because a corresponding r-solution exists (see e.g., Torrilhon (2003b)). This is so for solution S1c. The corresponding r-solution, which we denote solution S1r, has the same structure except that the TS wave-group consists of a RD followed downstream by a slow shock. As this structure involves six shocks/RDs, it is referred to as a sextuple-point solution. The combined properties of the transmitted RD and slow shock are similar to those of the $2 \rightarrow 4$ intermediate shock in the c-solution; the sign of B_t is reversed and the flow is compressed. This allows the locations of the other shocks in the r-solution to remain relatively unchanged from solution S1c, as can be seen from examination of the shock angles. For solution S1r, these were found to be $\phi_1 = 0.405694$, $\phi_2 = 0.917019$, $\phi_3 = 1.27678$, and $\phi_4 = 1.19283$. With the exception of the angle of the transmitted slow shock, ϕ_4, these angles differ from those in solution S1c only in the sixth significant figure.

5.5 Transitions in solution type with decreasing magnetic field magnitude

We will now examine how solutions to the shock refraction problem vary with certain parameters. Our main focus will be on how the solutions change as β is increased. To study this, we have computed solutions along four lines in parameter space, which are defined in Table 5.1. Regular and irregular solution branches exist for each line. We begin our examination by identifying transitions in solution type that occur along the irregular branch associated with Line I (Branch Ic), for which solution S1c is the minimum β solution. The examination is repeated for the regular branch associated with Line I (Branch Ir). We then examine a number of mathematical solutions to the shock refraction problem that are non-evolutionary in both the planar and strongly planar MHD systems, according to FK. The branches associated with Lines II-IV indicate how the transition points vary for certain changes in M, η, and γ.

Line	I	II	III	IV
M	2	2	2	1.4
α	$\pi/4$	$\pi/4$	$\pi/4$	$\pi/4$
η	3	3	1.5	3
γ	1.4	5/3	5/3	5/3
β_{min}	2	2	2	2
$\beta_{max}^{(c)}$	61.6	9.28	34.0	49.5
$\beta_{max}^{(r)}$	2.39×10^7	102968	104385	103339

Table 5.1: Parameters defining Lines I-IV. $\beta_{max}^{(c)}$ and $\beta_{max}^{(r)}$ are the maximum values of β for the c- and r-branches associated with each line.

In Chapter 6, we extend this investigation to the limit of large β and examine how the limiting solutions are related to the hydrodynamic triple-point, which occurs for $\beta^{-1} = 0$.

5.5.1 Branch I*c*

We begin to follow Branch Ic by computing a solution for a value of β 0.001% greater than β_{min}, using the shock angles from solution S1c as the initial guesses in the iterative solution procedure. Two more solutions along the branch are then computed by successively incrementing β by 0.001% and using the previously computed shock angles as the initial guesses. Once these first four solutions have been obtained, the initial guesses for the shock angles are computed using third order extrapolation in β. This allows β to be increased by larger increments of 2% to 5% while still providing sufficiently accurate initial guesses for the iterative solution procedure to converge rapidly.

For the initial part of the solution branch beginning at $\beta_{min} = 2$, Figure 5.8(a) shows how the angles of fast shocks RF and TF deviate from their corresponding triple-point values; the angles of shocks R and T in hydrodynamic triple-point solution to the shock refraction problem with $M = 2$, $\eta = 3$, $\alpha = \pi/4$, $\gamma = 1.4$, and $\beta^{-1} = 0$.

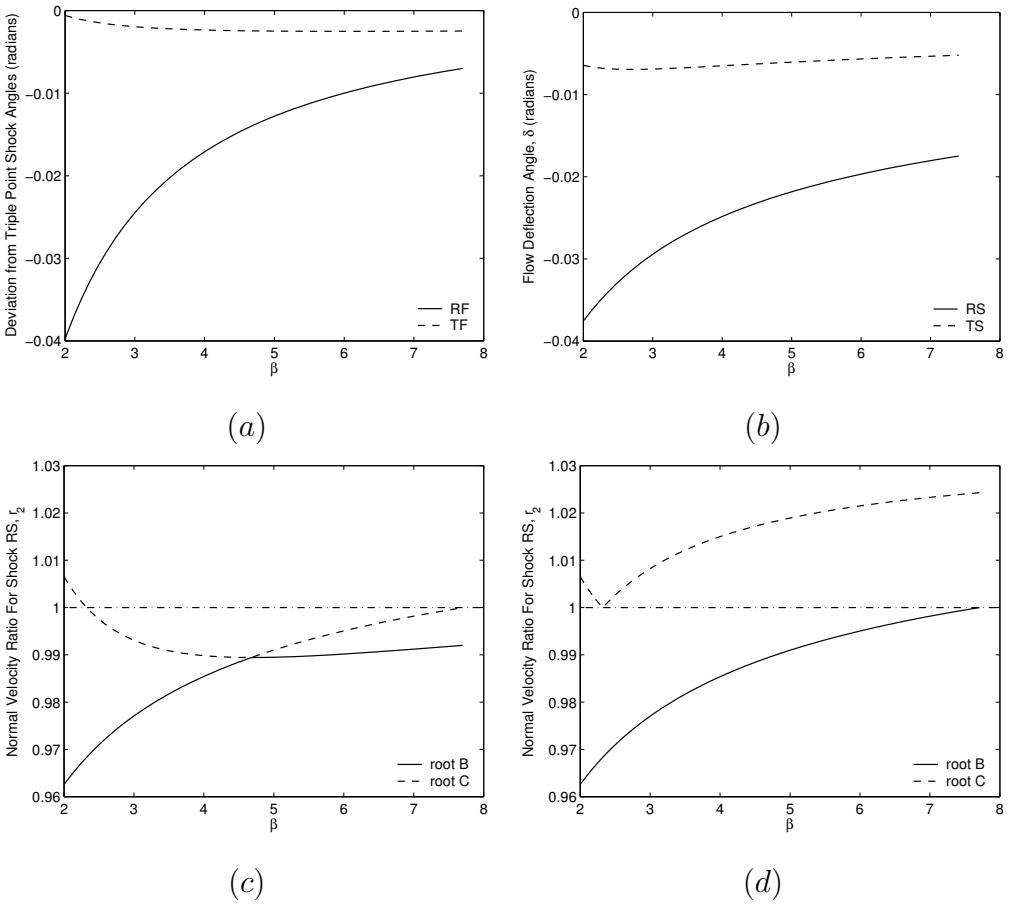

Figure 5.8: (a) Deviation of the fast shock angles from their corresponding values in the hydrodynamic triple-point, (b) angular deflection of the flow through RS and TS, and (c) roots B and C for the conditions upstream of RS for the initial part of solution Branch Ic (values of roots B and C for $\beta > 4.68$ are not associated with Branch Ic) with $M = 2$, $\eta = 3$, $\alpha = \pi/4$, and $\gamma = 1.4$. (d) Roots B and C for the conditions upstream of the slow shock in the RS wave-group for the initial part of solution Branch Ir.

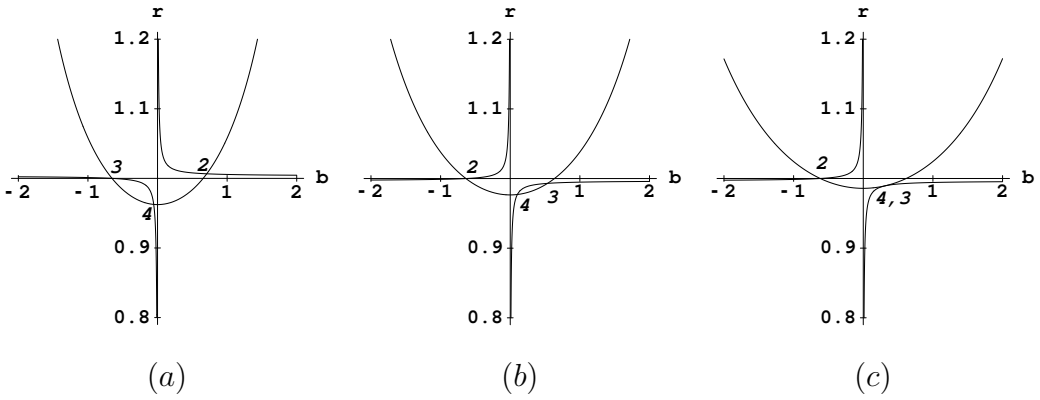

Figure 5.9: Graphical solutions of the MHD Rankine-Hugoniot relations for conditions upstream of shock RS along Branch Ic at (a) $\beta = 2$, (b) $\beta = 3$, and (c) $\beta = 4.68$.

This reveals that as β is increased, the fast shock angles tend toward their triple-point values. As this occurs, the misalignment between the flow in region 2 and that in region 4 decreases. Thus, the magnitudes of the angles through which shocks RS and TS must deflect the flow (δ_2 and δ_4 respectively) decrease, as can be seen from Figure 5.8(b). Figure 5.8(c) shows how the values of roots B and C vary for the conditions upstream of shock RS. At the beginning of Branch Ic, r_2 is given by root B, corresponding to a slow shock. As β is increased, the required decrease in the magnitude of δ_2 is achieved by the shock becoming weaker, as indicated by the value of r_2 increasing toward unity. At $\beta \approx 2.32$, the value of root C drops to 1 and RS is a switch-off shock. Beyond this, the value of root C drops below 1 so that the state upstream of RS now corresponds to intersection 2 of the $F = 0$ and $Z = 0$ curves. This implies that RS has transitioned from a slow shock to a $2 \rightarrow 4$ intermediate shock, as can be seen from Figures 5.9(a) and 5.9(b), which show the graphical solution to the RH relations for shock RS for values of β bracketing the transition point. We denote this a Slow-I24 transition.

Figure 5.8(c) shows that as β is increased further, roots B and C converge and become equal at $\beta \approx 4.68$, where RS is a $2 \rightarrow 3 = 4$ intermediate shock. At this value of β, the lower branch of the $Z = 0$ curve is tangent to the $F = 0$ curve, as shown

in Figure 5.9(c). For the solution branch to continue beyond this point, shock RS must continue to weaken as β increases. This may be achieved by RS transitioning from a $2 \rightarrow 4$ to a $2 \rightarrow 3$ intermediate shock, for which r_2 is given by root C instead of root B. We denote this a I24-I23 transition. Figure 5.8(c) shows that this transition allows r_2 to continue to increase smoothly for $\beta > 4.68$. According to FK, the $2 \rightarrow 3$ intermediate shock present in the solutions beyond the I24-I23 transition is non-evolutionary in both the planar and strongly planar MHD systems. For this reason, we do not consider these solutions as belonging to Branch Ic. Alternatively, Branch Ic may be continued via a slow-mode expansion fan appearing immediately downstream of the $2 \rightarrow 3 = 4$ intermediate shock, forming a C_1 compound wave that is evolutionary in the strongly planar system according to FK. We denote this a I24-C_1 transition. It was found that RS does not undergo any further transitions with increasing β after the I24-C_1 transition occurs. For Branch Ic, TS undergoes the Slow-I24 transition at $\beta \approx 0.964$, which is beyond where we have defined the end of Line I. For values of β just below this transition point, the c- and r-solutions are identical, but the solution branch terminates at $\beta \approx 0.952$ where the incident shock becomes non-evolutionary. TS was found to undergo the I24-C_1 transition at a slightly higher value of β than RS. All identified transition points are specified in Table 5.2.

5.5.2 Branch Ir

Solution S1r is the starting point for Branch Ir. As for Branch Ic, both RS and TS weaken (r and $|\delta|$ decrease) as β is increased along Branch Ir. RS is initially a slow shock with r_2 given by root B. It weakens to a switch-off shock at $\beta \approx 2.32$, where root C is equal to 1. This can be seen from Figure 5.8(d), which shows roots B and C for the conditions upstream of the slow shock in the RS wave-group along the initial portion of Branch Ir. Rather than undergoing a Slow-I24 transition at this point, a RD appears upstream of the shock. This event allows the sign of B_t to be reversed across the RS wave-group without the trailing shock becoming intermediate and is

denoted a Slow-RdSlow transition. Figure 5.8(d) shows that root C increases above unity after the Slow-RdSlow transition, confirming that the trailing shock remains slow. As β is increased beyond this transition point, the trailing slow shock continues to weaken. It becomes a slow magneto-acoustic wave that has no effect on the flow at $\beta \approx 7.71$, where r_2 reaches unity. In order for Branch Ir to continue for $\beta > 7.71$, the magnitude of δ_2 must be decreased further. This is achieved by the slow magneto-acoustic wave transitioning to a slow-mode expansion fan. We denote this process a RdSlow-RdExp transition. It was found that the RS wave-group does not undergo any further transitions with increasing β. The TS wave-group also undergoes the Slow-RdSlow and RdSlow-RdExp transitions, the locations of which are specified in Table 5.2.

Each possible combination of RS and TS wave-groups is referred to as a solution type. The ranges of β for which each solution type is valid are shown in Figure 5.10 for Branches Ic and Ir, along with the angular width of the inner layer. The angular width of the inner layer is defined as the angle from the leading wave in the RS wave-group to the leading wave in the TS wave-group. Also shown in Figure 5.10 are values of β for which we compare our results to the numerical simulations of Samtaney (2003) and present simulations of the same type.

5.5.3 Non-evolutionary solutions on Line I

For completeness, we will now briefly examine a number of mathematical solutions to the shock refraction problem that are non-evolutionary in both the planar and strongly planar MHD systems according to FK. Perhaps the most significant of these solutions are those involving $2 \rightarrow 3$ intermediate shocks. Such solutions can arise from RS and TS undergoing the I24-I23 transition identified in Section 5.5.1. As discussed in Section 5.3, other solutions involving $2 \rightarrow 3$ intermediate shocks may exist, but we have not investigated this. Computing the solutions in which RS and TS undergo the I24-I23 transition for increasing β along Line I, we find that r_2 reaches unity at $\beta \approx 7.71$, as can be seen from Figure 5.8(c). At this value of β, the reflected

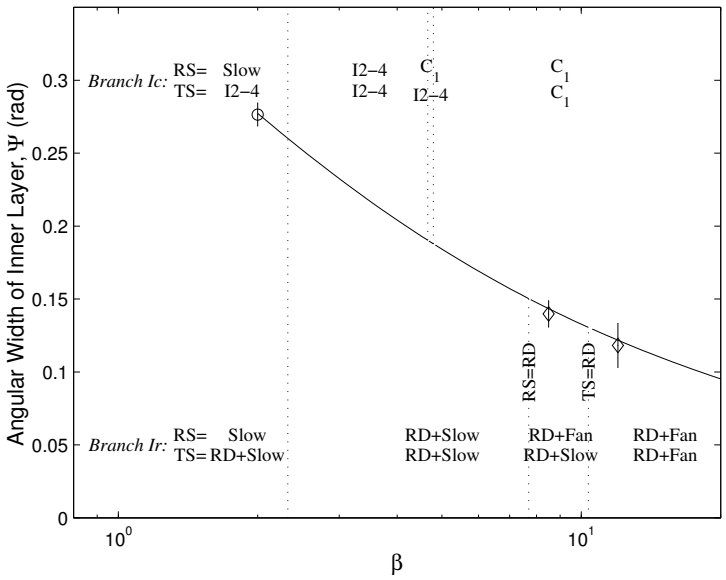

Figure 5.10: Locations of transitions in solution type with increasing β along Branches Ic and Ir ($M = 2$, $\eta = 3$, $\alpha = \pi/4$, $\gamma = 1.4$). The angular width of the inner layer (Ψ) from Branch Ic is indistinguishable from that from Branch Ir on the scale of this plot. I2-4 designates a $2 \rightarrow 4$ intermediate shock. $\circ$ indicate inner layer widths from the numerical simulations of Samtaney (2003). $\diamond$ indicate inner layer widths from present numerical simulations. The error bars correspond to 95% confidence intervals for the inner layer widths computed from the numerical simulations.

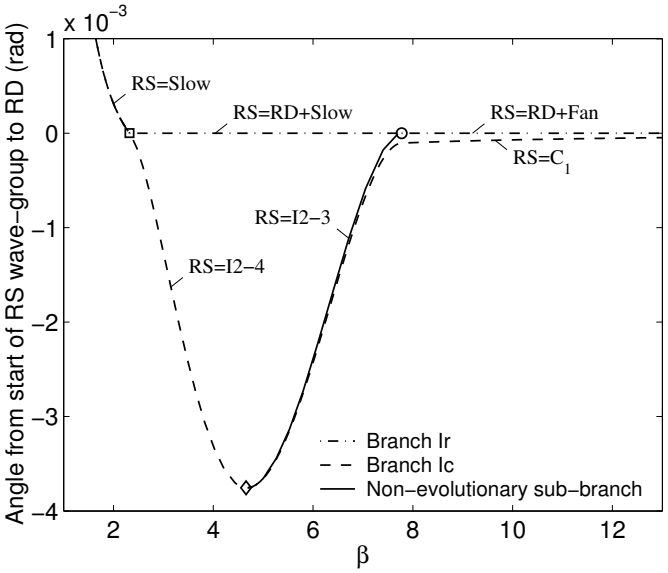

Figure 5.11: Angular separation between the leading wave in the RS wave-group and the location where a reflected RD would appear in solutions along the various branches associated with Line I. Note that, in many solutions, the RD is non-existent. □ indicates the Slow-RdSlow/Slow-I24 transition point. ◇ indicates the I24-C_1/I24-I23 transition point. ○ indicates the RdSlow-RdExp/I23-RdExp transition point. Note also that the pairs of transition points (e.g., the Slow-RdSlow and Slow-I24 transition points) may not coincide exactly, although they appear to do so on the scale of this plot. I2-3 and I2-4 designate $2 \rightarrow 3$ and $2 \rightarrow 4$ intermediate shocks, respectively.

$2 \rightarrow 3$ intermediate shock has weakened to the point where it has become a RD. For the non-evolutionary sub-branch (set of solutions valid along a portion of Line I) to continue for $\beta > 7.71$, the magnitude of δ_2 must decrease further. This can be achieved computationally via an expansion shock, for which $r > 1$. Expansion shocks, however, are entropy decreasing and thus non-physical. Alternatively, a slow-mode expansion fan may be introduced downstream of the RD to turn the flow toward the SC and bring it into alignment with that in region 5. We denote this a I23-RdExp transition. After both RS and TS undergo the I23-RdExp transition, the solutions lie on Branch Ir and are evolutionary in the planar system according to FK. Figure 5.11 illustrates the relationships between the various branches associated with Line I. It shows the angle between the leading wave in the RS wave-group and the location where a reflected RD would occur in solutions along Line I. This angle is zero when the RS wave-group contains a RD. Note that the transitions of TS must also be considered to gain a complete understanding of the branch structure.

It is possible to find solutions that satisfy Eqs. 5.11-5.15 where the RS and TS wave-groups consist of a RD followed by an expansion fan for values of β below their RdSlow-RdExp transition points. These solutions require the final expansion fan wavelets to be positioned upstream of the leading wavelets, hence they are non-physical.

Additional non-evolutionary solutions are possible if RS and TS undergo different transitions. For example, if RS undergoes Slow-RdSlow and RdSlow-RdExp transitions while TS undergoes Slow-I24 and I24-C_1 transitions, or vice-versa. After RS and TS have each undergone at least one transition, these solutions are not evolutionary in either the planar or strongly planar systems, hence we have not studied them in detail.

5.5.4 Lines II-IV

We will now investigate whether the same set of transitions occurs along Lines II-IV, which are defined in Table 5.1. The minimum β end-points of these branches

		Line			
Shock	Transition Pair	I	II	III	IV
	Slow-RdSlow/Slow-I24	2.32	2.48	10.2	13.8
RS	I24-C_1/I24-I23	4.68	4.96	20.3	28.2
	RdSlow-RdExp/I23-RdExp	7.71	8.17	34.0	47.3
	Slow-RdSlow/Slow-I24	0.964	1.11	5.12	9.13
TS	I24-C_1/I24-I23	4.79	4.50	16.3	25.2
	RdSlow-RdExp/I23-RdExp	10.2	9.28	32.6	48.5

Table 5.2: Values of β where transitions in solution type occur for Lines I-IV. The values of β given are accurate to the displayed number of significant figures. Pairs of transitions, such as the I24-C_1 and I24-I23 transitions, occur at the same β value up to accuracy displayed here. Not all pairs of transitions necessarily coincide.

are denoted as cases S2, S3, and S4, respectively. The parameters for case S2 are the same as those for case S1 with the exception of γ, which is increased to 5/3, a value more typically associated with plasma. The c- and r-solutions to case S2 were found by following the solution branches corresponding to increasing γ from the case S1 solutions. No transitions in solution type occur along these branches. For case S3, η is set to 1.5 to investigate the effects of reducing the density ratio. The other parameters are identical to those for case S2. Along the regular and irregular solution branches between the case S2 and case S3 solutions, the RS wave-group undergoes I24-Slow and RdSlow-Slow transitions, respectively. For case S4, M is set to 1.4 to investigate the effects of reducing the Mach number. The other parameters are identical to those for case S2. Along the regular and irregular solution branches between the case S2 and case S4 solutions, the RS wave-group undergoes I24-Slow and RdSlow-Slow transitions, respectively.

The branches associated with Lines II-IV emanate from the solutions to cases S2-S4, respectively, and are computed for increasing β in the same manner as Branch Ic. The sets of transitions in solution type that occur along Lines II-IV were found to

be the same as those along Line I, but the order in which the transitions occur was found to vary. Along Lines II and IV, TS undergoes the I24-C_1/I24-I23 transition before RS, but RS is the first to undergo the RdSlow-RdExp/I23-RdExp transition. Along Line III, TS undergoes all transitions at lower values of β than RS. The values of β at which the transitions occur along all solution branches investigated are listed in Table 5.2. Note that while the pairs of transitions, such as the I24-C_1 and I24-I23 transitions, occur at the same β value up to accuracy displayed in the table, not all pairs of transitions necessarily coincide exactly. From this table, we see that the increase in γ from Line I to Line II causes all transitions of TS except for the Slow-RdSlow to occur earlier, while it delays the transitions of RS. Both the decrease in M from Line II to Line III and the decrease in η from Line II to Line IV cause all transitions to occur at significantly larger β values.

5.6 Summary

We have developed an iterative procedure for determining the flow structure produced by the regular refraction of a MHD shock at an oblique planar density interface with a density ratio larger than unity. This procedure was used to reproduce the quintuple-point structure observed in the numerical simulations of Samtaney (2003). The quintuple-point structure is similar to the hydrodynamic triple-point, but with the SC replaced with two sub-fast shocks bracketing a MHD CD. The features of this structure were described in detail and there was found to be excellent agreement between our results and those of Samtaney (2003). For Samtaney's conditions, one of the sub-fast shocks is a $2 \rightarrow 4$ intermediate shock. A second solution was computed in which the intermediate shock was replaced by a 180^o rotational discontinuity followed downstream by a slow shock. This is referred to as a regular solution while the quintuple-point structure involving the intermediate shock is referred to as being irregular. For the three-dimensional ideal MHD equations, all waves that appear in regular solutions are admissible under the evolutionary condition according to Falle and Komissarov (2001). While for the strongly planar ideal MHD equations, in which

gradients and vectors are restricted to a plane (in some reference frame), all waves that appear in irregular solutions are admissible under the evolutionary condition.

For four sets of parameters, regular and irregular solution branches corresponding to increasing β were traced. It was found that as β is increased, the two shocks bracketing the SC undergo a number of transitions. Along each regular branch, the initial transitions are from slow shocks to 180^o rotational discontinuities followed downstream by slow shocks. As β is increased further, these transition to 180^o rotational discontinuities followed downstream by slow-mode expansion fans. Along each irregular solution branch, the transitions are from slow shocks to $2 \rightarrow 4$ intermediate shocks and finally to C_1 compound waves with increasing β.

Once all transitions are complete, we identified two possible flow structures that may arise from the shock refraction process: an irregular quintuple-point solution consisting of a hydrodynamic shock, two fast shocks, and two C_1 compound waves, and a seven wave regular solution consisting of a hydrodynamic shock, two fast shocks, two 180^o rotational discontinuities, and two slow-mode expansion fans, along with the contact discontinuity. The seven wave structure is denoted the septuple-point solution. The quintuple-point and septuple-point solutions remain valid up to the largest β values investigated using the iterative procedure.

Chapter 6

MHD Shock Refraction Problem for Vanishing Magnetic Field

6.1 Introduction

In this chapter, we address how the solutions to the MHD shock refraction problem identified in Chapter 5 approach the hydrodynamic triple-point in the limit of vanishing applied magnetic field. At values of β higher than the transition points listed in Table 5.2, we have identified two flow structures that may be produced by the shock refraction process for each of the four parameter sets considered. These two structures are the *septuple-point* r-solution, which consists of a combination of seven shocks, RDs, and expansion fans, and a *quintuple-point* c-solution consisting of a combination of five shocks and compound waves. The behavior of these solutions at large β is the topic of the following subsections. We present the behavior of the septuple-point first because it is more geometrically complex and efficient to compute for reasons that will be discussed in Section 6.2.2. In Section 6.3, the equations governing the leading order asymptotic solution of the shock refraction problem in the limit of large β are derived. The section concludes with a comparison between the asymptotic and full solutions. Finally, the work presented this chapter is summarized in Section 6.4.

6.2 Behavior of solutions at large β

6.2.1 Behavior of septuple-point solutions at large β

The structure of the septuple-point r-solution is illustrated in Figure 6.1(a). In the septuple-point solution, RF and TF are fast shocks, the RS wave-group consists of a RD, labeled RRD, followed downstream by a slow-mode expansion fan, labeled $RFan$, and finally, the TS wave-group consists of a RD, labeled TRD, followed downstream by a slow-mode expansion fan, labeled $TFan$. Following Branch Ir revealed that the septuple-point flow structure is maintained for β values up to 2.39×10^7. Solutions for β values greater than this were not computed.

Figure 6.1(b) reveals that as the magnetic field weakens, the angular width of the inner layer Ψ diminishes, while Figure 6.1(c) shows that the shock locations converge to their corresponding triple-point values for large β. The slope of the Ψ versus β^{-1} curve, when plotted on a logarithmic scale, reveals thatΨ scales like $\beta^{-1/2}$, which is proportional to the applied magnetic field magnitude B. Figure 6.1(d) shows the jump in velocity tangential to the SC across the inner layer, $\Delta u_{t\,inner}$, normalized by the jump in tangential velocity across the SC in the corresponding triple-point solution, $\Delta u_{t\,hydro}$. This reveals that as β becomes large, $\Delta u_{t\,inner}$ converges to $\Delta u_{t\,hydro}$. These observations suggest that, in the limit as $\beta \to \infty$, the septuple-point solution is identical to the hydrodynamic triple-point solution, with the exception that the hydrodynamic CD is replaced by the inner layer. The density and tangential velocity jumps across the inner layer, which are equal to those across the hydrodynamic CD in the limit, are supported by different elements within the layer. The density jump is principally supported by the MHD CD, but as this cannot support a shear, the tangential velocity jump must be supported by the RDs and expansion fans. Profiles of the tangential velocity within the inner layer for $\beta \approx 10.56$ and $\beta \approx 255,306$ are shown in Figure 6.2. These demonstrate that for moderate β, the tangential velocity jump is principally supported by the RDs, while for large β, it is almost entirely supported by the expansion fans. This is due to the fact that the tangential velocity jump across a RD scales like $(\sqrt{\gamma\,\rho/p}\,\beta\,M_{Sn})^{-1}$, which can be derived from Eq. C.12.

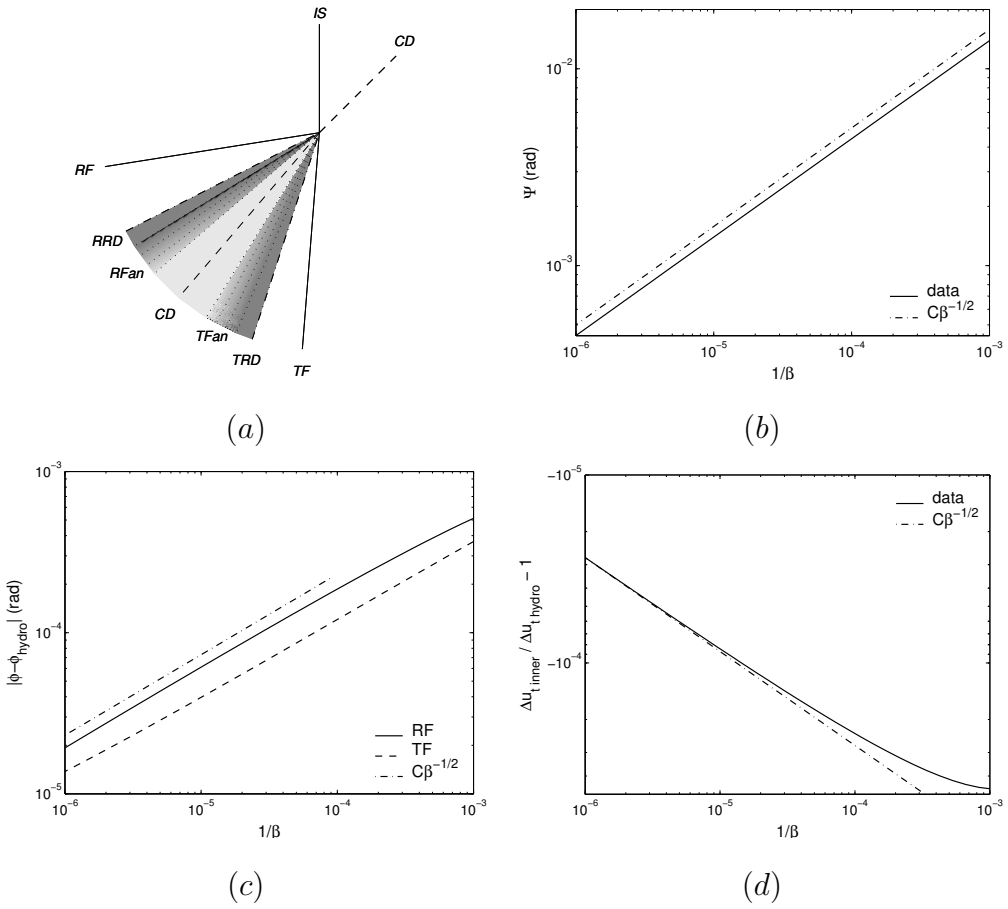

Figure 6.1: (a) Illustration of the septuple-point flow structure. The angular separations of the RDs and fans along with the angular extent of the fans have been exaggerated for clarity. (b) Variation of the angular width of the inner layer Ψ with β^{-1}. (c) Deviation of the angles of shocks RF and TF from their hydrodynamic triple-point values, ϕ_{hydro}, versus β^{-1}. (d) β^{-1} dependence of the tangential velocity jump across the inner layer, $\Delta u_{t\,inner}$, normalized by the tangential velocity jump across the CD in the corresponding hydrodynamic triple-point solution, $\Delta u_{t\,hydro}$. Logarithmic axes are used for (b)-(d) to illustrate the power law dependence of the plotted quantities on β^{-1}. Sample power law curves are included for comparison.

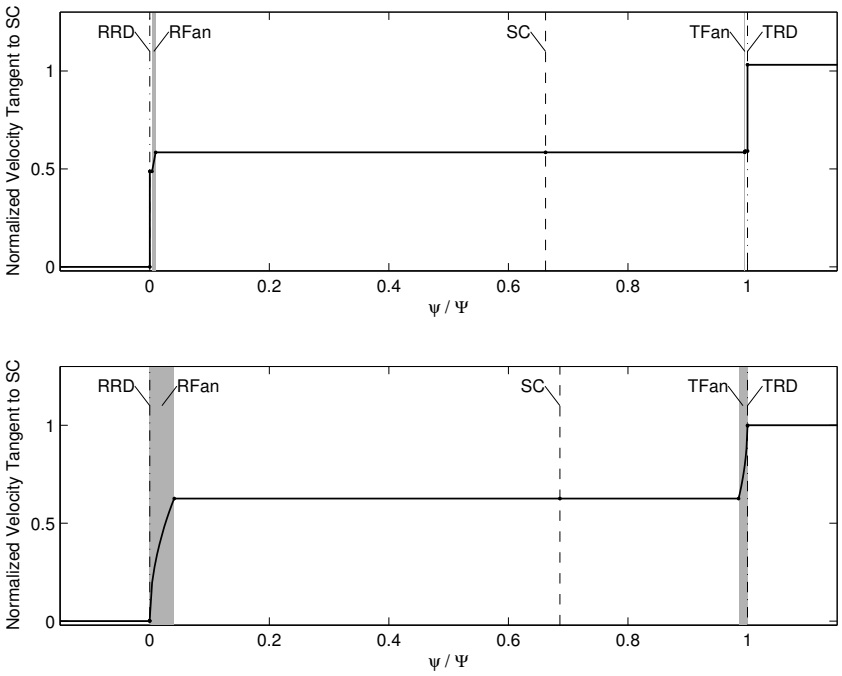

Figure 6.2: Velocity profiles within the inner layer of the septuple-point solution for two values of β along Branch Ir. The plotted velocity component is tangential to the SC and has been normalized such that it is zero at $\psi = 0$ and unity at $\psi = \Psi$. The top profile is for $\beta \approx 10.56$ and the bottom profile is for $\beta \approx 255606$. The angle ψ is defined counter-clockwise from RRD.

From our results, we also observe that for large β, each expansion fan supports finite jumps in ρ, p, and B_t to balance the tangential velocity jump. This implies that *while B_t tends to zero outside of the inner layer, it remains finite downstream of the expansion fans.* Further, Figure 6.2 shows that for large β, the angular extents of fans $RFan$ and $TFan$ still consume a finite fraction of the width of the inner layer. These findings indicate that in the limit of β tending to infinity, the inner layer is a singular structure.

6.2.2 Behavior of quintuple-point solutions at large β

The structure of the quintuple-point c-solution is illustrated in Figure 6.3(a). In the quintuple-point solution, RF and TF are fast shocks while RS and TS are C_1 compound waves labeled RC_1 and TC_1, respectively. We will refer to the expansion fan

portions of RC_1 and TC_1 as $RFan$ and $TFan$, respectively. Following Branch Ic revealed that the quintuple-point flow structure is maintained up to the highest β values for which solutions were computed. We discontinued following Branch Ic after establishing that its behavior is practically identical to that of Branch Ir. The reason that Branch Ic was not followed to the same β_{max} as Branch Ir is that solutions along this sub-branch are much more computationally expensive to calculate for large β. The additional expense arises from computing the angles of the $2 \rightarrow 3 = 4$ intermediate shocks. Computing these angles requires Eq. E.1 to be solved iteratively. For large β, we observe that the coefficients $\mathcal{B}$, $\mathcal{C}$, and $\mathcal{D}$ in this equation approximately scale like β. Thus, the terms in Eq. E.1 approximately scale like β^3 as they involve triple products of these coefficients. Satisfying Eq. E.1 to the same absolute tolerance for all β therefore requires the working precision of the iterative scheme to be increased like β^3, as the terms become large, greatly increasing the computational expense.

Figures 6.3(b) and 6.3(c) show comparisons of Ψ and the fast shock angles from Branches Ic and Ir. These demonstrate that the behavior of the quintuple-point and septuple-point solutions is practically identical, despite the structural differences between the two solutions. Figure 6.3(d) shows how the values of r for the reflected and transmitted $2 \rightarrow 3 = 4$ intermediate shocks vary with increasing β. It suggests that for large β, r tends toward unity for both shocks while they continue to reverse the sign of B_t as they are of an intermediate shock-type. This indicates that the $2 \rightarrow 3 = 4$ intermediate shocks reproduce the behavior of the RDs in the septuple-point for large β, implying that in the limit of β tending to infinity, the tangential velocity jump across the inner layer is supported by $RFan$ and $TFan$. Additionally, Figure 6.3(b) shows that the angular width of the inner layer scales like $\beta^{-1/2}$; hence the angular extents of $RFan$ and $TFan$ tend to zero for large β, as in the septuple-point solution. These results show that in the limit of β tending to infinity, the inner layer of the quintuple-point solution is also a singular structure as the expansion fans support finite jumps in u_t, B_t, ρ, and p while their angular extents tend to zero. We will now investigate this singular structure in more detail.

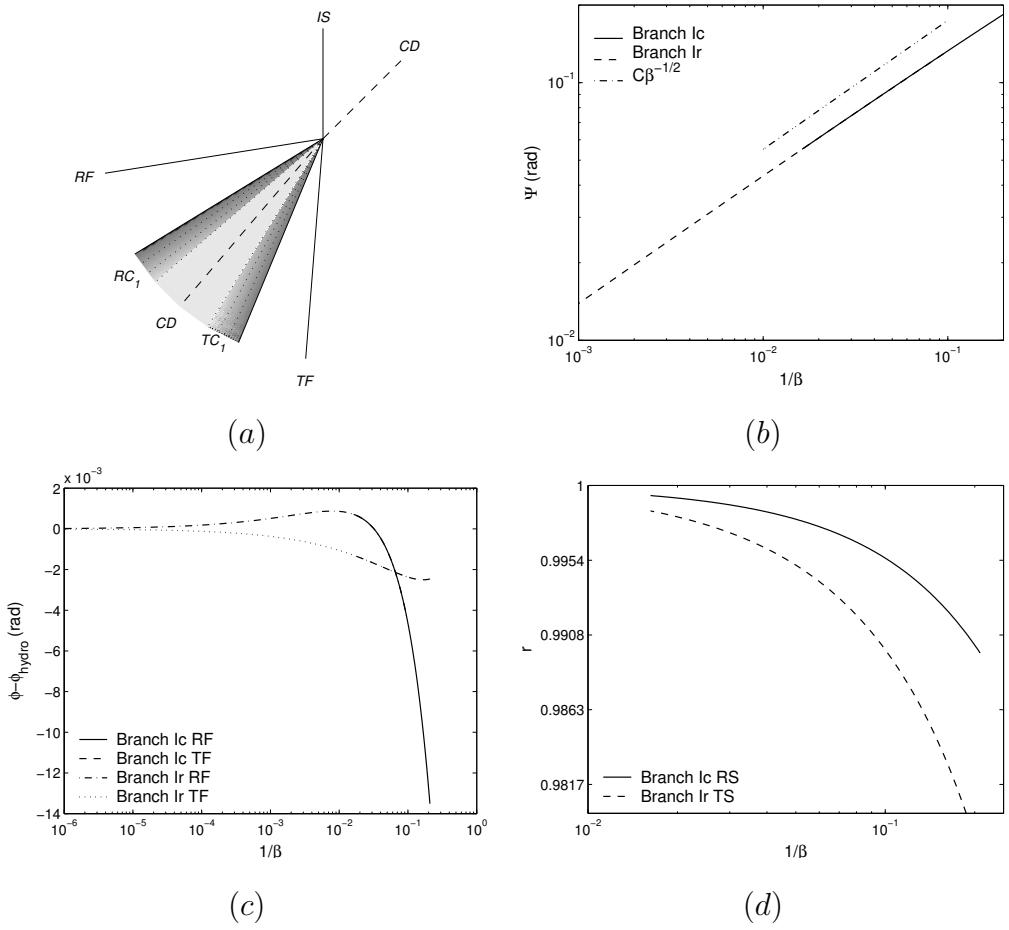

Figure 6.3: (a) Illustration of the quintuple-point flow structure. (b) Variation of the angular width of the inner layer Ψ with β^{-1} for Branches Ic and Ir. (c) Deviation of the angles of shocks RF and TF from their hydrodynamic triple-point values, ϕ_{hydro}, versus β^{-1} for Branches Ic and Ir. (d) β^{-1} dependence r for the transmitted and reflected $2 \rightarrow 3 = 4$ intermediate shocks, denoted RI and TI, respectively, along Branch Ic.

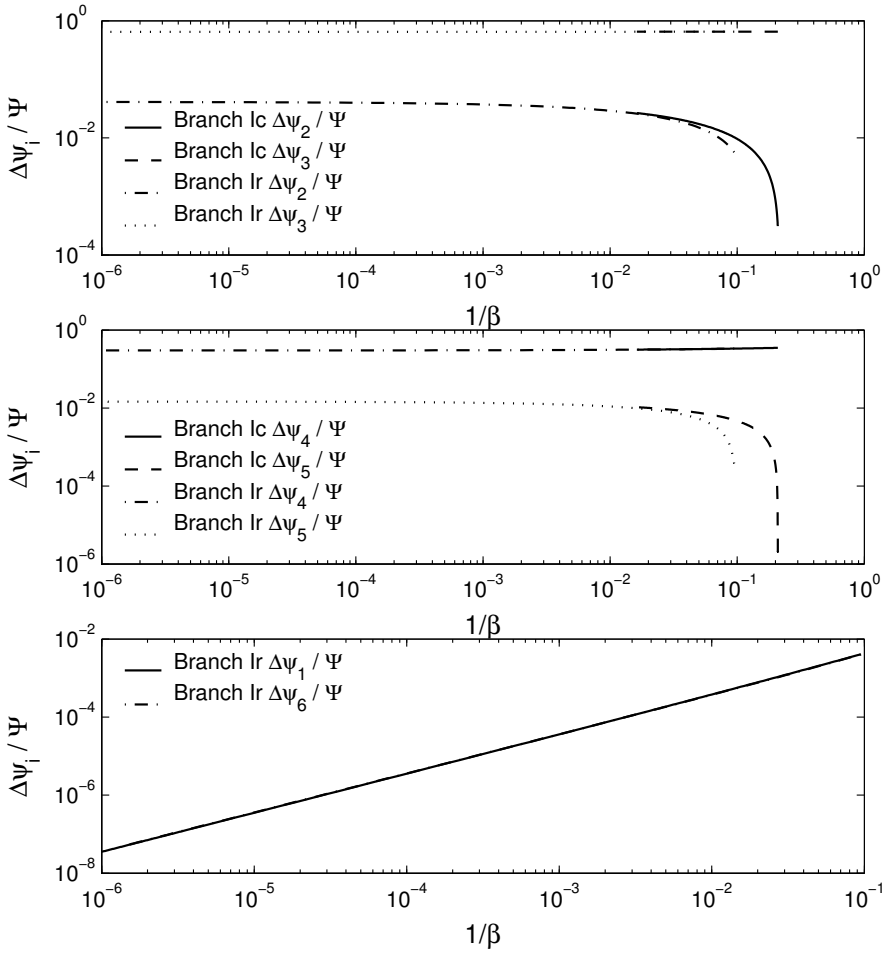

Figure 6.4: Variation of the sector widths within the inner layer along Branches Ic and Ir.

6.3 Structure of the singular wedge

6.3.1 Rescaling within the singular wedge

In the septuple-point solution, we denote the angle between RRD and the leading wavelet of $RFan$ as $\Delta\psi_1$, the angular extent of $RFan$ as $\Delta\psi_2$, the angle between the last wavelet of $RFan$ and the SC as $\Delta\psi_3$, the angle between the SC and the last wavelet of $TFan$ as $\Delta\psi_4$, the angular extent of $TFan$ as $\Delta\psi_5$, and the angle between the leading wavelet of $TFan$ and TRD as $\Delta\psi_6$. In the quintuple-point solution, $\Delta\psi_2$-$\Delta\psi_5$ are defined in the same way while $\Delta\psi_1$ and $\Delta\psi_6$ are both zero. Figure 6.4 shows how these sector widths vary with β^{-1} along Branches Ic and Ir. For both

branches, each of $\Delta\psi_2/\Psi$, $\Delta\psi_3/\Psi$, $\Delta\psi_4/\Psi$, and $\Delta\psi_5/\Psi$ asymptote to constant values for large β, indicating that these sector widths have the same $\beta^{-1/2}$ scaling as Ψ. Note that each of these scaled sector widths appear to asymptote to the same value for both branches. For the septuple-point solution, both $\Delta\psi_1$ and $\Delta\psi_6$ scale like β^{-1}; hence, they are small when compared to the other sector widths in the limit of large β. Further interrogation of the solutions along Line I revealed that within the inner layer (i.e. downstream of $RFan$ and $TFan$), M_{Sn} and K_n scale like $\beta^{-1/2}$ for large β. Conversely, ρ, p, M_{St}, and K_t remain finite. This implies that *even as $\beta \to \infty$, the magnetic field within the inner layer is finite* and scales like $\sqrt{\mu_0 p_3}$. In addition, the SC cannot support a tangential velocity jump as the magnetic field is not parallel to it.

The observed dependence of the inner layer flow states on β suggests the follow expansions in terms of the small parameter $\varepsilon \equiv \beta^{-1/2}$:

$$M_{Sn}(\zeta;\,\varepsilon) = \varepsilon M_{Sn}^{(1)}(\zeta) + \varepsilon^2 M_{Sn}^{(2)}(\zeta) + O(\varepsilon^3)\,, \tag{6.1}$$

$$M_{St}(\zeta;\,\varepsilon) = M_{St}^{(0)}(\zeta) + \varepsilon M_{St}^{(1)}(\zeta) + O(\varepsilon^2)\,, \tag{6.2}$$

$$K_n(\zeta;\,\varepsilon) = \varepsilon K_n^{(1)}(\zeta) + \varepsilon^2 K_n^{(2)}(\zeta) + O(\varepsilon^3)\,, \tag{6.3}$$

$$K_t(\zeta;\,\varepsilon) = K_t^{(0)}(\zeta) + \varepsilon K_t^{(1)}(\zeta) + O(\varepsilon^2)\,, \tag{6.4}$$

$$\rho(\zeta;\,\varepsilon) = \rho^{(0)}(\zeta) + \varepsilon \rho^{(1)}(\zeta) + O(\varepsilon^2)\,, \tag{6.5}$$

where $\zeta \equiv \psi/\varepsilon$. For each expansion fan, ζ originates from the leading wavelet and increases in the downstream direction. Substituting these expansions into Eqs. D.9-D.13, we obtain the following set of coupled differential equations in ζ for the leading

order terms within $RFan$ and $TFan$:

$$\frac{d\rho^{(0)}}{d\zeta} = \rho^{(0)} f_\rho \,, \tag{6.6}$$

$$\frac{dM_{Sn}^{(1)}}{d\zeta} = -\left(\frac{\gamma+1}{2} M_{Sn}^{(1)} f_\rho + M_{St}^{(0)}\right) , \tag{6.7}$$

$$\frac{dM_{St}^{(0)}}{d\zeta} = -\left(\frac{\gamma}{2}\frac{M_{Sn}^{(1)}}{K_n^{(1)} K_t^{(0)}} + \frac{K_t^{(0)}}{K_n^{(1)}} M_{Sn}^{(1)} + \frac{\gamma-1}{2} M_{St}^{(0)}\right) f_\rho \,, \tag{6.8}$$

$$\frac{dK_n^{(1)}}{d\zeta} = -\left(\frac{\gamma}{2} K_n^{(1)} f_\rho + K_t^{(0)}\right) , \tag{6.9}$$

$$\frac{dK_t^{(0)}}{d\zeta} = -\frac{\gamma}{2}\left(\frac{1}{K_t^{(0)}} + K_t^{(0)}\right) f_\rho \,, \tag{6.10}$$

where,

$$f_\rho = \frac{-2 M_{Sn}^{(1)} M_{St}^{(0)} \left(1 + \frac{2}{\gamma} {K_t^{(0)}}^2\right) + \frac{4}{\gamma} K_n^{(1)} K_t^{(0)}}{\left[\gamma + 3 + \left(4 + \frac{2}{\gamma}\right) {K_t^{(0)}}^2\right] {M_{Sn}^{(1)}}^2 - 2 {K_n^{(1)}}^2} \,.$$

The source of the observed singular change in the tangential magnetic field across each expansion fan is the term involving $1/K_t^{(0)}$ in Eq. 6.10. At the leading wavelet of an expansion fan, where $K_t^{(0)} = 0$, this causes the ζ-derivative of $K_t^{(0)}$ to be infinite. Within the expansion fans, we find that to leading order in ζ, $K_t^{(0)}$ behaves like $\sqrt{\zeta}$ near $\zeta = 0$.

Computing the leading order asymptotic approximation to the inner layer structure in the limit of large β requires Eqs. 6.6-6.10 to be solved. To achieve this, boundary conditions for each of these equations are necessary. The boundary conditions for the $O(1)$ quantities $\rho^{(0)}$, $M_{St}^{(0)}$, and $K_t^{(0)}$ are the values on either side of the SC in the corresponding hydrodynamic triple-point solution (zero in the case of $K_t^{(0)}$). Obtaining boundary conditions for $M_{Sn}^{(1)}$ and $K_n^{(1)}$ requires the $O(\varepsilon)$ quantities outside of the inner layer to be computed. In Appendix G, we show that the $2 \rightarrow 3 = 4$ intermediate shocks in the quintuple-point solution and the RDs in the septuple-point solution do not affect the boundary conditions for Eqs. 6.6-6.10 and hence are omitted from the leading order solution. Combined with other arguments, this implies that the leading order asymptotic solution is the large β limit of both the

quintuple-point and septuple-point solutions.

6.3.2 Equations for $O(\varepsilon)$ quantities outside the singular wedge

In each region outside of the inner layer, ρ, p, and $\mathbf{u}$ can be expanded about their values in the triple-point solution, which are denoted with the superscript (0). For example,

$$\rho(\phi;\,\varepsilon) = \rho^{(0)}(\phi) + \varepsilon\rho^{(1)}(\phi) + O(\varepsilon^2)\,.$$

From the definition of ε, the appropriate expansion for the magnetic field is

$$\mathbf{B}(\phi;\,\varepsilon) = \varepsilon\mathbf{B}^{(1)}(\phi) + O(\varepsilon^2)\,.$$

As I is a hydrodynamic shock, the presence of $\mathbf{B}$ does not perturb the hydrodynamic variables in region 1. Thus, $\rho_1 = \rho_1^{(0)}$, $p_1 = p_1^{(0)}$, and $\mathbf{B}_1 = \varepsilon\mathbf{B}_{1nu}^{(1)}\hat{\mathbf{e}}_x = -\varepsilon\sqrt{2\,\mu_0 p_0}\,\hat{\mathbf{e}}_x$. Here, $\hat{\mathbf{e}}_x$ is a unit vector oriented in the $x-$direction. From our examination of Branch Ir, we observe that the fast shock angles are perturbed about their triple-point values as follows:

$$\phi = \phi^{(0)} + \varepsilon\phi^{(1)} + O(\varepsilon^2)\,.$$

This perturbs the velocity components upstream of RF and TF about their triple-point values. We will denote vector components defined relative to plane waves forming the upstream and downstream boundaries of a region with the subscripts u and d respectively. The perturbed velocity components immediately upstream of RF are given by

$$\begin{aligned}
u_{1nd} &= u_{1nd}^{(0)} + \varepsilon u_{1nd}^{(1)} + O(\varepsilon^2) \\
&= -u_{1tu}^{(0)}\cos\phi_1^{(0)} - u_{1nu}^{(0)}\sin\phi_1^{(0)} + \varepsilon\phi_1^{(1)}\left(u_{1tu}^{(0)}\sin\phi_1^{(0)} - u_{1nu}^{(0)}\cos\phi_1^{(0)}\right) + O(\varepsilon^2)\,, \\
u_{1td} &= u_{1td}^{(0)} + \varepsilon u_{1td}^{(1)} + O(\varepsilon^2) \\
&= -u_{1tu}^{(0)}\sin\phi_1^{(0)} + u_{1nu}^{(0)}\cos\phi_1^{(0)} - \varepsilon\phi_1^{(1)}\left(u_{1tu}^{(0)}\cos\phi_1^{(0)} + u_{1nu}^{(0)}\sin\phi_1^{(0)}\right) + O(\varepsilon^2)\,,
\end{aligned}$$

while the $O(\varepsilon)$ magnetic field components are given by

$$B_{1nd} = \varepsilon B_{1nd}^{(1)} = -\varepsilon B_{1nu}^{(1)} \sin\phi_1^{(0)},$$
$$B_{1td} = \varepsilon B_{1td}^{(1)} = \varepsilon B_{1nu}^{(1)} \cos\phi_1^{(0)}.$$

The $O(\varepsilon)$ vector components upstream of TF are calculated in a similar manner.

The magnetic field just downstream of the fast shocks will also be $O(\varepsilon)$ because the shocks are not close to the switch-on limit. To compute the perturbed flow-states downstream of RF and TF ($2u$ and $4u$, respectively), shock jump conditions for the $O(\varepsilon)$ quantities are required. These are obtained by substituting our expansions for ρ, p, $\mathbf{u}$, and $\mathbf{B}$ into Eqs. 5.6-5.10 in the reference frame where $u_t^{(0)} = 0$. By setting the $O(1)$ terms of the resulting expressions equal to zero, we obtain the usual hydrodynamic shock jump conditions. Setting the $O(\varepsilon)$ terms equal to zero yields

$$\left[\rho^{(0)} u_n^{(1)} + \rho^{(1)} u_n^{(0)}\right] = 0 \ , \tag{6.11}$$

$$\left[2\rho^{(0)} u_n^{(0)} u_n^{(1)} + \rho^{(1)} {u_n^{(0)}}^2 + p^{(1)}\right] = 0 \ , \tag{6.12}$$

$$\left[u_t^{(1)}\right] = 0 \ , \tag{6.13}$$

$$\left[\frac{\left(\rho^{(1)} u_n^{(0)} + 3\rho^{(0)} u_n^{(1)}\right) {u_n^{(0)}}^2}{2} + \frac{\gamma\left(u_n^{(1)} p^{(0)} + u_n^{(0)} p^{(1)}\right)}{\gamma - 1}\right] = 0 \ , \tag{6.14}$$

$$\left[u_n^{(0)} B_t^{(1)}\right] = 0 \ . \tag{6.15}$$

These equations are not valid for shocks that are almost switch-on shocks. The values of $\rho^{(1)}$, $p^{(1)}$, and $u_n^{(1)}$ downstream of each fast shock are obtained by the simultaneous solution of Eq. 6.11, Eq. 6.12, and Eq. 6.14. Once $u_n^{(1)}$ is known on both sides of each shock, the downstream values of $B_t^{(1)}$ can be computed from Eq. 6.15. Eq. 6.13 shows that $u_t^{(1)}$ is continuous across each shock, as is $B_n^{(1)}$.

To compute the $O(\varepsilon)$ components of flow-states $2d$ and $4d$, which are defined relative to the leading wavelets of $RFan$ and $TFan$, respectively, we must first compute the $O(1)$ and $O(\varepsilon)$ terms in the expansions for $\Delta\phi_d$ (the angle between RF

and $RFan$) and $\Delta\phi_a$ (the angle between TF and $TFan$). This can be accomplished by substituting our expansions for the primitive variables into Eq. F.2 because we determined that the location of each leading wavelet is the same as that of a RD up to $O(\varepsilon)$. For $\Delta\phi_d$, this gives

$$\begin{aligned}\Delta\phi_d &= \Delta\phi_d^{(0)} + \varepsilon\Delta\phi_d^{(1)} + O(\varepsilon^2) \\ &= \arctan\frac{M_{Sn}^{(0)}}{M_{St}^{(0)}} + \frac{\varepsilon M_{Sn}^{(0)} M_{St}^{(0)}}{{M_{Sn}^{(0)}}^2 + {M_{St}^{(0)}}^2}\left[\frac{M_{Sn}^{(1)}}{M_{Sn}^{(0)}} - \frac{M_{St}^{(1)}}{M_{St}^{(0)}} - \sqrt{\frac{2}{\gamma}}\left(\frac{K_n^{(1)}}{M_{Sn}^{(0)}} - \frac{K_t^{(1)}}{M_{St}^{(0)}}\right)\right] + O(\varepsilon^2)\,,\end{aligned}$$

where the subscript $2u$ has been dropped from all quantities for clarity and

$$K_{n/t}^{(1)} = \frac{B_{n/t}^{(1)}}{\sqrt{2\mu_0 p^{(0)}}}\,, \tag{6.16}$$

$$M_{Sn/t}^{(1)} = M_{Sn/t}^{(0)}\left(\frac{u_{n/t}^{(1)}}{u_{n/t}^{(0)}} + \frac{\rho^{(1)}}{2\rho^{(0)}} - \frac{p^{(1)}}{2p^{(0)}}\right)\,. \tag{6.17}$$

Note that $\Delta\phi_d^{(0)}$ is equal to the angle between the reflected shock and the SC in the corresponding triple-point solution, a prerequisite for the $O(1)$ terms in our expansions corresponding to a triple-point solution. $\Delta\phi_a^{(1)}$ is computed by inserting flow-state 4u into the above relation for $\Delta\phi_d^{(1)}$ and inverting the direction of $\mathbf{K}_{4u}^{(1)}$. We can now compute $u_{2nd}^{(1)}$ using

$$u_{2nd}^{(1)} = -\Delta\phi_d^{(1)} u_{2td}^{(0)} + u_{2nu}^{(1)}\cos\Delta\phi_d^{(0)} - u_{2tu}^{(1)}\sin\Delta\phi_d^{(0)}\,.$$

A similar relation is used to compute $u_{4nd}^{(1)}$. From the hydrodynamic triple-point solution, both $u_{2nd}^{(0)}$ and $u_{4nd}^{(0)}$ are zero. This results in the inner layer boundary conditions for M_{Sn} being $O(\varepsilon)$, as required by Eq. 6.7. The leading order magnetic field components upstream of $RFan$ are given by

$$\begin{aligned}B_{2nd}^{(1)} &= B_{2nu}^{(1)}\cos\Delta\phi_d^{(0)} - B_{2tu}^{(1)}\sin\Delta\phi_d^{(0)}\,, \\ B_{2td}^{(1)} &= B_{2nu}^{(1)}\sin\Delta\phi_d^{(0)} + B_{2tu}^{(1)}\cos\Delta\phi_d^{(0)}\,.\end{aligned}$$

The components upstream of $TFan$ are computed in the same manner.

The boundary conditions for Eqs. 6.6-6.10 can now be computed from states $2d$ and $4d$ upstream of the fans; the boundary conditions for $\rho^{(0)}$, $p^{(0)}$, and $M_{St}^{(0)}$ are taken directly from the triple-point solution on either side of the shocked interface. Eq. 6.16 is used to calculate the boundary conditions for $K_n^{(1)}$ from states $2d$ and $4d$ while the boundary conditions for $M_{Sn}^{(1)}$ are computed using

$$M_{S2nd}^{(1)} = \frac{u_{2nd}^{(1)}}{\sqrt{\gamma p_2^{(0)}/\rho_2^{(0)}}}, \quad M_{S4nd}^{(1)} = \frac{u_{4nd}^{(1)}}{\sqrt{\gamma p_4^{(0)}/\rho_4^{(0)}}}.$$

Finally, the appropriate boundary conditions for $K_t^{(0)}$ are zero.

6.3.3 Leading order matching conditions at the interface

The leading order terms of flow-state $3u$ immediately downstream of the trailing wavelet of $RFan$ are computed by numerically integrating Eqs. 6.6-6.10 from $\zeta = 0$ to $\zeta = \Delta\zeta_2 \equiv \Delta\psi_2/\varepsilon$ using the boundary conditions derived in Section 6.3.2. Similarly, flow-state $5u$ is computed by numerically integrating Eqs. 6.6-6.10 from $\zeta = 0$ to $\zeta = \Delta\zeta_5 \equiv \Delta\psi_5/\varepsilon$. To leading order, the angular separations between the trailing wavelets of the expansion fans and the SC, $\varepsilon\Delta\zeta_3$ and $\varepsilon\Delta\zeta_4$, are given by

$$\Delta\zeta_3 = \frac{u_{3nu}^{(1)}}{u_{3tu}^{(0)}}, \quad \Delta\zeta_4 = \frac{u_{5nu}^{(1)}}{u_{5tu}^{(0)}}.$$

Using this, it can be shown that the leading order matching conditions for pressure, velocity magnitude, velocity direction, tangential magnetic field, and normal magnetic

field can be expressed as

$$p_3^{(0)} = p_5^{(0)}\,, \tag{6.18}$$

$$u_{3tu}^{(0)} = u_{5tu}^{(0)}\,, \tag{6.19}$$

$$\phi_1^{(1)} + \Delta\phi_d^{(1)} + \Delta\zeta_2 + \Delta\zeta_3 + \Delta\zeta_4 + \Delta\zeta_5 - \phi_3^{(1)} + \Delta\phi_a^{(1)} = 0\,, \tag{6.20}$$

$$K_{3tu}^{(0)} = K_{5tu}^{(0)}\,, \tag{6.21}$$

$$K_{3nu}^{(1)} - \Delta\zeta_3 K_{3tu}^{(0)} + K_{5nu}^{(1)} - \Delta\zeta_4 K_{5tu}^{(0)} = 0\,. \tag{6.22}$$

6.3.4 Leading order asymptotic solution technique

The leading order asymptotic solution is computed in the same manner as the solution to the full problem. The solution can be completely specified by four scaled angles, $\phi_1^{(1)}$, $\phi_3^{(1)}$, $\Delta\zeta_2$, and $\Delta\zeta_5$. An approximate solution is found by iterating on these four angles using a secant method until Eqs. 6.18-6.21 are satisfied to eight significant figures. To check the consistency of this procedure, the final angles are substituted into Eq. 6.22 to ensure that it is satisfied to the same precision. It was found that the radius of convergence for this set of equations is very small, necessitating extremely accurate initial guesses for the four angles to achieve a converged solution. One difficulty that arises in this problem is that the derivatives in Eqs. 6.8 and 6.10 are infinite at the leading wavelet of each expansion fan ($\zeta = 0$) as they contain terms involving $1/K_t^{(0)}$. Thus, they cannot be integrated numerically if the physical boundary condition $K_t^{(0)} = 0$ is used. This is handled by setting the boundary conditions on $K_t^{(0)}$ to be the small values $-\epsilon K_{2dt}^{(1)}$ and $-\epsilon K_{4dt}^{(1)}$ at the leading wavelets of $RFan$ and $TFan$, respectively. The value of ϵ used was 10^{-10}. This procedure is acceptable because in the immediate vicinity of the leading wavelet ($\zeta \ll 1$), the growth of $K_t^{(0)}$ is decoupled to leading order (in ζ) from changes in the other variables. For $\zeta \ll 1$, $K_t^{(0)}$ behaves like $\sqrt{\zeta}$ to leading order while the other variables are constant to leading order.

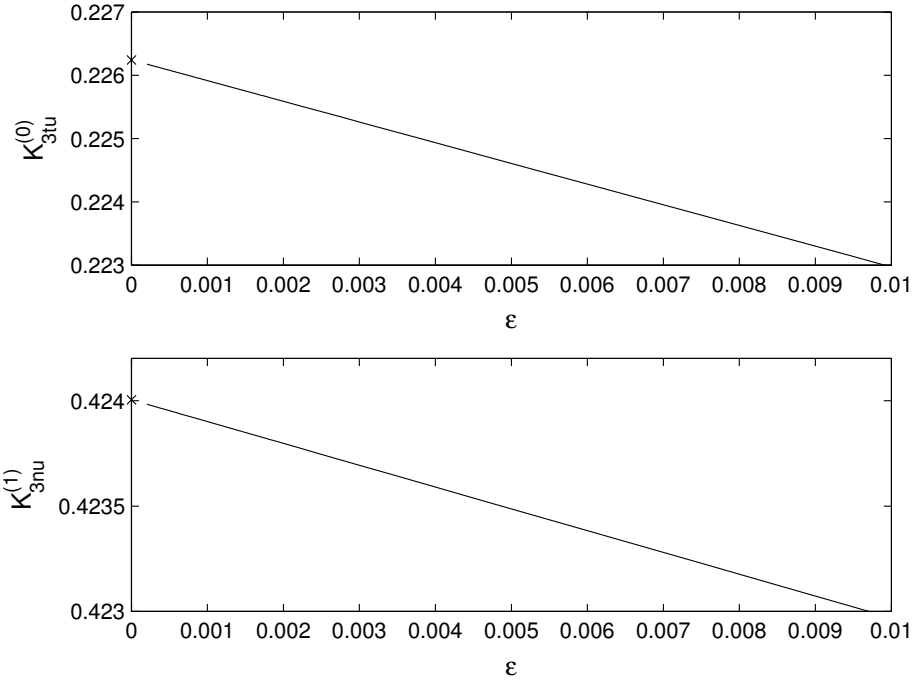

Figure 6.5: $K_{3t}^{(0)}$ and $K_{3n}^{(1)}$ values from the leading order asymptotic solution ($\times$) and approximated from Branch Ir ($-$) versus ε.

6.3.5 Comparing the full and asymptotic solutions

We have computed the leading order asymptotic solution to the shock refraction problem specified by the parameters defining Line I, which are listed in Table 5.1. For this set of parameters, we found that $\phi_1^{(1)} = 0.01981083$, $\phi_3^{(1)} = -0.01205304$, $\Delta\zeta_2 = 0.01814016$, and $\Delta\zeta_5 = 0.00646063$. The residual of Eq. 6.22 is less than 10^{-9} for this set of scaled angles.

Approximate values for $O(\varepsilon)$ terms can be recovered from the full solutions along Branches Ic and Ir. For example, an approximate value for $\phi_1^{(1)}$ can be computed using

$$\phi_{1\,approx}^{(1)} = \frac{\phi_1 - \phi_1^{(0)}}{\varepsilon},$$

where ϕ_1 and ε are taken from a full solution along either Branch Ic or Branch Ir. Note that these approximations have an error proportional to the value of ε for the full solution used. The approximate values of $\phi_1^{(1)}$, $\phi_3^{(1)}$, $\Delta\zeta_2$, and $\Delta\zeta_5$ from Branch Ir were extrapolated to $\varepsilon = 0$ and compared to the values from the leading order asymptotic

solution. The relative errors were found to be at most 7.7×10^{-6}, which is an order of magnitude less than the smallest value of ε from Branch Ir. Figure 6.5 shows a comparison between the values of representative $O(1)$ and $O(\varepsilon)$ inner layer quantities from the asymptotic solution and approximated from Branch Ir. In general, there was found to be excellent agreement between the leading order asymptotic solution and the full solutions at the end of Branch Ir in the limit of small ε.

6.4 Summary

Our results suggest that in the limit of infinite β, both the quintuple-point and septuple-point solutions identified in Chapter 5 become identical to the hydrodynamic triple-point solution, with the exception that the shocked hydrodynamic contact is replaced by a singular structure we call the inner layer. The inner layer is a wedge bounded by either the two compound waves or the two rotational discontinuities followed by the two slow-mode expansion fans. These bracket the MHD contact. In both cases, the angle of this wedge scales like $\beta^{-1/2}$, which is proportional to the applied magnetic field magnitude. A scaling for each of the variables within the inner layer is suggested from the results of our computations. Significantly, this scaling implies that the magnetic field within the inner layer is finite in the limit of β tending to infinity. In addition, the magnetic field is not parallel to the MHD contact, hence it cannot support a jump in tangential velocity. This necessitates the presence of the expansion fans (that are part of the compound waves in the quintuple-point solution), which support the tangential velocity discrepancy across the inner layer even though their angular extents tend to zero. To verify these findings, the equations governing the leading order asymptotic solution of the shock refraction problem in the limit of large β were derived. These equations were then solved iteratively. We argue that the leading order asymptotic solution is the large β limit of both the quintuple-point and septuple-point solutions, in part because neither the shock portions of the compound waves nor the rotational discontinuities participate in it. The asymptotic and full solutions were compared quantitatively and there was found to be excellent

agreement between the two. Although we have only examined the limit of infinite β in detail for one set of parameters, we anticipate that for all sets of parameters where the shock refraction is regular, a singular layer will be present in which the leading order behavior is also governed by slow-mode expansion fans.

Chapter 7

Conclusions

The Richtmyer-Meshkov instability (RMI) is important in a wide variety of applications including inertial confinement fusion (Lindl et al., 1992), astrophysical phenomena (Arnett, 2000), supersonic and hypersonic air breathing engines (Yang et al., 1993), deflagration-to-detonation transition (Khokhlov et al., 1999), and reflected shock tunnels (Stalker and Crane, 1978, Brouillette and Bonazza, 1999). In some of these applications, the fluids involved may be plasmas and hence be affected by magnetic fields. For one configuration, Samtaney (2003) has demonstrated, via numerical simulations, that the growth of the RMI in magnetohydrodynamics (MHD) is suppressed in the presence of a magnetic field. The extent and cause of this suppression were theoretically and numerically investigated in this thesis.

As a first step, ideal MHD simulations of the RMI of a sinusoidally perturbed interface were carried out, both in the presence and absence of a magnetic field. The results of these simulations, which are presented in Chapter 2, are in qualitative agreement with the simulations of Samtaney (2003), in which the interface was planar and oblique: When a magnetic field is present, additional MHD shocks are generated during the shock refraction process that transport vorticity away from the density interface, suppressing the growth of the RMI. The most significant result to arise from the simulations presented in Chapter 2 is that the interface amplitude still exhibits some growth in the presence of a magnetic field. The behavior of the interface amplitude in this case, a short period of growth followed by oscillations about a

constant mean, was not reported by Samtaney and was deemed to warrant further investigation.

To understand the behavior of the interface seen in Chapter 2, and the effect of a magnetic field on the MHD RMI in general, a linearized model problem is studied in Chapter 3. The model problem consists of a sinusoidally perturbed interface separating incompressible conducting fluids of different densities that is impulsively accelerated at $t = 0$. There is a magnetic field aligned with the impulsive acceleration. This flow was studied by analytically solving the appropriate linearized initial value problem. The solution indicates that the initial growth rate of the interface is unaffected by the presence of a magnetic field. The growth rate then decays due to the transport of vorticity via Alfvén fronts. This results in interface amplitude asymptoting to a constant value, such that the difference between the initial and final interface amplitudes is inversely proportional to the magnetic field magnitude. Thus the instability of the interface is suppressed by the presence of the magnetic field.

The model developed in Chapter 3 differs from the full MHD Richtmyer-Meshkov instability in that it is incompressible, linear, and is driven by an impulse rather than by the impact of a shock wave. To assess the performance of this linear model, predictions from the model were compared to the results of impulse driven linearized (IDL), shock driven linearized (SDL), and non-linear (NL) compressible MHD simulations for a variety of cases. The performance of the linear model was first assessed for a baseline case for which the incident shock Mach number M, initial interface amplitude η_0, and non-dimensional strength of the applied magnetic field β^{-1} are small. For this case, the agreement between the linear model and the interface behavior from the IDL simulation is excellent, with the model predicting the final amplitude of the interface to within 0.2%. Compressible waves present are in the simulation that cause small amplitude, short period oscillations in the amplitude of the interface. These waves are not present in the linear model but do not effect the overall evolution of the interface as they have no vorticity associated with them. The agreement between the linear model and the SDL simulation is also good, while the final interface amplitude

from the NL simulation is over-predicted by 2.2%. For all simulations of this case, the linear model represents the flow structures that dominate the evolution of the interface with reasonable accuracy. In the shock driven simulations, the interface amplitude also exhibits a long period oscillation caused by the interaction of transverse waves downstream of the shocks and/or outgoing waves reflected from the shocks. When M is increased, the linear model still accurately predicts the behavior of the interface in the IDL simulation, but it increasingly overestimates the amplitude of the interface η in the shock driven cases. The amplitude of the long period oscillations in the shock driven simulations increases with M. As β^{-1} is increased, the linear model less accurately predicts the results of all simulations. The accuracy of the linear model was found to be severely compromised once the magnetic field is sufficiently strong that the Alfvén wave speed approaches the acoustic sound speed, particularly if the incident shock is weak. When this occurs, the features of the flow that dominate the evolution of the interface deviate significantly from the linear model. When η_0 is increased, the agreement between the model and the linearized simulations is unchanged. The degree to which the linear model over-predicts η from NL simulations gradually increases with η_0. Generally, the interface behavior given by the incompressible linear model developed in Chapter 3 well approximates that seen compressible linearized simulations when $M - 1$, η_0/λ, and β^{-1} are small. For such cases, the agreement with interface behavior observed in non-linear simulations is also reasonable. When $M - 1$, η_0/λ, and β^{-1} are increased, the linear model becomes less accurate. For strong shocks, large initial perturbation amplitudes, and strong magnetic fields, it appears that the linear model may give a rough estimate of the interface behavior, but it is not quantitatively accurate.

Samtaney (2003) has identified the change in the MHD shock refraction process with the application of a magnetic field as the mechanism by which the MHD RMI is suppressed. In hydrodynamics, a solution to the shock refraction problem was required in order for the analysis of the compressible RMI to be carried out (Richtmyer, 1960). A solution technique for the MHD shock refraction problem therefore seems essential to the analysis of the MHD RMI. In Chapter 5, an iterative procedure

was developed for determining the flow structure produced by the regular refraction of a MHD shock at an oblique planar density interface with a density ratio larger than unity. This solution technique was used to reproduce the quintuple-point structure observed in the numerical simulations of Samtaney (2003). The quintuple-point structure is similar to the hydrodynamic triple-point, but with the shocked contact replaced by two sub-fast shocks that bracket a MHD contact discontinuity, which is vorticity free. The features of this structure were studied in detail and there was shown to be excellent agreement between the results of the iterative procedure and the numerical results of Samtaney (2003). For Samtaney's conditions, one of the sub-fast shocks is a $2 \rightarrow 4$ intermediate shock. A second solution was computed in which the intermediate shock was replaced by a 180^o rotational discontinuity followed downstream by a slow shock. This is referred to as a regular solution while the quintuple-point structure involving the intermediate shock is referred to as being irregular. For the three-dimensional ideal MHD equations, all waves that appear in regular solutions are admissible under the evolutionary condition according to Falle and Komissarov (2001). While for the strongly planar ideal MHD equations, in which gradients and vectors are restricted to a plane (in some reference frame), all waves that appear in irregular solutions are admissible under the evolutionary condition. Regular and irregular solution branches corresponding to increasing β were traced for four sets of parameters. As β is increased, it was found that the two shocks bracketing the shocked contact undergo a number of transitions. Along each regular branch, the initial transitions are from slow shocks to 180^o rotational discontinuities followed downstream by slow shocks. As β is increased further, these transition to 180^o rotational discontinuities followed downstream by slow-mode expansion fans. Along each irregular solution branch, the transitions are from slow shocks to $2 \rightarrow 4$ intermediate shocks and finally to C_1 compound waves with increasing β. Once all transitions are complete, two possible flow structures that may arise from the shock refraction process were identified. These are an irregular quintuple-point solution consisting of a hydrodynamic shock, two fast shocks, and two C_1 compound waves, and a seven wave regular solution consisting of a hydrodynamic shock, two fast shocks, two 180^o

rotational discontinuities, and two slow-mode expansion fans, along with the contact discontinuity. The seven wave structure is denoted the septuple-point solution. The quintuple-point and septuple-point solutions remain valid up to the largest β values investigated using the iterative procedure.

In the hydrodynamic triple-point solution to a shock refraction problem, which occurs in MHD in the absence of a magnetic field, the shocked contact discontinuity is a vortex sheet. If, however, a magnetic field is present, even if it is vanishingly small in magnitude, the contact discontinuity cannot support a tangential velocity jump. This apparent paradox is addressed in Chapter 6, initially by applying the solution technique developed in Chapter 5 to cases in which the applied magnetic field is small. The results presented suggest that in the limit of infinite β, which corresponds to a vanishing applied magnetic field, both the quintuple-point and septuple-point solutions identified in Chapter 5 become identical to the hydrodynamic triple-point solution, with the exception that the shocked hydrodynamic contact is replaced by a singular structure we call the inner layer. The inner layer is a wedge bounded by either the two compound waves or the two rotational discontinuities followed by the two slow-mode expansion fans. These bracket an MHD contact discontinuity. In both cases, the angle of this wedge scales like $\beta^{-1/2}$, which is proportional to the applied magnetic field magnitude. A scaling for each of the variables within the inner layer is also suggested by the results of the calculations. Significantly, this scaling implies that the magnetic field within the inner layer is finite in the limit of β tending to infinity. In addition, the magnetic field is not parallel to the MHD contact, hence it cannot support a jump in tangential velocity. This necessitates the presence of the expansion fans (that are part of the compound waves in the quintuple-point solution), which support the tangential velocity discrepancy across the inner layer even though their angular extents tend to zero. To verify these findings, the equations governing the leading order asymptotic solution of the shock refraction problem, which is the large β limit of both the quintuple-point and septuple-point solutions, were derived and then solved iteratively. Finally. the asymptotic and full solutions were compared quantitatively and were found to be in excellent agreement.

Appendix A

Numerical method for ideal MHD equations

The non-linear simulations presented in this thesis were carried out using a method developed by Ravi Samtaney (Computational Plasma Physics Group, Princeton Plasma Physics Laboratory, Princeton University, NJ) for obtaining numerical solutions to the ideal MHD equations. For completeness, this numerical method is briefly described here.

A.1 Modified ideal MHD equations

The governing equations for the numerical method are the ideal MHD equations, which are presented in Section 2.2. These equations were simplified by assuming that the solenoidal property of the magnetic field holds. Following the arguments of Falle et al. (1998), if the solenoidal property of the magnetic field is violated numerically then an additional term, proportional to $\nabla \cdot \mathbf{B}$, should be included on the right-hand side of the *conservation* form of the equations. The resulting set of equations is

$$\frac{\partial U}{\partial t} + \frac{\partial F_j(U)}{\partial x_j} = S_{\nabla\cdot\mathbf{B}}, \tag{A.1}$$

where

$$S_{\nabla\cdot\mathbf{B}} = -\frac{\partial B_k}{\partial x_k} \left\{0\,,\, B_i\,,\, u_i,\, B_k u_k\right\}^T. \tag{A.2}$$

Powell et al. (1999b) have used these equations in their *eight-wave* approach, in which magnetic monopoles are advected along streamlines. Samtaney's approach is based on that of Powell, except that in his approach the source term makes no contribution to the final update of the conserved variables. Thus, Samtaney's approach leads to a conservative, solenoidal **B** method. The source term is, however, used in the predictor steps of the algorithm, which is described in the next section, as its inclusion is necessary to obtain second-order accuracy.

A.2 Multidimensional second-order Godunov method for MHD

In describing Samtaney's method, the following notation is adopted from the Chombo documentation. The underlying discretization of space is given as points $(i_0, ..., i_{\mathbf{D}-1}) = \boldsymbol{i} \in \mathbb{Z}^{\mathbf{D}}$, where $\mathbf{D}$ is the number of spatial dimensions. The problem domain is discretized using a grid $\Gamma \subset \mathbb{Z}^{\mathbf{D}}$. Γ is used to represent a cell-centered discretization of the continuous spatial domain into a collection of control volumes, which are defined as follows: $\boldsymbol{i} \in \Gamma$ represents a region of space $[\boldsymbol{x}_0 + (\boldsymbol{i} - \frac{1}{2}\boldsymbol{u})h, \boldsymbol{x}_0 + (\boldsymbol{i} + \frac{1}{2}\boldsymbol{u})h]$, where $\boldsymbol{x}_0 \in \mathbb{R}^{\mathbf{D}}$ is some fixed origin of coordinates, h is the mesh spacing, and $\boldsymbol{u} \in \mathbb{Z}^{\mathbf{D}}$ is the vector whose components are all equal to one. Various face-centered and node-centered discretizations of space can also be defined based on those control volumes. For example, $\Gamma^{\boldsymbol{v}}$ denotes the set of points in physical space of the form $\boldsymbol{x}_0 + (\boldsymbol{i} \pm \frac{1}{2}\boldsymbol{v})h, \boldsymbol{i} \in \Gamma$, where $\boldsymbol{v}$ is any vector whose components are equal to either zero or one.

Samtaney's approach is a spatially unsplit method of the type developed by Colella (1990b) and Saltzman (1994). The unsplit method was recently extended to MHD by Crockett et al. (2005). To describe this method, Eq. A.1 is first rewritten without the summation convention as,

$$\frac{\partial U}{\partial t} + \sum_{d=0}^{\mathbf{D}-1} \frac{\partial F^d}{\partial x^d} = S_{\nabla \cdot \mathbf{B}}.$$

Here, F^d is equivalent to F_{d+1} in the previous notation. Next, a vector of primitive variables $W \equiv W(U)$ is defined as,

$$W = \{\rho, u_i, B_i, p\,(\ or\ p_t\ )\}^T\,,$$

where $p_t = p + B_k B_k/2$ is the total pressure. The choice of total pressure is convenient for certain problems. The equations are then rewritten in quasilinear form in terms of W as,

$$\frac{\partial W}{\partial t} + \sum_{d=0}^{\mathbf{D}-1} \bar{A}^d(W)\ \frac{\partial W^d}{\partial x^d} = S'_{\nabla\cdot\mathbf{B}},$$

where,

$$\bar{A}^d = \nabla_U W \cdot \nabla_U F^d \cdot \nabla_W U,$$

and,

$$S'_{\nabla\cdot\mathbf{B}} = \nabla_U W \cdot S_{\nabla\cdot\mathbf{B}}.$$

For MHD, $\bar{A}^d$ is a singular matrix with an eigenvector degeneracy. Taking the source term $S'_{\nabla\cdot\mathbf{B}}$ to the left hand side of the above equation gives the quasilinear equation,

$$\frac{\partial W}{\partial t} + \sum_{d=0}^{\mathbf{D}-1} A^d(W)\ \frac{\partial W^d}{\partial x^d} = 0.$$

For example, $\bar{A}^0$ (the superscript 0 indicates the x direction) is given by,

$$\bar{A}^0 = \begin{bmatrix} u_x & \rho & 0 & 0 & 0 & 0 & 0 & 0 \\ 0 & u_x & 0 & 0 & -B_x/\rho & B_y/\rho & B_z/\rho & 1/\rho \\ 0 & 0 & u_x & 0 & -B_y/\rho & -B_x/\rho & 0 & 0 \\ 0 & 0 & 0 & u_x & -B_z/\rho & 0 & -B_x/\rho & 0 \\ 0 & 0 & 0 & 0 & 0 & 0 & 0 & 0 \\ 0 & B_y & -B_x & 0 & -u_z & u_x & 0 & 0 \\ 0 & B_x & 0 & -B_x & -u_\phi & 0 & u_x & 0 \\ 0 & \gamma p & 0 & 0 & (\gamma-1)\mathbf{B}\cdot\mathbf{u} & 0 & 0 & u_x \end{bmatrix}, \qquad \text{(A.3)}$$

while A^0 is given by

$$A^0 = \begin{bmatrix} u_x & \rho & 0 & 0 & 0 & 0 & 0 & 0 \\ 0 & u_x & 0 & 0 & 0 & B_y/\rho & B_z/\rho & 1/\rho \\ 0 & 0 & u_x & 0 & 0 & -B_x/\rho & 0 & 0 \\ 0 & 0 & 0 & u_x & 0 & 0 & -B_x/\rho & 0 \\ 0 & 0 & 0 & 0 & u_x & 0 & 0 & 0 \\ 0 & B_y & -B_x & 0 & 0 & u_x & 0 & 0 \\ 0 & B_z & 0 & -B_x & 0 & 0 & u_x & 0 \\ 0 & \gamma p & 0 & 0 & 0 & 0 & 0 & u_x \end{bmatrix}. \tag{A.4}$$

Now, given the discrete solution at time-step n, $U^n_{\boldsymbol{i}}$, second-order accurate estimates of the fluxes at the cell faces, $\boldsymbol{i}+\frac{1}{2}\boldsymbol{e}^d$, at time level $n+\frac{1}{2}$ must be computed in order to advance the solution. These are denoted $F^{n+\frac{1}{2}}_{\boldsymbol{i}+\frac{1}{2}\boldsymbol{e}^d} \approx F^d(\boldsymbol{x}_0+(\boldsymbol{i}+\frac{1}{2}\boldsymbol{e}^d)h, t^n+\frac{1}{2}\Delta t)$. Here, $\boldsymbol{e}^d$ is the unit vector spanning spatial dimension d. Note that the transformations $\nabla_U W$ and $\nabla_W U$ are functions of both space and time. Samtaney's method for advancing the solution with second order accuracy in time and space, while maintaining the solenoidal property of the magnetic field, consists of the following nine steps:

1. Transform $U^n_{\boldsymbol{i}}$ to primitive variables,

$$W^n_{\boldsymbol{i}} = W(U^n_{\boldsymbol{i}}),$$

   then compute the slopes $\Delta^d W_{\boldsymbol{i}}$ for $0 \le d < \mathbf{D}$.

2. Compute the effect of the normal derivative terms and the source term on the extrapolation in space and time from cell centers to faces. For $0 \le d < \mathbf{D}$,

$$W_{\boldsymbol{i},\pm,d} = W^n_{\boldsymbol{i}} + \frac{1}{2}(\pm I - \frac{\Delta t}{h} A^d_{\boldsymbol{i}}) P_\pm(\Delta^d W_{\boldsymbol{i}}), \tag{A.5}$$

   where,

$$A^d_{\boldsymbol{i}} = A^d(W_{\boldsymbol{i}})$$

and

$$P_{\pm}(W) = \sum_{\pm\lambda_k>0} (l_k \cdot W) r_k. \tag{A.6}$$

Here, λ_k are eigenvalues of $A^d_{\boldsymbol{i}}$, and l_k and r_k are the corresponding left and right eigenvectors (see Powell et al. (1999b) for expressions).

3. Compute estimates of F^d at the cell interfaces suitable for computing the one-dimensional flux derivatives $\frac{\partial F^d}{\partial x^d}$. The previous normal predictor step yields the left and right states at each cell interface. These are input to the eight-wave linearized Riemann solver of Powell et al. (1999b), which computes the primitive variables at the cell interface. The entire solution vector at $\boldsymbol{i} + \frac{1}{2}\boldsymbol{e}^d$ is termed the solution of the Riemann problem. The flux estimates are then computed from the primitive variables,

$$F^{\mathrm{1D}}_{\boldsymbol{i}+\frac{1}{2}\boldsymbol{e}^d} \equiv F(W^{\mathrm{1D}}_{\boldsymbol{i}+\frac{1}{2}\boldsymbol{e}^d}) \tag{A.7}$$

where,

$$W^{\mathrm{1D}}_{\boldsymbol{i}+\frac{1}{2}\boldsymbol{e}^d} \equiv R(W_{\boldsymbol{i},+,d}, W_{\boldsymbol{i}+\boldsymbol{e}^d,-,d}).$$

Here, R represents the Riemann solver.

4. In 3D, compute corrections to $W_{\boldsymbol{i},\pm,d}$ corresponding to one set of transverse derivatives appropriate to obtain $(1,1,1)$ diagonal coupling. This step is not carried out in 2D. The corrections are computed as follows:

$$W_{\boldsymbol{i},\pm,d_1,d_2} = W_{\boldsymbol{i},\pm,d_1} - \frac{\Delta t}{3h} \nabla_U W \cdot (F^{\mathrm{1D}}_{\boldsymbol{i}+\frac{1}{2}\boldsymbol{e}^{d_2}} - F^{\mathrm{1D}}_{\boldsymbol{i}-\frac{1}{2}\boldsymbol{e}^{d_2}}). \tag{A.8}$$

In addition, the magnetic field arising from the solution of the Riemann problem is generally not solenoidal. Thus the following nonconservative source term is also added to $W_{\boldsymbol{i},\pm,d_1,d_2}$:

$$-\frac{\Delta t}{3h} \nabla_U W \cdot (B^{d_2}_{\boldsymbol{i}+\frac{1}{2}\boldsymbol{e}^{d_2}} - B^{d_2}_{\boldsymbol{i}-\frac{1}{2}\boldsymbol{e}^{d_2}}) a_{\boldsymbol{i},d_2}. \tag{A.9}$$

Here, $a_{\boldsymbol{i},d_2} = \{0, B_k, u_k, u_k B_k\}^T$ where each entry is computed as the average of the values at $\boldsymbol{i} + \frac{1}{2}\boldsymbol{e}^{d_2}$ and $\boldsymbol{i} - \frac{1}{2}\boldsymbol{e}^{d_2}$.

5. In 3D, compute the fluxes corresponding to the corrected $W_{\boldsymbol{i},\pm,d_1,d_2}$ calculated in the previous step. This is done using,

$$F_{\boldsymbol{i}+\frac{1}{2}\boldsymbol{e}^{d_1},d_2} = R(W_{\boldsymbol{i},+,d_1,d_2}, W_{\boldsymbol{i}+\boldsymbol{e}^{d_1},-,d_1,d_2}, d_1), \tag{A.10}$$

$$d_1 \neq d_2,\ 0 \leq d_1, d_2 < \mathbf{D}.$$

6. Compute the final corrections to $W_{\boldsymbol{i},\pm,d}$ due to the remaining transverse derivatives using,

$$\text{2D:}\quad W^{n+\frac{1}{2}}_{\boldsymbol{i},\pm,d} = W_{\boldsymbol{i},\pm,d} - \frac{\Delta t}{2h}\nabla_U W \cdot (F^{\text{1D}}_{\boldsymbol{i}+\frac{1}{2}\boldsymbol{e}^{d_1}} - F^{\text{1D}}_{\boldsymbol{i}-\frac{1}{2}\boldsymbol{e}^{d_1}}) \tag{A.11}$$

$$d \neq d_1,\ 0 \leq d, d_1 < \mathbf{D}$$

$$\begin{aligned}\text{3D:}\quad W^{n+\frac{1}{2}}_{\boldsymbol{i},\pm,d} = W_{\boldsymbol{i},\pm,d} &- \frac{\Delta t}{2h}\nabla_U W \cdot (F_{\boldsymbol{i}+\frac{1}{2}\boldsymbol{e}^{d_1},d_2} - F_{\boldsymbol{i}-\frac{1}{2}\boldsymbol{e}^{d_1},d_2}) \\ &- \frac{\Delta t}{2h}\nabla_U W \cdot (F_{\boldsymbol{i}+\frac{1}{2}\boldsymbol{e}^{d_2},d_1} - F_{\boldsymbol{i}-\frac{1}{2}\boldsymbol{e}^{d_2},d_1})\end{aligned} \tag{A.12}$$

$$d \neq d_1 \neq d_2,\ 0 \leq d, d_1, d_2 < \mathbf{D}.$$

The corresponding nonconservative source terms are then added to the corrected values as follows:

$$\text{2D:}\quad W^{n+\frac{1}{2}}_{\boldsymbol{i},\pm,d} = W^{n+\frac{1}{2}}_{\boldsymbol{i},\pm,d} - \frac{\Delta t}{2h}\nabla_U W \cdot (B^{d_1}_{\boldsymbol{i}+\frac{1}{2}\boldsymbol{e}^{d_1}} - B^{d_1}_{\boldsymbol{i}-\frac{1}{2}\boldsymbol{e}^{d_1}})a_{\boldsymbol{i},d_1} \tag{A.13}$$

$$d \neq d_1,\ 0 \leq d, d_1 < \mathbf{D}$$

$$\begin{aligned}\text{3D:}\quad W^{n+\frac{1}{2}}_{\boldsymbol{i},\pm,d} = W_{\boldsymbol{i},\pm,d} &- \frac{\Delta t}{2h}\nabla_U W \cdot (B^{d_1}_{\boldsymbol{i}+\frac{1}{2}\boldsymbol{e}^{d_1},d^2} - B^{d_1}_{\boldsymbol{i}-\frac{1}{2}\boldsymbol{e}^{d_1},d^2})a_{\boldsymbol{i},d_1} \\ &- \frac{\Delta t}{2h}\nabla_U W \cdot (B^{d_2}_{\boldsymbol{i}+\frac{1}{2}\boldsymbol{e}^{d_2},d^1} - B^{d_2}_{\boldsymbol{i}-\frac{1}{2}\boldsymbol{e}^{d_2},d^1})a_{\boldsymbol{i},d_2}\end{aligned} \tag{A.14}$$

$$d \neq d_1 \neq d_2,\ 0 \leq d, d_1, d_2 < \mathbf{D}.$$

Note that convergence tests on linear wave propagation indicate that second-

order accuracy is not obtained unless the terms corresponding to contributions of $S_{\nabla\cdot\mathbf{B}}$ are included in the transverse predictors above.

7. Compute the final estimate of fluxes by first re-evaluating the primitive variables at the cell faces using,

$$W^{n+\frac{1}{2}}_{\boldsymbol{i}+\frac{1}{2}\boldsymbol{e}^d} = R(W^{n+\frac{1}{2}}_{\boldsymbol{i},+,d}, W^{n+\frac{1}{2}}_{\boldsymbol{i}+\boldsymbol{e}^d,-,d}, d). \tag{A.15}$$

The normal component of the magnetic field at $\boldsymbol{i} + \frac{1}{2}\boldsymbol{e}^d$ is then used to compute a cell centered divergence. The following Poisson equation,

$$\nabla^2\phi = \sum_{d=0}^{\mathbf{D}-1} \frac{\partial B^d}{\partial x^d}_{\boldsymbol{i}}, \tag{A.16}$$

is then solved using a multi-grid technique with a Gauss-Seidel Red-Black ordering smoother. The normal component of the magnetic field at the faces is then corrected as follows:

$$B^d_{\boldsymbol{i}\frac{1}{2}\boldsymbol{e}^d} = B^d_{\boldsymbol{i}\frac{1}{2}\boldsymbol{e}^d} - \frac{(\phi_{\boldsymbol{i}+\boldsymbol{e}^d} - \phi_{\boldsymbol{i}})}{h}. \tag{A.17}$$

The corrected magnetic field is then substituted into $W^{n+\frac{1}{2}}_{\boldsymbol{i}+\frac{1}{2}\boldsymbol{e}^d}$, which is used to compute the final estimate of the fluxes, $F^{n+\frac{1}{2}}_{\boldsymbol{i}+\frac{1}{2}\boldsymbol{e}^d} = F(W^{n+\frac{1}{2}}_{\boldsymbol{i}+\frac{1}{2}\boldsymbol{e}^d})$.

8. Update the conserved variables using the divergence of the fluxes as follows:

$$U^{n+1}_{\boldsymbol{i}} = U^n_{\boldsymbol{i}} - \frac{\Delta t}{h}\sum_{d=0}^{\mathbf{D}-1}(F^{n+\frac{1}{2}}_{\boldsymbol{i}+\frac{1}{2}\boldsymbol{e}^d} - F^{n+\frac{1}{2}}_{\boldsymbol{i}-\frac{1}{2}\boldsymbol{e}^d}). \tag{A.18}$$

9. Perform a centered constrained transport step. The formulation used for this step is the one prescribed by Toth (2000). This step removes divergence modes with the following finite difference representation:

$$\nabla\cdot\mathbf{B}_{\boldsymbol{i}} = \frac{1}{2h}\sum_{d=0}^{\mathbf{D}-1}(B^d_{\boldsymbol{i}+\boldsymbol{e}^d} - B^d_{\boldsymbol{i}-\boldsymbol{e}^d}) + O(h^2). \tag{A.19}$$

The electric field is evaluated using a centered approximation in time,

$$\mathbf{E}_{\boldsymbol{i}} = \frac{1}{2}\left((\mathbf{u}\times\mathbf{B})_{\boldsymbol{i}}^{\mathbf{n+1}} + (\mathbf{u}\times\mathbf{B})_{\boldsymbol{i}}^{\mathbf{n}}\right), \tag{A.20}$$

and then each component of the magnetic field is corrected as follows:

$$B_{\boldsymbol{i}}^{d,n+1} = B_{\boldsymbol{i}}^{d,n} - \varepsilon_{d,d_1,d_2}\,\frac{\Delta t}{2h}\left(E^{d_2}_{\boldsymbol{i}+\boldsymbol{e}^{d_1}} - E^{d_2}_{\boldsymbol{i}-\boldsymbol{e}^{d_1}} + E^{d_1}_{\boldsymbol{i}+\boldsymbol{e}^{d_2}} - E^{d_1}_{\boldsymbol{i}-\boldsymbol{e}^{d_1}}\right). \tag{A.21}$$

Appendix B

Numerical method for linearized simulations

The linearized simulations presented in this thesis were carried out using a method developed by Samtaney (2004) for obtaining numerical solutions to the linearized MHD equations when the base flow is temporally evolving. For completeness, this method is briefly described here. First, the equations of compressible ideal MHD are written in conservative form in two dimensions as follows;

$$\frac{\partial U}{\partial t} + \frac{\partial F(U)}{\partial x} + \frac{\partial H(U)}{\partial z} = 0, \tag{B.1}$$

where the solution vector $U \equiv U(x, z, t)$ is,

$$U = \{\rho, \rho u, \rho v, \rho w, B_x, B_y, B_z, \rho e_T\}^T, \tag{B.2}$$

and the vectors $F(U)$ and $H(U)$ are given by,

$$\begin{aligned} F(U) &= \left\{\rho u, \rho u^2 + p_t - B_x^2, \rho uv, \rho uw - B_x B_z, 0, uB_y - vB_x, uB_z - wB_x,\right. \\ &\quad \left.(\rho e_T + p_t)u - B_x(B_x u + B_y v + B_z w)\right\}^T, \\ H(U) &= \left\{\rho w, \rho uw - B_x B_z, \rho vw - B_y B_z, \rho w^2 + p_t - B_z^2, wB_x - uB_z, wB_y - vB_z, 0,\right. \\ &\quad \left.(\rho e_T + p_t)w - B_z(B_x u + B_y v + B_z w)\right\}^T. \end{aligned} \tag{B.3}$$

These are the fluxes of mass, momentum, magnetic field, and total energy in the x and z directions, respectively. In the above equations, ρ is the density, u, v and w are the velocity components, B_x, B_y and B_z are the components of the magnetic field, ρe_T is the total energy per unit volume, and $p_t \equiv p + B^2/2$ is the sum of the gas pressure and the magnetic pressure. Next, the solution is written as,

$$U(x, z, t) = U^o(z, t) + \epsilon\, \hat{U}(z, t) \exp(ikx),$$

where $\epsilon \ll 1$, $U^o(z, t)$ is a one-dimensional temporally evolving base flow, and $\epsilon\hat{U}(z, t) \exp(ikx)$ is the perturbation to the base flow. Substituting this form for $U(x, z, t)$ into (B.1) then collecting terms of $O(1)$ and $O(\epsilon)$, respectively, we obtain,

$$\frac{\partial U^o}{\partial t} + \frac{\partial H(U^o)}{\partial z} = 0, \tag{B.4}$$

$$\frac{\partial \hat{U}}{\partial t} + \frac{\partial A(U^o)\hat{U}}{\partial z} = ikB(U^o)\hat{U}, \tag{B.5}$$

where $B(U^o)$ is the Jacobian of $F(U^o)$ with respect to U^o. Equation (B.4) governs the evolution of the base flow, while the evolution of the perturbations is governed by (B.5). This is a system of coupled linear wave equations in which the wave speeds are given by the eigenvalues of $A(U^o)$, the Jacobian of the $H(U^o)$ with respect to U^o.

A finite volume upwind approach is adopted to solve for both the base flow and the perturbations. The domain is discretized into finite volumes of uniform size Δz, whose centers have index j and faces have indices $j \pm \frac{1}{2}$. Equations (B.4) and (B.5) are written in a semi-discrete fashion as,

$$\frac{\partial U^o_j}{\partial t} = -\frac{H_{j+\frac{1}{2}} - H_{j-\frac{1}{2}}}{\Delta z}, \tag{B.6}$$

$$\frac{\partial \hat{U}_j}{\partial t} = -\frac{H'_{j+\frac{1}{2}} - H'_{j-\frac{1}{2}}}{\Delta z} + ikB(U^o_j)\hat{U}_j, \tag{B.7}$$

and integrated in time using a third-order TVD Runge-Kutta scheme. The fluxes

$H_{j+\frac{1}{2}}$ and $H'_{j+\frac{1}{2}}$ are evaluated using Roe's method as follows;

$$H_{j+\frac{1}{2}} = \frac{1}{2}\left\{ H(U^o_j) + H(U^o_{j+1}) - \sum_k R_k|\lambda_k|L_k(U^o_{j+1} - U^o_j) \right\}, \tag{B.8}$$

$$H'_{j+\frac{1}{2}} = \frac{1}{2}\left\{ A(U^o_j)\hat{U}_j + A(U^o_{j+1})\hat{U}_{j+1} - [A^+(U^o_{j+\frac{1}{2}}) - A^-(U^o_{j+\frac{1}{2}})](\hat{U}_{j+1} - \hat{U}_j) \right\}, \tag{B.9}$$

where λ_k and L_k (R_k) are the eigenvalues and left (right) eigenvectors of $A(U^o_j)$, respectively. The matrices $A^{\pm}(U^o)$ are defined as $A^{\pm}(U^o) = R\Omega^{\pm}L$, where $\Omega^{\pm}$ is a diagonal matrix whose entries are $\pm\frac{1}{2}(|\lambda_k| + \lambda_k)$. These are evaluated at the cell faces using the state $U^o_{j+\frac{1}{2}}$, which is the algebraic mean of U^o_j and U^o_{j+1}.

Appendix C

The MHD Rankine-Hugoniot relations

Solutions to the MHD RH relations can be found as follows. It can then be shown that Eqs. 5.6-5.9 reduce to the following algebraic equation in r and b obtained by Liberman and Velikhovich (1986):

$$F(r,b) = Ar^2 + Br + C = 0 \ , \tag{C.1}$$

where

$$A = -\frac{1}{2}\frac{\gamma+1}{\gamma-1} \ , \quad B = \frac{1}{(\gamma-1)M_{S1}^2} + \frac{\gamma}{(\gamma-1)}\left(1 - \frac{b^2 - \sin^2\theta_1}{2M_{A1}^2}\right) \ , \tag{C.2}$$

$$C = -\frac{1}{2} - \frac{1}{(\gamma-1)M_{S1}^2} + \frac{b^2 - \sin^2\theta_1 - Y\left(b - \sin\theta_1\right)^2}{2M_{A1}^2} \ , \quad Y = 1 - \frac{1}{M_{I1}^2} \ . \tag{C.3}$$

The relation $F(r,b) = 0$ defines a curve in (r,b) space on which the fluxes of mass, momentum, and energy are equal to those upstream of the shock. The final jump condition can be expressed as

$$Z(r,b) = bX - Y\sin\theta_1 = 0 \ , \tag{C.4}$$

where

$$X = r - \frac{1}{M_{I1}^2} \ . \tag{C.5}$$

The intersections of the curves defined by $F = 0$ and $Z = 0$ are the locations in (r, b) space where all jump conditions are satisfied. The two equations $F = 0$ and $Z = 0$ are combined into a quartic equation in r, which is then divided by the known factor $(r - 1)$ to yield the cubic

$$\mathcal{R}(r) = \mathcal{A}r^3 + \mathcal{B}r^2 + \mathcal{C}r + \mathcal{D} = 0 \ , \tag{C.6}$$

where

$$\begin{aligned}
\mathcal{A} &= \frac{\gamma+1}{\gamma-1} \ , \\
\mathcal{B} &= -1 - \frac{2}{(\gamma-1)\,{M_{S1}}^2} - \frac{2\,(\gamma+1)\cos^2(\theta_1) + \gamma\sin^2(\theta_1)}{(\gamma-1)\,{M_{A1}}^2} \ , \\
\mathcal{C} &= \frac{(\gamma+1)\,{M_{S1}}^2 + \left[4 + {M_{S1}}^2\,(3\gamma-4)\right]{M_{A1}}^2 + \left[(\gamma+1)\,{M_{S1}}^2 + \left(4 + {M_{S1}}^2\gamma\right){M_{A1}}^2\right]\cos(2\theta_1)}{2\,(\gamma-1)\,{M_{A1}}^4{M_{S1}}^2} \ , \\
\mathcal{D} &= -\frac{\left[1 + (\gamma-1)\,{M_{S1}}^2 + \cos(2\theta_1)\right]\cos^2(\theta_1)}{(\gamma-1)\,{M_{A1}}^4{M_{S1}}^2} \ .
\end{aligned}$$

In terms of these coefficients, the roots of the cubic, referred to hereafter as roots A, B and C, can be expressed as

$$r_A = \frac{1}{6\,\mathcal{A}}\left[-2\,\mathcal{B} + J + H\right] \ , \tag{C.7}$$

$$r_B = \frac{1}{12\,\mathcal{A}}\left[-4\,\mathcal{B} - (H+J) + \sqrt{3}\,i\,(H-J)\right] \ , \tag{C.8}$$

$$r_C = \frac{1}{12\,\mathcal{A}}\left[-4\,\mathcal{B} - (H+J) - \sqrt{3}\,i\,(H-J)\right] \ , \tag{C.9}$$

where

$$\begin{aligned}
H &= 2^{2/3}\left(-N + \sqrt{-4\left(\mathcal{B}^2 - 3\,\mathcal{A}\,\mathcal{C}\right)^3 + N^2}\right)^{1/3} \ , \\
J &= 4\left(\mathcal{B}^2 - 3\,\mathcal{A}\,\mathcal{C}\right)/H \ , \\
N &= 2\,\mathcal{B}^3 - 9\,\mathcal{A}\,\mathcal{B}\,\mathcal{C} + 27\,\mathcal{A}^2\,\mathcal{D} \ .
\end{aligned}$$

Once r has been computed from the upstream state using Eq. C.7, Eq. C.8, or Eq. C.9, the complete downstream state ($\rho_2,\ p_2,\ \mathbf{M}_{S2},\ \beta_2,\ \theta_2$) can be readily computed. First b is computed using Eq. C.4. An expression for the downstream pressure in terms of r and b can be found by manipulating Eq. 5.7 into

$$f_p(r,b) \equiv \frac{p_2}{p_1} = 1 + \gamma M_{S1}^2 \left(1 - r - \frac{b^2 - \sin^2(\theta_1)}{2M_{A1}^2}\right) \ . \tag{C.10}$$

The normal component of the downstream Mach number is then simply obtained using

$$M_{S2n} = \sqrt{\frac{r}{f_p(r,b)}} M_{S1n} \ , \tag{C.11}$$

while the tangential component is obtained by manipulating Eq. 5.8 into

$$M_{S2t} = \sqrt{\frac{1}{r\ f_p(r,b)}} \left(M_{S1t} + M_{S1n} \frac{(b - \sin\theta_1)\cos\theta_1}{M_{A1}^2}\right) \ . \tag{C.12}$$

Finally, β_2 and θ_2 are readily obtained using the definition of b and the fact that B_n is continuous across a shock;

$$\beta_2 = \frac{1}{b^2 + \cos^2(\theta_1)} f_p(r,b)\ \beta_1 \ , \tag{C.13}$$

$$\sin\theta_2 = \frac{b}{\sqrt{b^2 + \cos^2(\theta_1)}} \ . \tag{C.14}$$

Appendix D

Governing equations for a MHD expansion fan

The basic equations governing the flow through a centered, steady MHD expansion fan can be obtained by writing Eqs. 5.1-5.2 and Eqs. 5.4-5.5 in cylindrical co-ordinates, then assuming variations occur only with the polar angle φ (Yang and Sonnerup, 1976, Krisko and Hill, 1991). Further, the flow is assumed to be isentropic; hence the energy equation is replaced by an entropy equation. Under these assumptions the governing equations become

$$\rho\ u_t + \rho\ \partial_\varphi u_n + u_n\ \partial_\varphi \rho = 0\ , \tag{D.1}$$

$$u_t\ u_n + u_n\ \partial_\varphi u_n + \partial_\varphi p/\rho - B_t\ B_n/\mu_0\rho + B_t\ \partial_\varphi B_t/\mu_0\rho = 0\ , \tag{D.2}$$

$$u_n^2 - u_n\ \partial_\varphi u_t - B_n^2/\mu_0\rho + B_n\ \partial_\varphi B_t/\mu_0\rho = 0\ , \tag{D.3}$$

$$\partial_\varphi p/p - \gamma\ \partial_\varphi \rho/\rho = 0\ , \tag{D.4}$$

$$B_t + \partial_\varphi B_n = 0\ , \tag{D.5}$$

$$B_t\ \partial_\varphi u_n + u_n\ \partial_\varphi B_t - B_n\ \partial_\varphi u_t - u_t\ \partial_\varphi B_n = 0\ , \tag{D.6}$$

where $\partial_\varphi \equiv \partial/\partial\varphi$, and the subscripts n and t denote vector components in the φ and r directions respectively. Eqs. D.1-D.6 form a system for $\partial_\varphi\rho$, $\partial_\varphi p$, $\partial_\varphi u_t$, $\partial_\varphi u_n$, $\partial_\varphi B_t$, and $\partial_\varphi B_n$. It can be shown that if the determinant of the system is non-zero, only the trivial solution of uniform flow is admissible. Thus, for a MHD expansion fan to

be a valid solution, the system must be singular, which requires

$$\frac{u_n^4}{p} - \frac{u_n^2}{\rho}\left(\gamma + \frac{B_n^2}{\mu_0 p} + \frac{B_t^2}{\mu_0 p}\right) + \frac{\gamma B_n^2}{\mu_0 \rho^2} = 0 \ . \tag{D.7}$$

We introduce the following non-dimensional vector to represent the magnetic field:

$$\mathbf{K} \equiv \frac{\mathbf{B}}{\sqrt{2\mu_0 p}} \ . \tag{D.8}$$

After non-dimensionalization, Eqs. D.1-D.6 can be combined to form the following set of differential equations from which pressure has been eliminated (Yang and Sonnerup, 1976):

$$\partial_\varphi M_n = -\frac{(\gamma+1)}{2} M_n \frac{\partial_\varphi \rho}{\rho} - M_t \ , \tag{D.9}$$

$$\partial_\varphi M_t = \left(-\frac{K_t\ M_n}{K_n\ M_t} + \frac{1-\gamma}{2} + \frac{\gamma\ M_n \left({M_n}^2 - 1\right)}{2\ K_n\ K_t\ M_t}\right) M_t \frac{\partial_\varphi \rho}{\rho} + M_n \ , \tag{D.10}$$

$$\partial_\varphi K_n = -\frac{\gamma\ K_n}{2}\frac{\partial_\varphi \rho}{\rho} - K_t \ , \tag{D.11}$$

$$\partial_\varphi K_t = \frac{\gamma}{2}\left(\frac{{M_n}^2}{{K_t}^2} - 1 - {K_t}^{-2}\right) K_t \frac{\partial_\varphi \rho}{\rho} + K_n \ . \tag{D.12}$$

Here, M denotes the sonic Mach number. By combining the derivative of Eq. D.7,

$$\partial_\varphi \left(M_n^4 - M_n^2\left[1 + \frac{2}{\gamma}(K_n^2 + K_t^2)\right] + \frac{2}{\gamma}K_n^2\right) = 0 \ ,$$

with Eqs. D.9)-D.12, we obtain

$$\frac{\partial_\varphi \rho}{\rho} = \frac{4\ {M_n}^3\ M_t - 2\ M_n\ M_t\left[1 + \frac{2}{\gamma}\left({K_n}^2 + {K_t}^2\right)\right] + \frac{4}{\gamma}K_n\ K_t}{-2\ {K_n}^2 - 2\,(2+\gamma)\,{M_n}^4 + {M_n}^2\left[3 + \left(4 + \frac{2}{\gamma}\right)\left({K_n}^2 + {K_t}^2\right) + \gamma\right]} \ . \tag{D.13}$$

The complete solution throughout the expansion fan can be found by numerically integrating Eqs. D.9-D.13 with respect to φ, then using the isentropic relation to recover the pressure. The domain of integration begins at the leading wavelet of the expansion fan. This wavelet propagates at either the fast or slow MHD characteristic

speed with respect to the upstream flow, depending on whether we are considering a fast- or a slow-mode expansion fan. Thus, the angle of the leading wavelet to the upstream velocity vector, φ, must satisfy

$$M_{Fn/SLn}\left(\varphi_{F/SL}\right) = 0 \ . \tag{D.14}$$

Appendix E

Governing equations for a slow compound wave

For certain shock solutions to the MHD RH relations, it is possible for rarefaction waves to move with the shocks. This can occur for shocks that propagate at the fast characteristic speed and for shocks where the downstream normal flow speed relative to the shock is the slow characteristic speed. When a rarefaction travels immediately upstream or downstream of one of these shocks, the combination is referred to as a *compound wave*. In the context of MHD, these waves were first identified in numerical solutions to the full MHD equations by Wu (1987). In the strongly planar MHD system, Myong and Roe (1997) recommend the use of compound waves as a substitute for $2 \rightarrow 3$ intermediate shocks, which are inadmissible under their viscosity admissibility condition and the evolutionary condition.

The compound wave relevant to this study consists of a $2 \rightarrow 3 = 4$ intermediate shock, for which $u_{n2} = C_{SL2}$, followed immediately downstream by a slow-mode expansion fan. This is the steady two-dimensional analogue of the unsteady one-dimensional slow compound wave referred to as C_1 by Myong and Roe (1997). We will use the same designation for the two-dimensional compound wave.

For a $2 \rightarrow 3 = 4$ intermediate shock to occur, roots B and C of the RH relations must be equal. Comparing Eq. C.8 and Eq. C.9, it is apparent that this implies

$H = J$. In terms of the coefficients of Eq. C.6, this can be expressed as

$$\mathcal{D} = \frac{-2\,\mathcal{B}^3 + 9\,\mathcal{A}\,\mathcal{B}\,\mathcal{C} - 2\,\mathcal{B}^2\sqrt{\mathcal{B}^2 - 3\,\mathcal{A}\,\mathcal{C}} + 6\,\mathcal{A}\,\mathcal{C}\sqrt{\mathcal{B}^2 - 3\,\mathcal{A}\,\mathcal{C}}}{27\,\mathcal{A}^2}\,. \tag{E.1}$$

This relationship must be satisfied by the upstream flow state in order for a C_1 compound wave to be possible. The flow state downstream of a compound wave is computed as follows: As $H = J$ for a $2 \rightarrow 3 = 4$ intermediate shock, the following simplified relationship can be used to compute r:

$$r_{B/C} = -\frac{1}{6\,\mathcal{A}}\left(2\,\mathcal{B} + \,H\right)\,. \tag{E.2}$$

After b is computed using Eq. C.4, the remainder of the flow state downstream of the shock may be computed using Eqs. C.10-C.14. Using this flow state as initial data, the conditions downstream of the compound wave are then found by integrating Eqs. D.9-D.13 across the expansion fan portion of the wave.

Appendix F

Matching conditions at the contact discontinuity

The conditions on either side of the shocked contact discontinuity (SC) are computed as follows. First, the conditions upstream of shocks I (denoted with a subscript 0) and TF (denoted with a subscript b) in the reference frame where the intersection point is stationary are computed from the problem parameters using

$$\begin{aligned} \mathbf{U}_0 &= (1,\ 1,\ M,\ -M\tan\alpha,\ \beta,\ \pi)\ , \\ \mathbf{U}_b &= \left(\eta,\ 1,\ \sqrt{\eta}\frac{\cos(\frac{\pi}{2}-\phi_3+\alpha)}{\cos\alpha}M,\ \sqrt{\eta}\frac{\sin(\frac{\pi}{2}-\phi_3+\alpha)}{\cos\alpha}M,\ \beta,\ -\frac{\pi}{2}-\phi_3\right)\ , \end{aligned}$$

where $\mathbf{U} \equiv (\rho,\ p,\ M_{Sn},\ M_{St},\ \beta,\ \theta)$ and ϕ_3 is the angle between shock TF and the negative x-axis, as indicated in Figure 5.4, which shows how the various angles and regions of uniform flow in the problem are designated. θ and the normal and tangential vector components in $\mathbf{U}$ are defined with respect to the wave at the downstream boundary of a region.

Next, the conditions downstream of shock I (state 1) are computed. This is done by first computing the normal velocity ratio r_0 across shock I using the appropriate root of the RH relations, root A, B, or C. The specifics of which root is appropriate for each of the shocks for a given set of problem parameters will be discussed in Sections 5.4 and 5.5. Once $r_0 = \rho_1^{-1}$ is determined, the remainder of state 1 is computed using Eqs. C.4 and C.10-C.14.

In order to compute the conditions across shock RF, the components of $\mathbf{M}_{S1}$ normal and tangential to it are computed using

$$\begin{aligned} M'_{Sn} &= M_{Sn}\cos\Delta\phi - M_{St}\sin\Delta\phi \ , \\ M'_{St} &= M_{Sn}\sin\Delta\phi + M_{St}\cos\Delta\phi \ , \end{aligned} \tag{F.1}$$

where the unprimed and primed quantities are defined with respect to upstream and downstream waves, respectively, and $\Delta\phi$ is the angle between the two waves. The vector representing the magnetic field is redefined in the same manner. State 2 downstream of shock RF can then be computed using the RH relations, as for state 1.

If RS is a shock, the procedure used to compute state 2 is repeated to compute state 3 downstream of shock RS. It will be shown in Sections 5.4 and 5.5 that, in some instances, shock RS and/or shock TS is replaced by either a C_1 compound wave, a 180^o rotational discontinuity (RD) followed by a slow shock, or a RD followed by a slow-mode expansion fan. Assuming that RS is a C_1 compound wave, the angle between its leading edge and shock RF ($\Delta\phi_c$) must be calculated. This is done by expressing the coefficients in Eq. E.1 in terms of state 2 and $\Delta\phi_c$, then solving this relation numerically. Once $\Delta\phi_c$ is known, Eqs. F.1 are used to compute the vector components normal and tangential to the leading edge of the compound wave. The procedure outlined in Appendix E is then used to compute the flow state downstream of the compound wave. These are the conditions to the left of the SC and are referred to as state 3. If, instead, we assume that the RS wave-group begins with a RD, an intermediate state denoted with a subscript d must be calculated downstream of the RD. This is done by first calculating the angle between the RD and shock RF, $\Delta\phi_d$. Utilizing the fact that the rotational discontinuity propagates at the upstream intermediate characteristic speed with respect to the flow, it can be shown that

$$\Delta\phi_d = \arctan\left(\frac{\sqrt{2/\gamma}K_{2n} - M_{S2n}}{\sqrt{2/\gamma}K_{2t} - M_{S2t}}\right) \ , \tag{F.2}$$

where the subscripts n and t refer to vector components normal and tangential to shock RF. Once $\Delta\phi_d$ is known, Eqs. F.1 are used to compute the vector components normal and tangential to the RD. State d is then determined from the RH relations, making use of the fact that for a 180^o RD, $r = 1$ and $b = -\sin\theta_1$. If the remainder of the RS wave-group is a slow shock, the procedure used to compute state 2 is repeated to compute state 3. Alternatively, if the RS wave-group concludes with a slow-mode expansion fan, the next step is to compute the location of the leading wavelet of the fan ϕ_{f1} by solving Eq. D.14. Eqs. D.9)-D.13 are then integrated numerically from ϕ_{f1} to the angle of the last wavelet using state d as the initial conditions. This yields the conditions to the left of the SC.

The conditions to the right of the SC (state 5) are determined using an analogous procedure. For the proposed wave configuration to be a valid solution of the equations of ideal MHD, states 3 and 5 must satisfy matching conditions Eqs. 5.11-5.15.

Appendix G

Equivalence of leading order asymptotic quintuple and septuple-point solutions

We present the following argument that the leading order asymptotic solution to the shock refraction problem is the large β limit of both the quintuple-point and septuple-point solutions; upstream of the $2 \rightarrow 3 = 4$ intermediate shocks in the quintuple-point solution and the RDs in the septuple-point solution, our results indicate that the primitive variables can be expressed as

$$\begin{aligned}
\rho(\phi;\, \varepsilon) &= \rho^{(0)}(\phi) + \varepsilon\rho^{(1)}(\phi) + O(\varepsilon^2)\,, \\
p(\phi;\, \varepsilon) &= p^{(0)}(\phi) + \varepsilon p^{(1)}(\phi) + O(\varepsilon^2)\,, \\
u_n(\phi;\, \varepsilon) &= \varepsilon u_n^{(1)}(\phi) + O(\varepsilon^2)\,, \\
u_t(\phi;\, \varepsilon) &= u_t^{(0)}(\phi) + \varepsilon u_t^{(1)}(\phi) + O(\varepsilon^2)\,, \\
\mathbf{B}(\phi;\, \varepsilon) &= \varepsilon \mathbf{B}^{(1)}(\phi) + O(\varepsilon^2)\,.
\end{aligned}$$

Substituting these expansions into the RH relations and collecting terms of the same order, it can be shown that $\rho^{(0)}$, $p^{(0)}$, $u_n^{(1)}$, $u_t^{(0)}$, and $B_n^{(1)}$ are constant across both the $2 \rightarrow 3 = 4$ intermediate shocks and RDs in our solutions for small ε. Thus, these discontinuities do not affect the boundary conditions for Eqs. 6.6-6.10 and are omitted from the leading order solution. From Figure G.1, it can be seen that the difference between the locations of the leading expansion fan wavelets in the two solutions is

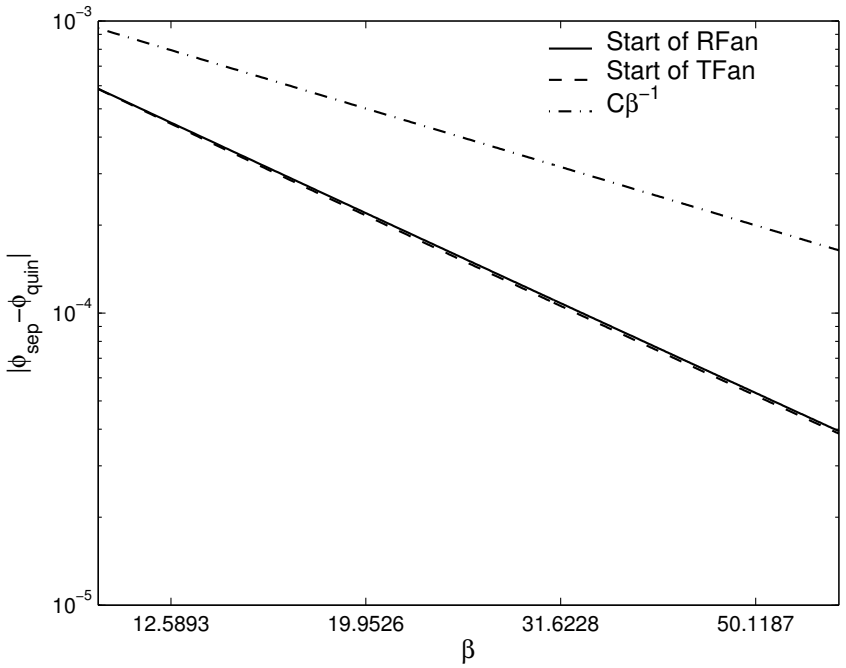

Figure G.1: Difference between the locations of the leading expansion fan wavelets of $RFan$ and $TFan$ in the two solutions along Branches Ic (subscript quin) and Ir (subscript sep).

less than $O(\varepsilon^2)$, which also has no effect on the boundary conditions for Eqs. 6.6-6.10. These two facts, combined with the observation that outside of the inner layer, both solutions converge to the hydrodynamic triple-point like $\beta^{-1/2}$, imply that the leading order asymptotic solution is the large β limit of both the quintuple-point and septuple-point solutions.

Bibliography

A. I. Akhiezer, G. J. Lubarski, and R. V. Polovin. The stability of shock waves in magnetohydrodynamics. *Soviet Phys. JETP*, 8:507–511, 1959.

D. Arnett. The role of mixing in astrophysics. *Ap. J. Suppl.*, 127:213–217, 2000.

R. F. Benjamin. Experimental observations of shock stability and shock induced turbulence. In W. P. Dannevik, A. C. Buckingham, and C. E. Leith, editors, *Advances in Compressible Turbulent Mixing*, pages 341–348. Nat. Tech. Inf. Serv., 1992.

A. R. Bestman. Confluence of three shock waves for transverse shocks and shocks in an aligned MHD field. *Journal of Plasma Physics*, 13(1):107–125, 1975.

M. Brouillette. The Richtmyer-Meshkov instability. *Ann. Rev. Fluid Mech.*, 34:445–468, 2002.

M. Brouillette and R Bonazza. Experiments on the Richtmyer-Meshkov instability: wall effects and wave phenomena. *Phys. Fluids*, 11:1127–1142, 1999.

S. Chandrasekhar. *Hydrodynamic and hydromagnetic stability.* Oxford University Press, 1961.

P. Colella. Multidimensional upwind methods for hyperbolic conservation laws. *J. Comp. Phys.*, 87:171–200, 1990a.

Phillip Colella. Multidimensional upwind methods for hyperbolic conservation laws. *J. Comput. Phys.*, 87:171–200, 1990b.

A. W. Cook, W. Cabot, and P. L. Miller. The mixing transition in Rayleigh-Taylor instability. *J. Fluid Mech.*, 511:333–362, 2004.

R. K. Crockett, P. Colella, R. T. Fisher, R. I. Klein, and C. F. McKee. "an unsplit, cell-centered godunov method for ideal mhd". *J. Comp. Phys.*, 203:422–448, 2005.

S. A. E. G. Falle and S. S. Komissarov. On the inadmissibility of non-evolutionary shocks. *J. Plasma Physics*, 65(1):29–58, 2001.

S. A. E. G. Falle, S. S. Komissarov, and P. Joarder. A multidimensional upwind scheme for magnetohydrodynamics. *Mon. Not. R. Astron. Soc.*, 297:265–277, 1998.

G. Fraley. Rayleigh-taylor stability for a normal shock wave-density discontinuity interaction. *Phys. Fluids*, 29, 1986.

R. L. Holmes, J. W. Grove, and D. H. Sharp. Numerical invesitgation of Richtmyer-Meshkov instability using front tracking. *J. Fluid Mech.*, 301:51–64, 1995.

A. Jeffrey and A. Taniuti. *Non-Linear Wave Propagation.* Academic Press, New York, 1964.

C. F. Kennel, R. D. Blandford, and P. Coppi. MHD intermediate shock discontinuities. Part 1. Rankine-Hugoniot conditions. *Journal of Plasma Physics*, 42(2): 299–319, 1989.

A. M. Khokhlov, E. S. Oran, and G. O. Thomas. Numerical simulation of deflagration-to-detonation transition: the role of shock-flame interactions in turbulent flames. *Combust. Flames*, 117:323–339, 1999.

P. H. Krisko and T. W. Hill. Two-dimensional model of a slow-mode expansion-fan at Io. *Geophysical Research Letters*, 18(11):1947–1950, 1991.

M. A. Liberman and A. L. Velikhovich. *Physics of Shock Waves in Gases and Plasmas.* Springer, 1986.

J. D. Lindl, R. L. McCrory, and E. M. Campbell. Progress toward ignition and burn propagation in inertial confinement fusion. *Physics Today*, 45:32–40, 1992.

G. H. Markstein. Flow disturbances induced near a slightly wavy contact surface, or flame front, traversed by a shock wave. *J. Aero. Sci.*, 24:238–239, 1957.

E. E. Meshkov. Instability of the interface of two gases accelerated by a shock wave. *Sov. Fluid Dyn.*, 4:101–108, 1969.

K. Meyer and P. Blewett. Numerical investigation of the stability of a shock-accelerated interface between two fluids. *Phys. Fluids*, 15:753–59, 1972.

K. Mikaelian. Freeze-out and the effect of compressibility in the Richtmyer-Meshkov instability. *Phys. Fluids*, 6:356–68, 1994a.

K. Mikaelian. Oblique shocks and the combined Rayleigh-Taylor, Kelvin-Helmholtz, and Richtmyer-Meshkov instabilities. *Phys. Fluids*, 6:1943–45, 1994b.

R. S. Myong and P. L. Roe. Shock waves and rarefaction waves in magnetohydrodynamics. Part 2. The MHD system. *J. Plasma Phys.*, 58(3):521–552, 1997.

H. Ogawa and T. Fujiwara. Analyses of three shock interactions in magnetohydrodynamics: Aligned-field case. *Physics of Plasmas*, 3(8):2924–2938, 1996.

R. V. Polovin and V. P. Demutskii. *Fundamentals of Magnetohydrodynamics*. Consultants Bureau, New York, 1990.

K. G. Powell, P. L. Roe, T. J. Linde, T. I. Gombosi, and D. L. DeZeeuw. A solution-adaptive upwind scheme for ideal magnetohydrodynamics. *J. Comp. Phys.*, 154: 284–309, 1999a.

K.G. Powell, P.L. Roe, T.J. Linde, T.I. Gombosi, and D.L. DeZeeuw. A Solution-Adaptive Upwind Scheme for Ideal Magnetohydrodynamics. *J. Comp. Phys.*, 154: 284–300, 1999b.

R. D. Richtmyer. Taylor instability in shock acceleration of compressible fluids. *Comm. Pure and Appl. Math.*, 13:297–319, 1960.

Jeff Saltzman. An unsplit 3d upwind method for hyperbolic conservation laws. *J. Comput. Phys.*, 115:153–168, 1994.

R. Samtaney. An upwind method for linearized ideal mhd equations with an evolving base state. Technical report, PPPL, December 2004. In preparation.

R. Samtaney and N. Zabusky. Circulation deposition on on shock-accelerated planar and curved density stratified interface: models and scaling laws. *J. Fluid Mech.*, 269:45–78, 1994.

Ravi Samtaney. Suppression of the Richtmyer-Meshkov instability in the presence of a magnetic field. *Physics of Fluids*, 15(8):L53–L56, 2003.

R. J. Stalker and K. C. A. Crane. Driver gas contamination in a high-enthalpy reflected shock-tunnel. *AIAA J.*, 16:277–279, 1978.

G. W. Sutton and A. Sherman. *Engineering Magnetohydrodynamics*. McGraw-Hill, 1965.

G. I. Taylor. The instability of liquid surfaces when accelerated in a direction perpendicular to their planes. *Proc. R. Soc. A*, 201:192–196, 1950.

M. Torrilhon. Non-uniform convergence of finite volume schemes for Riemann problems of ideal magnetohydrodynamics. *J. Comp. Phys.*, 192:73–94, 2003a.

M. Torrilhon. Uniqueness conditions for Riemann problems of ideal magnetohydrodynamics. *J. Plasma Phys.*, 69(3):253–276, 2003b.

G. Toth. The $\nabla \cdot B = 0$ constraint in shock-capturing magnetohydrodynamics codes. *J. Comp. Phys.*, 161:605–2652, 2000.

A. L. Velikovich. Analytic theory of Richtmyer-Meshkov instability for the case of reflected rarefaction wave. *Phys. Fluids*, 8:1666–79, 1996.

J. G. Wouchuk and K. Nishihara. Asymptotic growth in the linear Richtmyer-Meshkov instability. *Phys. Plasmas*, 4:1028–38, 1997.

C. C. Wu. On MHD intermediate shocks. *Geophys. Res. Lett.*, 14:668–671, 1987.

C. C. Wu. Formation, structure and stability of MHD intermediate shocks. *J. Geophys. Res.*, 95:8149–8175, 1990.

C. C. Wu. Magnetohydrodynamic Riemann problem and the structure of the magnetic reconnection layer. *J. Geophys. Res.*, 100:5579–5598, 1995.

C. C. Wu. Shock wave interaction with the magnetopause. *J. Geophys. Res.*, 105 (A4):7533–7543, 2000.

C. C. Wu. Shock wave interaction with the magnetopause. *Space Sci. Rev.*, 109: 219–226, 2003.

C. C. Wu and P. H. Roberts. Richtmyer-Meshkov instability and the dynamics of the magnetosphere. *Geophys. Res. Letters*, 26(6):655–658, 1999.

C. K. Yang and B. U. Ö. Sonnerup. Compressible magnetic field reconnection: a slow wave model. *Astrophysical Journal*, 206:570–582, 1976.

J. Yang, T. Kubota, and E. E. Zukoski. Applications of shock induced mixing to supersonic combustion. *AIAA J.*, 31:854–862, 1993.

Y Yang, Q. Zhang, and D. Sharp. Small amplitude theory of Richtmyer-Meshkov instability. *Phys. Fluids*, 2:892–95, 1994.

N. Zabusky. Vortex paradigm for accelerated inhomogeneous flows: visiometrics for the Rayleigh-Taylor and Richtmyer-Meshkov environments. *Ann. Rev. Fluid Mech.*, 31:495–536, 1999.